On the analysis of moving heart valves : a numerical fluid-structure interaction model

ON THE ANALYSIS OF MOVING HEART VALVES

A NUMERICAL FLUID-STRUCTURE INTERACTION MODEL

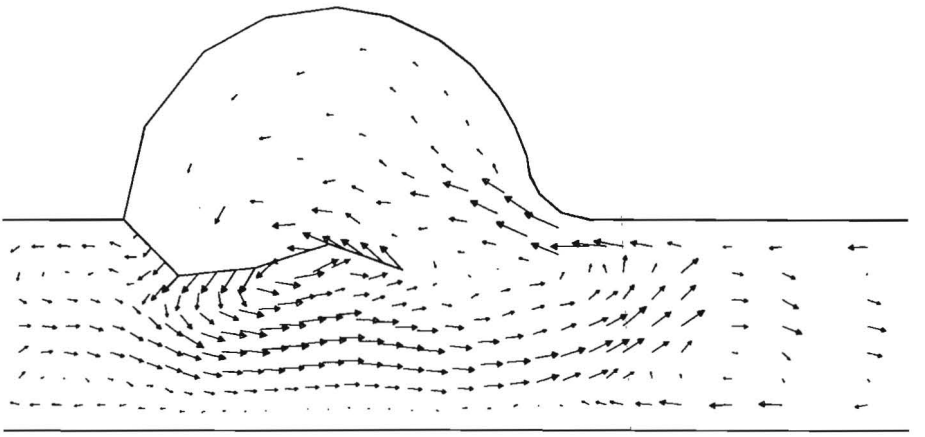

JOOST HORSTEN

ON THE ANALYSIS OF MOVING HEART VALVES

This research is supported by the Dutch Technology Foundation (STW),
grant nr. EWT 58.0857

Financial support by the Netherlands Heart Foundation
for the publication of this thesis is gratefully acknowledged

CIP-GEGEVENS KONINKLIJKE BIBLIOTHEEK DEN HAAG

Horsten, Jan Baptist Adrianus Maria

On the analysis of moving heart valves: a numerical fluid-structure interaction model /
J.B.A.M. Horsten - [S.l. : s.n.]. -Ill.
Proefschrift Eindhoven. - Met lit.opg. - Met een samenvatting in het Nederlands
ISBN 90-9003613-X.
SISO 605.12 UDC 616.12/.14-77
Trefw.: hartkleppen.

ON THE ANALYSIS OF MOVING HEART VALVES

A NUMERICAL FLUID-STRUCTURE INTERACTION MODEL

PROEFSCHRIFT

ter verkrijging van de graad van doctor aan
de Technische Universiteit Eindhoven,
op gezag van de Rector Magnificus, prof.ir. M.Tels,
voor een commissie aangewezen door het College van Dekanen
in het openbaar te verdedigen
op vrijdag 12 oktober 1990 te 16.00 uur

door

Jan Baptist Adrianus Maria Horsten

geboren te Eindhoven

druk: wibro dissertatiedrukkerij, helmond.

Dit proefschrift is goedgekeurd door de promotoren:

prof.dr.ir. D.H. van Campen
prof.dr.ir. G. Vossers

en de copromotor:

dr.ir. A.A. van Steenhoven

Voor Rob

Like all young men I set out to be a genius,
but mercifully laughter intervened

Lawrence Durrell

Contents

	Abstract	vii
	Samenvatting	viii
1.	***Introduction***	
1.1	Motivation	1.1
1.2	Physiological situation	1.1
1.3	Existing models	1.5
1.3.1	Overview	1.5
1.3.2	Peskin's model	1.6
1.3.3	Weakly coupled methods	1.9
1.4	Problem definition	1.11
1.5	Methods applied	1.12
2.	***Physical-mathemical models***	
2.1	Fluid models	2.1
2.1.1	Quasi 1D model	2.2
2.1.2	Von Mises model	2.4
2.1.3	Finite Element model	2.7
2.2	Structure model	2.12
2.3	Fluid-structure interaction models	2.16
2.3.1	Single degree of freedom	2.16
2.3.2	Multiple degrees of freedom	2.19
2.3.3	Summary of algorithm	2.21
2.4	Numerical tests	2.21
2.4.1	Finite element mesh	2.21
2.4.2	Time integration	2.24
2.4.3	Convergence	2.25
2.5	Discussion	2.31
3.	***Experiments***	
3.1	Experimental setup	3.1
3.2	Flow characterization	3.4
3.3	Measurement equipment	3.6
3.4	Test of experimental model	3.7
3.5	Parameter estimation	3.10
3.6	Error estimation	3.12
4.	***Rigid valve***	
4.1	Fixed valve in a steady flow	4.1
4.2	Fixed valve in a pulsatile flow	4.6
4.3	Steady free valve	4.10
4.4	Moving free valve	4.11
4.5	Parameter variation	4.13
4.6	Discussion	4.20

5. Segmented valve

5.1	Free valve in a steady flow	5.1
5.2	Free valve in a pulsatile flow	5.3
5.3	Parameter variation	5.5
5.4	Discussion	5.12

6. Summary and conclusions

References
List of symbols

Appendices
A. Outline of a fully coupled method
B. Von Mises fluid model
C. Finite Element fluid model
D. Van Wijngaarden-Dekker-Brent method
E. Minimization method
F. Quasi 1D fluid model with a parabolic velocity profile

Abstract

In the present study a two-dimensional numerical fluid-structure interaction model is developed for the analysis of the dynamic behavior of a prosthetic heart valve. Two different valve types are considered. The first is a rigid valve which can rotate around its point of attachment. It resembles the case of a disc-type valve prosthesis, which has only one degree of freedom. The second type is a segmented valve, consisting of several rigid segments connected to each other. This type is intended for the design of valve prostheses with more degrees of freedom such as flexible bio-prosthetic or artificial leaflet valves. The buoyancy, the bending stiffness and the load due to the fluid flow are included in the valve equilibrium equation. The constitutive equations may be nonlinear. Large displacements and deformations are allowed.

Various fluid models are incorporated in the fluid-structure interaction model. The simplest are a quasi one-dimensional analytic model and a potential flow model. Furthermore, a finite element fluid model, based on the two-dimensional unsteady Navier-Stokes equations, is applied. The coupled fluid-structure system is solved by a fully coupled, iterative method: both the fluid and the structure subsystem are evaluated separately (one subsystem is solved while the other is kept constant) and an iteration is performed until equilibrium is achieved. The equilibrium position of the rigid valve is found by the application of the root finding method of Brent (1973). The equilibrium position of the segmented valve is found by Powell's hybrid method, a nonlinear least squares method.

Experiments have been performed to validate the fluid-structure interaction models. Steady and unsteady cases have been considered. Separate experiments have been performed to determine the parameters in the constitutive equations. In general the agreement between experimental and numerical results are good. Some small deviations occur, which can be attributed to spurious threedimensional effects in the experimental model or to an insufficient accuracy of the parameters of the constitutive equations. For the rigid valve an unconditional numerical stability is achieved. The numerical segmented valve model converges for a wide range of parameters.

Apart from the application to heart valve prostheses, the models can be used for a rather general class of fluid-structure interaction problems. The model will be useful especially in those cases in which a full description of the fluid is required, when the structure has relatively few degrees of freedom and when the structure displacements and deformations are large.

Samenvatting

Dit onderzoek heeft tot doel het ontwikkelen van een tweedimensionaal numeriek vloeistof-structuur interactiemodel voor de analyse van de beweging van een hartklepprothese in een pulserende bloedstroming. Er worden zowel een stijve klep, roterend om zijn aanhechtingspunt, als een gesegmenteerde klep, bestaande uit een aantal aan elkaar bevestigde stijve segmenten, bestudeerd. De stijve klep is bedoeld voor de analyse van mechanische disk-prothesen, de gesegmenteerde klep voor de analyse van flexibele prothesen van biologische of kunstmatige materialen. De opwaartse krachten, de buigstijfheid in de bevestigingspunten en de invloed van de vloeistofstroming worden betrokken in de evenwichtsvergelijking van de klep. De constitutieve vergelijkingen kunnen niet-lineair zijn. Grote verplaatsingen en vervormingen zijn mogelijk.

De vloeistofstroming wordt beschreven door zowel een quasi-eendimensionaal analytisch model, een tweedimensionaal model potentiaalstromingsmodel als door een tweedimensionaal numeriek eindige elementen model, gebaseerd op de instationaire Navier-Stokes vergelijking. De oplossing van het gekoppelde vloeistof-structuur systeem wordt gevonden met een volledig gekoppelde, iteratieve methode: het vloeistof- en het structuursubsysteem worden apart opgelost en de evenwichtssituatie wordt iteratief bepaald. De evenwichtspositie van de stijve klep wordt bepaald met de methode van Brent (1973) voor het vinden van de oplossing van een algebraïsche niet-lineaire vergelijking. De evenwichtsstand van de gesegmenteerde klep wordt gevonden met Powell's hybride methode, een niet-lineaire kleinste kwadraten methode.

De theoretische modellen zijn geverifieerd aan de hand van experimenten in zowel stationaire als instationaire situaties. Over het algemeen komen de theoretische en experimentele resultaten goed overeen. Er treden enkele kleine afwijkingen op die toegeschreven kunnen worden aan ongewenste driedimensionale stromingseffecten in het experimentele model en aan de beprekte nauwkeurigheid van de materiaalparameters in de constitutieve vergelijkingen. In het geval van de stijve klep is onvoorwaardelijke numerieke stabiliteit bereikt. Het numerieke model voor de gesegmenteerde klep convergeert voor een groot bereik van parameters.

Naast de toepassing op hartklepprothesen kunnen de modellen ook worden toegepast op een meer algemene klasse van vloeistof-structuur interactieproblemen. De modellen zijn vooral geschikt wanneer een volledige beschrijving van de vloestofstroming vereist is, wanneer de structuur relatief weinig vrijheidsgraden heeft en wanneer de structuur grote verplaatsingen en vervormingen ondergaat.

1. INTRODUCTION

1.1 Motivation

Frequently, natural human aortic valves do not function properly and need to be replaced by valve prostheses. Commercially available valve prostheses can be divided into two main categories: mechanical and biological prostheses. Nowadays, most mechanical valve prostheses are disc–type valve prostheses, which consist of one or two rigid plates, mounted in a frame. Biological valve prostheses are constructed from prepared porcine valves or from porcine or bovine heart tissue. A survey of the merits of these prostheses types is given by Rousseau (1985).

This study is carried out within the framework of a research project which has as ultimate goal the design of an improved aortic valve prosthesis, based upon a fundamental understanding of the behavior of the natural valve. This prosthesis should be a tri-leaflet valve, which enables the use of the three natural sinuses. The geometry of the valve should be such that it provides gradual valve closure. The leaflets should be constructed of flexible fiber reinforced synthetic materials to overcome complications associated with biological leaflet valves. Previous research is done by van Steenhoven (1979), who investigated the fluid dynamics of the natural valve, by Sauren (1981), who investigated the mechanics of the natural valve, by van Renterghem (1983), who investigated the valve geometry during the cardiac cycle and by Rousseau (1985) who developed a numerical model for the mechanical analysis of an artificial leaflet valve in the fully closed situation.

This study will focus on the numerical analysis of the dynamic behavior of a model valve prosthesis. The object is the development of a numerical fluid–structure interaction model, which describes the opening and closure of the valve. Such a model is necessary for the optimization of the dynamical aspects of the valve: improvement of the closure efficiency and minimization of flow resistance, fluid shear stresses and bending strains. The latter constitute a stimulating factor in the forming of calcium deposits (Rousseau,1985).

1.2 Physiological situation

Sketches of the heart and the natural aortic valve are given in figures 1.1, 1.2 and 1.3. The aortic valve is located between the left ventricle and the aorta. It consists of three flexible leaflets. The valve exhibits a 120° rotational symmetry. Behind every leaflet a cavity in the aorta is present, called the sinus of Valsalva (Reid, 1970,

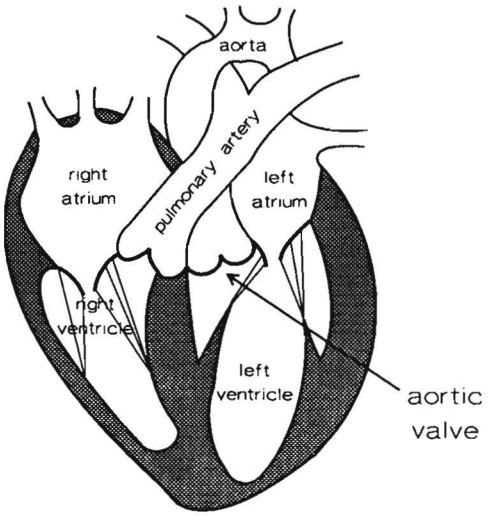

figure 1.1 Sketch of the human heart (after Arts, 1978)

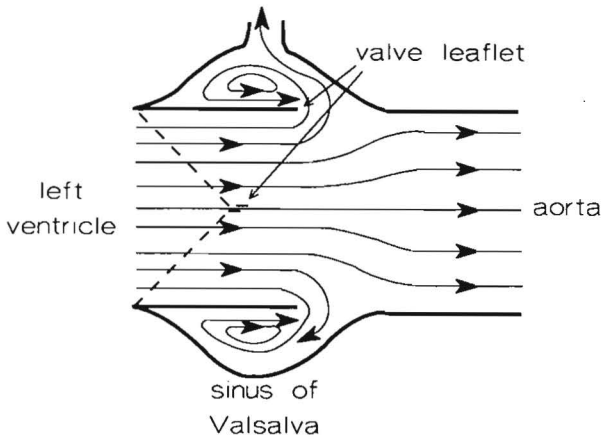

figure 1.2 Sketch of the natural aortic valve in a fully opened position (solid line) and in a closed position (dashed line) and the flow phenomena around an opened valve (after Bellhouse in Bergel, 1972)

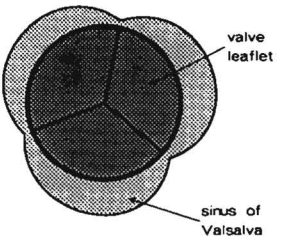

figure 1.3 **Sketch of the natural aortic valve as seen from the aorta into the direction of the left ventricle**

Swanson & Clark, 1973). The valve leaflets are made of soft elastine texture, reinforced by collagen fibers (Sauren, 1981). This construction enables the valve to be flexible while opening or closing, to minimize the flow resistance, and to be strong in fully closed position when it has to withstand the largest pressure drop. The valve tissue is anisotropic and visco–elastic (Sauren, 1981). The visco–elasticity is mainly important in the fully closed situation, when the stresses reach their maximum values and some relaxation occurs. When the valve is open, the stresses are very small (Thubrikar,1982). So, in this situation the mechanical behavior of the texture is of minor importance. The density of the valve texture is about equal to that of blood, so buoyancy forces are negligible in the in–vivo situation. Since the mass of the valve itself is much smaller than the mass of the blood flowing around it, it can be expected that also inertial effects of the valve are negligible. The aperture of the valve varies from fully closed to fully opened (van Steenhoven, 1979) so the displacement of the valve leaflets is large.

The fluid phenomena around the valve are rather complex. Figure 1.4 shows that the variations of the flow rate are large. Furthermore, the shape of the fluid domain changes considerably due to the large valve displacements. During the systolic phase of each heart period vortices are formed behind each leaflet in the sini (see figure 1.2) and they are broken down again during the diastolic phase. Since the valve is located at the entrance of the aorta, no flow development can occur and the axial velocity is approximately constant over the diameter. In large blood vessels as the aorta, blood behaves in a good approximation like an incompressible, Newtonian fluid (Caro et al., 1978). It appears that in the case of properly working heart valves, the fluid flow is laminar and that no turbulence occurs (Nerem & Seed, 1972). Only when a heart valve or valve prosthesis exhibits a malfunctioning, some turbulence can occur.

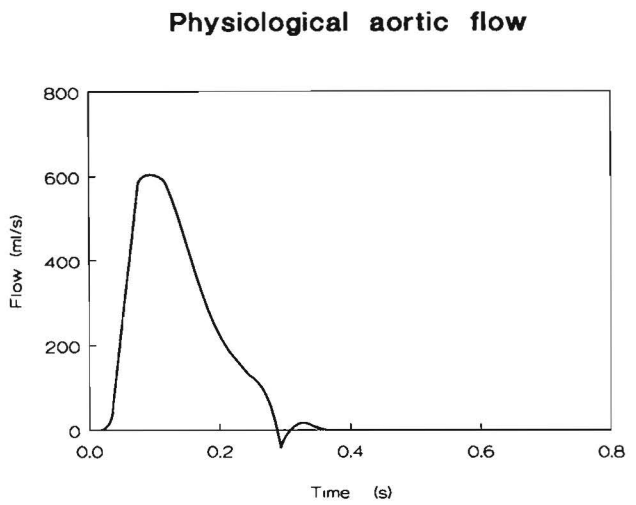

figure 1.4 Physiological flow rate as a function of time (after Milnor, 1982)

Laminar flow of a Newtonian incompressible fluid satisfies the Navier-Stokes and continuity equations (Batchelor, 1983). In dimensionless form these equations read:

$$St\,\dot{\vec{u}} + \vec{u}\cdot\nabla\,\vec{u} - \frac{1}{Re}\nabla^2\vec{u} + \nabla\,p = \vec{0} \qquad (1.1)$$

$$\nabla\cdot\vec{u} = 0 \qquad (1.2)$$

with $\vec{u}$ the velocity vector, p the pressure, ∇ the gradient vector operator and the superscript dot $\dot{}$ denotes the local time derivative. Re is the Reynolds number, defined as $Re = u_c h_c/\nu$ with u_c the cross-section averaged velocity at top systole, h_c a characteristic length and ν the kinematic viscosity. Physiological values are given by Milnor (1982). The maximum Reynolds number, based upon aorta radius as characteristic length, is about 4500. St denotes the Strouhal number and is defined as $St = h_c/u_c\tau$ with τ the deceleration time of the systole. A typical physiological value of St is 0.1.

An important feature of the valve-fluid system is that the motion of the valve and the fluid flow are strongly coupled. The valve imposes the shape of the fluid domain and the boundary conditions on the contact surface. On the other hand, the valve itself is passive and the only mechanisms which move it are the fluid stresses

on the valve. The interaction phenomena are responsible for an important feature of the natural valve. It already closes partially during flow deceleration and only a very small amount of back flow is necessary to obtain a full closure, thus increasing the efficiency of the valve (Bellhouse & Talbot, 1969). This process is initiated by the adverse pressure gradient during flow deceleration (van Steenhoven & van Dongen, 1979). Another physiological relevant aspect of this early closure is the reduction of the pressure rise just after valve closure (van Steenhoven & van Dongen, 1986).

1.3 Existing models

Several models have been developed which might be relevant for the description of the flow around heart valves. In section 1.3.1, a short overview is given of some models which have some relation to this study, but which have been developed for different situations. In sections 1.3.2 and 1.3.3, two types of models are described which are more related to this study. In section 1.3.4 an outline of an alternative strategy is given.

In these models several types of coupling methods are used. In order to avoid confusion, some terms are defined here. *Decoupled* methods ignore the interaction almost completely. First, the behavior of one of the subsystems (fluid or structure) is computed for every point of time. The solution of this first subsystem is used as boundary condition for the computation of the second one. The interaction is only one way, from the first to the second subsystem. In *weakly coupled* methods both subsystems are also solved separately in time, but only during one discrete timestep. Before the start of a new timestep, the solution of the previous timestep of one subsystem is available to solve the other subsystem. In both strategies, the subsystems need not to be exactly in equilibrium with each other at every timestep. The guarantee of this equilibrium is the start for *fully coupled* methods. In *iteratively fully coupled* methods, both subsystems are still solved separately but the equilibrium is obtained by some sort of iteration. In *directly fully coupled* methods both subsystems are solved simultaneously.

1.3.1 Overview

There are several numerical models which give an analysis of the flow field around fixed heart valves. Examples of these studies are those of Idelsohn et al. (1985), Stevenson et al. (1985) and Thalassoudis et al. (1984). They give a rather accurate description of the two–dimensional steady flow around a fully opened valve. The

authors are mainly interested in the calculation of shear stresses in the fluid. The motion of the valve is not taken into account, thus ignoring the interaction between fluid flow and valve motion.

A large category of models which have some relation to the present problem are those analyzing the flow around flexible membranes and plates and along compliant walls. Examples are the studies of Frederiks et al. (1986) and Gad–el–Hak (1986). Their main interest is the occurrence of flow–induced instabilities in the structure. In most studies, the problem is simplified by ignoring viscous phenomena and by restricting to small structure amplitudes, so that linear models can be applied. Since in our case these restrictions are too severe and since flow instabilities are not yet of primary concern, these type of models are not applicable here.

A third category is that of analytical quasi one–dimensional models, specially developed for the interaction problem of heart valve and blood flow. Examples of these models are those of Bellhouse & Talbot (1969), van Steenhoven & van Dongen (1979), Lee & Talbot (1979) and Wipperman (1985). In these models the cross–section averaged values of axial fluid velocity and pressure are used and special assumptions for the fluid flow and pressure in the sinus are made. Notwithstanding these strong simplifications they give a fair global description of the valve motion. However, they are not accurate enough for a detailed analysis of the effect of small variations of the valve geometry and the mechanical properties on the valve motion.

1.3.2 Peskin's model

A model, specially developed for the mitral heart valve, is given by Peskin (1977). It incorporates the full Navier–Stokes equations and flexible boundaries. An essential characteristic of the model is that the computation of fluid flow and structure motion are partly decoupled: a weak coupling is applied. Another feature is that the interaction between fluid and structure is not taken into account by prescribing boundary conditions at the contact surface but by using local body forces in the fluid at the location of the contact surface. The structure is fully submerged in the fluid. Magnitude and direction of these local body forces are chosen in such a way that they simulate the presence of the submerged structure.

The starting point of the model is formed by the Navier–Stokes and continuity equations. The Navier-Stokes equation is extended with a body force $\vec{f}$ according to:

$$St\,\dot{\vec{u}} + \vec{u}\cdot\nabla\vec{u} - \frac{1}{Re}\nabla^2\vec{u} + \nabla p - \vec{f} = \vec{0} \qquad (1.3)$$

with $\vec{f}$ the external body force per unit mass resulting from the presence of the structure. Boundary conditions are only necessary at the border of the computation domain.

When $\vec{f}$ is known on a time level t on every place $\vec{x}$, then the fluid velocity can be computed from equations (1.3) and (1.2). That still leaves the problem of the computation of $\vec{f}$. At this stage, Peskin makes the assumption that the inertia of the structure is negligible compared to that of the surrounding blood and that the structure is purely elastic. From these assumptions follows that the force $\vec{f}$, acting on the fluid by the structure, is fully determined by the instantaneous geometry of the structure and that it always balances the local internal elastic forces in the structure.

Because the fluid is viscous, no discontinuities in the velocity can occur. Therefore, the local fluid velocity is equal on both sides of the structure and equal to the velocity of the structure. Because tangential velocity of both fluid and structure are equal, no slip on the structure surface occurs. Since the normal velocities are equal, no fluid will flow through the structure. Therefore, the physical boundary conditions on the structure are satisfied automatically.

The structure is modeled as a network of linear elastic springs, which connect the discrete structure points. Also bending stiffness is incorporated. For a given geometry of the boundary the internal structure forces can be computed.

For the numerical computation of the fluid velocity field, Peskin uses a finite difference method. A square grid with equidistant grid points is used. He uses a hybrid grid approach: the discrete structure points are allowed to move freely through this grid. They do not have to coincide with the fluid grid points. Consequently, an interpolation must be performed between fluid and structure points. Peskin's interpolation approach is based on the application of discrete delta functions.

Hence, the equations of motion of structure and fluid are weakly coupled. The interaction is incorporated by the structure force $\vec{f}$. Therefore, in the discrete time integration the structure and fluid systems will be solved separately. The most simple approach would be just to compute the structure force at the start of the timestep and to proceed with the computation of the fluid flow. According to Peskin such a method appears to be numerically unstable. Therefore he uses a somewhat more sophisticated approach: he tries to give an approximation of the force at the end of the timestep.

In order to estimate the structure force, he states that it can be approximated by

$$\vec{f} = St \frac{\partial \vec{u}}{\partial t} \qquad (1.4)$$

This is in fact a simplification of the Navier–Stokes equation (1.3) in which the convective, viscous and pressure forces are neglected. Using this approximation, estimates of valve position of the valve leaflet and the corresponding structure force at the end of the actual time step are computed. In turn, these estimates are used to compute an approximation of the fluid velocity field at the end of the timestep. Peskin assumes that this approximation is good enough to ensure that, at the end of the timestep, the estimated fluid–structure force and the internal structure force balance, and that both structure and fluid are in equilibrium. No iteration is performed to guarantee such an equilibrium. In general, these forces will not balance.

The way in which the fluid–structure force is computed, is crucial. Peskin's approach is based on the simplified Navier–Stokes equation (1.4). He does not give any justification for this choice. In fact, (1.4) will only be a good approximation of (1.3) if the local acceleration term is much larger than the other terms. A simple example, of a case in which this condition is obviously not satisfied, is the steady flow parallel to the structure, for instance a fully opened valve. In that case, the internal structure forces will be in equilibrium with the *viscous* forces. In steady cases where large velocity gradients occur, the *convective* term will dominate, for example near an almost closed valve.

Using the dimensionless parameters Re and St an estimate can be made of the relative importance of the different terms in (1.3). In the aorta Re=4500 and St=0.1. For the mitral valve these values are about Re=3500 and St=0.2. The product of St and Re reflects the magnitude of the local acceleration term in the Navier-Stokes equation relative to that of the viscous term. So it can be concluded that the negligence of the *viscous* forces, compared to the *local acceleration* forces is reasonable as long as no flow separation occurs. But if the flow separates, viscosity must be incorporated, at least at the separation point. Furthermore, the *convective* forces are of the same order or even larger than the local acceleration forces (since St<1). The negligence of these forces is therefore even more questionable. This conclusion is confirmed by the work of van Steenhoven and van Dongen (1979), who found that in the physiological range of Reynolds numbers viscous phenomena are of minor importance and that the influence of the St–number is large. If St > 0.3 the acceleration forces dominate the convective ones. If St<0.15 this is not true anymore. This means that Peskin's approach would not be valid for the aortic valve. The application to the mitral valve (as Peskin does) can be slightly better justified.

The highly simplified estimation of the interaction forces results in a numerical

stability which is only conditional. In more recent work (Tu & Peskin, 1988) a model is presented in which unconditional stability is achieved. However, this model is only applied to Stokes flow. Another drawback of Peskin's method is the spatial accuracy which is limited to first order, due to the repeated interpolation of velocity and forces to and from fluid grid points and structure points. Because of these limitations, Peskin's method is not applied in this study.

1.3.3 Weakly coupled methods

Another category of numerical models is the one developed for the interaction of fluid with large, complex structures. Overviews of this type of models are given by Belytschko (1980) and Park & Felippa (1983). A typical application of these type of models is the response analysis of a nuclear reactor due to some accident. An example is found in the work of Kulak (1981, 1984, 1985). Most models are finite element models. The emphasis lays on the description of the structure. Inertia, damping and stiffness are incorporated. Structure displacements can be large, so nonlinear structure models are applied. Many of them use an arbitrary Lagrange–Euler description for the spatial discretization. In general, the fluid description is more simplified, by restricting it to linear models with an inviscid fluid and with small fluid displacements. Typical for those models is a partial decoupling (or *weak coupling*) of fluid and structure. The total system is partitioned in a *fluid* and a *structure* subsystem, which are integrated separately in time. Several variations are developed. The simplest one is the *explicit-explicit* partition. Both subsystems are integrated with an explicit time integration system. There are no special requirements for the boundary conditions at the contact surface, since they can simply be extrapolated from previous timesteps. These models can be very efficient, but they are only conditionally stable. Another possibility is an *explicit-implicit* partition: first one system (usually the fluid) is integrated with an explicit method. The solution of this subsystem at the boundary is used as a contact condition for the second subsystem, which is integrated with an implicit scheme. In general, these methods show better stability properties, but they are still conditionally stable. In an *implicit-implicit* method both subsystems are integrated implicitly, thus improving the stability further. In this case a complication arises for the contact condition. None of the subsystems can be integrated first when the contact conditions are not available (which depend on the solution of the other subsystem). This contact condition must be extrapolated from the previous timestep, thus introducing an explicit component in the algorithm, which may destroy the stability of the total system. Much attention is

paid to stability analyses in order to select the proper extrapolator. An outline of such a weakly coupled method is given in appendix B.

These types of methods can not generally be applied to the combination of an incompressible fluid and a structure which has small inertia, damping and bending stiffness, like a prosthetic leaflet heart valve. Consider for example the valvular opening and closing phase when the valve is at least partly strain free. Then, in some parts no internal stresses are present and consequently, the fluid forces on both sides of the valve must balance. If a weakly coupled method is applied, first the position and/or the velocity of the boundary is estimated. If first the fluid flow is computed, generally the fluid stresses on both sides of the valve will *not* balance. The resulting fluid load is applied to the valve and the valve displacements are computed. Due to the small stiffness of the structure these displacements will be large, and may even be infinite, in order to obtain internal stresses which balance the fluid load. Apart from numerical problems, which may arise because the initial estimate of the valve may be an undetermined situation, it will be clear that this situation is not physically realistic. In reality, the deformation will be finite since the balancing mechanism is not the increase of the internal stresses, but an instantaneous fluid pressure rise behind the valve, retarding the valve. This correction mechanism is lacking in the weakly coupled approach and the method is therefore expected not to be reliable for all situations which can be expected when examining a leaflet valve.

If, on the other hand, the structure would have no inertia and would be stress-free during the full cardiac cycle, an alternative, decoupled strategy would be applicable. If the valve has no internal stresses, it can not exert any force on the fluid and the valve motion would not affect the fluid flow. Then, it would be possible to compute the fluid flow while ignoring the presence of the valve and to compute the valve deformation afterwards, assuming that it flushes along with the fluid. A continuously stress-free valve would be of no use, since it does not exert any force on the fluid and therefore it can not prevent the fluid from flowing back into the ventricle. So, a decoupled approach will not be applicable. The problem at hand is characterized by a combination of situations with and without stress. Since both decoupled and weakly coupled methods are not readily applicable, a fully coupled approach must be used.

1.3.4 Outline of fully coupled methods

One could think of a directly fully coupled treatment of fluid and structure. No example of such a strategy is found in the literature. An outline of a possible approach is given in appendix A. A complication is the combination of the Langrangian description for the structure (nodal points coincide with material points and move together with the structure) and the Eulerian description for the fluid (nodal points are fixed in space). An arbitrary Langrange–Euler approach for the fluid must be used in which the nodal points can move with an arbitrary speed. In fact, these methods are developed for weakly coupled strategies, as are described in section 1.3.3. In those cases the method can be very much simplified since the structure displacement is computed first, uncoupled from the fluid flow. At the moment that the fluid flow must be computed, the position and velocity of the boundaries are all known, and the fluid computation is fairly straightforward. The implementation of a truly fully coupled method is much more complicated, since fluid boundary position and speed are a function of the fluid flow itself and are therefore unknown. This observation gives rise to extra nonlinear terms in the system of equations. At this moment, it is not clear how they can affect the stability of the system.

Another drawback of a directly fully coupled approach is that the number of equations which must be solved simultaneously, increases. Furthermore, one is forced to implement both structure and fluid solver in one software package. This may result in large, inflexible computer codes, which are difficult to adapt or maintain. Because of these considerations, the directly fully coupled approach is not applied in this study. An *iteratively* fully coupled method does not suffer from the disadvantages of a directly coupled method. Both subsystems are evaluated separately: one subsystem is solved while the other is kept constant. Therefore, an Eulerian description can be used for the fluid. If required, both subsystems can be solved with a different software package. In general, the memory computer requirements will be less than in the fully coupled approach, since the subsystems are smaller than a directly coupled system. A possible drawback could be the number of iterations needed to obtain the solution.

1.4 Problem definition

The general object of this study is the development of a numerical fluid–structure interaction model, allowing a full description of the flow field in complex shaped domains and for structures which may have a variety of mechanical and dynamical

properties. The structure displacements may be large. The interaction between fluid and structure is fully taken into account. An iteratively fully coupled approach will be applied.

Because of computational reasons, the fluid flow and the structure are restricted to be two–dimensional. The model valve is shown in figure 1.5. It may be rigid or segmented, consisting of several rigid links. Behind the valve a cylindrical cavity is present, which is a modeled version of the physiological sinus of Valsalva. The rigid valve and the links can rotate around their points of attachment. No strains occur, so their lengths are fixed. The links are attached to the rigid channel or to each other by membranous hinges. These hinges may cause a bending moment. Since in general the density of the valve may be different from the density of the fluid a gravity or buoyancy force may act on the links. The inertia of the valve is neglected. The rigid valve can be regarded as a disc–type prosthesis. With an increasing number of links, the segmented valve will behave more and more like a fully flexible valve. The fluid flow will be assumed to be incompressible, Newtonian and laminar.

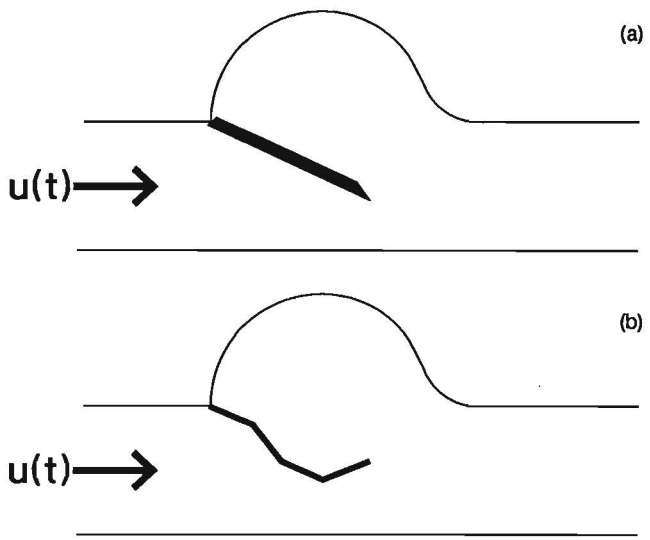

Figure 1.5 Two-dimensional heart valve models (a) rigid, (b) segmented

1.5 Methods applied

Several fluid models will be used, the most advanced is based on the full two–dimensional Navier–Stokes and continuity equations for a Newtonian, incompressible and laminar fluid by a finite element method. Furthermore, two simpler, analytical fluid models will be applied in order to gain more fundamental physical understanding of the fluid flow phenomena and to demonstrate the flexibility of the interaction model. The valve is described by the equilibrium equation of a set of rigid links.

The interaction between fluid and structure is taken fully into account. The equations of motion of fluid and structure are iteratively coupled. The subsystems are evaluated separately and an iteration is applied until equilibrium between fluid and valve is achieved. In this way the numerical stability is guaranteed. It will appear that the assumptions, made for fluid and structure, are not restrictive to the actual interaction model. For example, inertial and (visco–) elastic phenomena of the structure can easily be incorporated and, as will be illustrated, the interaction model can easily be used in combination with any fluid solver, which matches the needs of a specific problem.

The theoretical models will be validated by means of a comparison of theoretical simulations to experimental results.

2. PHYSICAL-MATHEMATICAL MODELS

In this chapter, a model is presented for the analysis of a coupled system of fluid flow and structure motion. As discussed in chapter 1, the approach is an iteratively fully coupled one. Several variations are developed, using different models for the fluid flow (numerical or analytical) and the valve (rigid or segmented).

Unless otherwise stated, dimensionless quantities are used. The characteristic length is defined as the channel height and the characteristic velocity as the velocity, averaged over the channel height at the moment of maximum flow rate. The characteristic time is defined as the deceleration time if the flow rate is pulsatile, as the period time if the flow rate is varying harmonically and as the ratio of characteristic length and characteristic velocity if the flow rate is constant.

2.1 Fluid models

Figure 2.1 shows a global sketch of the flow field around the rigid model valve in a steady flow case. It is obtained by visualizations by ink injection in the experimental model, which will be described in chapter 3. The fluid phenomena are similar to physiological ones: flow separation at the valve tip and the formation of a vortex behind the valve. Since both the fluid phenomena and the shape of the domain are rather complex, a suitable approach for the flow description in this study is a finite element method. In section 2.1.3 such a method is described which solves the full Navier-Stokes equations.

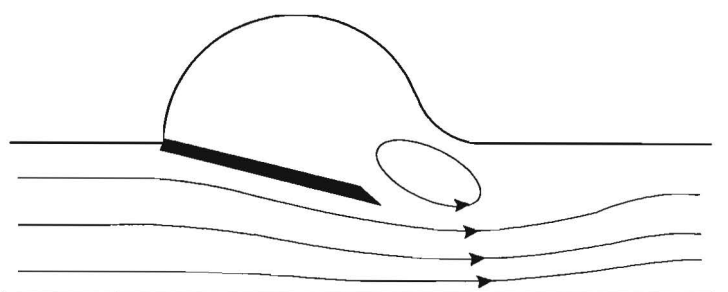

figure 2.1 Global sketch of the steady flow field around a rigid model valve

This numerical model is preceded by two simpler, analytical models. They are introduced because it will turn out that, notwithstanding their simplicity, they are able to describe some aspects of the flow field quite well, albeit in a qualitative way, thus giving more insight in the physics of the flow. Furthermore, they illustrate the flexibility of the fluid-structure interaction model. Both analytical models are applied to a valve in a steady position. A simple quasi one-dimensional model, based on Bernoulli's theorem and conservation of mass, is given in section 2.1.1. Section 2.1.2 describes a two-dimensional potential flow model.

2.1.1 Quasi one-dimensional fluid model

In this section a simplified analytical model is presented for the fluid flow around a two-dimensional aortic valve. The model is presented for the case of a rigid valve in an unsteady flow. Besides, a formulation is given for segmented valve in a steady flow.

In the derivation of the models it is assumed that the fluid is incompressible, that the viscosity of the fluid is negligible and that the velocity gradient in the vertical direction is zero ("plug flow"). In order to simulate the effect of flow separation at the valve tip, the pressure in the sinus is assumed to be constant and equal to the pressure at the downstream end of the valve. The physiological Reynolds number is fairly high (Re_{max}=4500), so viscous effects in the fluid are small indeed. This does not hold for the valve tip, where the flow separates. Since the fluid velocity in the sinus is much smaller than in the main flow and the pressure must be continuous in the vertical direction, the flow separation is accounted for in a simplified way by the assumption with respect to the sinus pressure. These assumptions are the same as made by van Steenhoven & van Dongen (1979) and by Wipperman (1985) who also incorporated the unsteady valve motion in their models.

Because of these assumptions, the continuity equation reduces to:

$$h(x)u(x,t) = h_0u_0(t) = h_tu_t(t) \tag{2.1}$$

with $h_0 \equiv 1$. The momentum equation reduces to Bernoulli's theorem:

$$\tfrac{1}{2}u^2(x) + p(x) = \tfrac{1}{2}u_t^2 + p_t + \frac{\partial}{\partial t}\int_x^{x_t} u(x)dx \tag{2.2}$$

x denotes the horizontal coordinate, h the local valve height, u and p the axial fluid

velocity and pressure, respectively and t the time. Subscripts o and t refer to the valve fixation point and the tip respectively. Without loss of generality, it can be stated that

$$p_t = 0 \tag{2.3}$$

Furthermore,

$$x_0 = 0 \tag{2.4a}$$
$$h(0) = h_0 \tag{2.4b}$$
$$x_i = x_{i-1} + l_i \cos \varphi_i \tag{2.4c}$$
$$h_i = h_{i-1} - l_i \sin \varphi_i \tag{2.4d}$$
$$h = h_{i-1} - s \sin \varphi_i \tag{2.4e}$$

where x_i and h_i are the horizontal vertical coordinate of the connection point between the links i and i+1, whereas φ_i is the angle between link i and the horizontal axis (cf. figure 2.5). l_i is the length of link i and s the local coordinate along a link.

Rigid valve in a pulsatile flow

Substitution of (2.1), (2.3) and (2.4) in (2.2) gives (with n=1, $l=l_1$ and $\varphi=\varphi_1$) an expression for the pressure along the valve:

$$p(s) = \tfrac{1}{2}h_0^2 u_0^2 \left[\frac{1}{(h_0 - l \sin\varphi)^2} - \frac{1}{(h_0 - s \sin\varphi)^2}\right] + h_0 \frac{du_0}{dt} \int_0^l \frac{ds}{(h_0 - s \sin\varphi)^2}$$

$$= \tfrac{1}{2}h_0^2 u_0^2 \left[\frac{1}{(h_0 - l \sin\varphi)^2} - \frac{1}{(h_0 - s \sin\varphi)^2}\right] + \frac{h_0}{\sin\varphi} \frac{du_0}{dt} \left[\ln(h_0 - s \sin\varphi) - \ln(h_0 - l \sin\varphi)\right] \tag{2.5}$$

The moment acting on the valve is obtained by integrating the pressure along the valve according to

$$m_f = \int_0^l p(s)\, s\, ds \tag{2.6}$$

Substituting (2.5) in (2.6) and using some standard integrals yields

$$m_f = \tfrac{1}{2}h_0^2u_0^2\left[\frac{l^2}{2(h_0 - l\sin\varphi)^2} - \frac{1}{\sin^2\varphi}\left\{\ln\left(\frac{h_0 - l\sin\varphi}{h_0}\right) + \frac{h_0}{h_0 - l\sin\varphi} - 1\right\}\right] +$$

$$\frac{h_0}{\sin\varphi}\frac{du_0}{dt}\left[\left(\frac{h_0}{\sin\varphi}\right)^2\ln\left(\frac{h}{h_0 - l\sin\varphi}\right) - \frac{h_0 l}{2\sin\varphi} - \left(\frac{l}{4}\right)^2\right] \qquad (2.7)$$

Segmented valve in a steady flow

The pressure, integrated force and moment on a link of the chain valve can be calculated in a very similar way as in the rigid valve case (if the flow is steady). The analog of equation (2.5) for a separate link i is

$$p(s) = \tfrac{1}{2}h_0^2u_0^2\left[\frac{1}{h_t^2} - \frac{1}{(h_{i-1} - s\sin\varphi_i)^2}\right] \qquad (2.8)$$

The fluid link force is given by

$$f_i = \int_0^{l_i} p\,ds = \qquad (2.9)$$

$$\tfrac{1}{2}h_0^2u_0^2\left[\frac{l_i}{h_t^2} - \frac{1}{\sin\varphi_i\,(h_{i-1} - l_i\sin\varphi_i)} + \frac{1}{h_{i-1}\sin\varphi_i}\right] \qquad (2.10)$$

Here f_i is directed normal to the link. The link moment due to the fluid is found in an analogous way as (2.7):

$$m_{fi} = \tfrac{1}{2}h_0^2u_0^2\left[\frac{1}{2}\left(\frac{l_i}{h_t^2}\right)^2 -\right.$$

$$\left.\frac{1}{\sin^2\varphi_i}\left\{\ln\left(\frac{h_{i-1} - l_i\sin\varphi_i}{h_{i-1}}\right) + \frac{h_{i-1}}{h_{i-1} - l_i\sin\varphi_i} - 1\right\}\right] \qquad (2.11)$$

2.1.2 Von Mises fluid model

An appropriate analytical model for the steady flow around the rigid valve is given by von Mises (Gurevich, 1965). The model is a potential flow model and uses complex function theory. For practical application the resulting analytical expression need to be evaluated numerically. An outline of the original fluid model is given in appendix

C. Here, the essentials and the application to our problem are given.

The domain of the model is shown in figure 2.2. There is a close resemblance to the aortic model. The sinus is not explicitly present, but a wake is assumed to be present behind the valve, bounded by a free streamline. At the valve tip, the streamline is not in the axial direction (as in the case of the quasi one-dimensional model in section 2.1.1) but tangential to the valve.

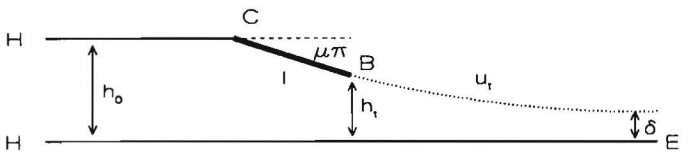

figure 2.2 Fluid domain according to the von Mises fluid model

The domain in figure 2.2 is regarded as a complex plane. In this plane a complex velocity and a corresponding velocity potential are defined. These quantities can be evaluated by transforming the plane to another complex plane, in which the fluid domain has the shape of an upper half circle. In turn, this half circle can be expanded to the full transformed plane. More details of this transformation are given in appendix C. With the use of some complex function theory, the velocity near the valve can be expressed as

$$u(s) = u_0(\frac{\sigma}{\eta})^{\mu} \tag{2.12}$$

in which u_0 is the entrance velocity, $\mu\pi$ the angle of the valve with the horizontal axis, s the coordinate along the valve from fixation point to tip and σ a parameter depending on s according to

$$\frac{s}{h_0} = 1 - \frac{\eta^{\mu}}{\pi}\int_{\sigma}^{1}\left[\frac{1}{\sigma'+\eta} + \frac{1}{\sigma'+1/\eta} - \frac{2}{\sigma'+1}\right]\frac{d\sigma'}{\sigma'^{\mu}} \tag{2.13}$$

η is representing the position of the source of the entrance flow in the transformed complex plane and is determined by

$$\frac{\eta^{\mu}}{\pi}\int_{0}^{1}\left[\frac{1}{\sigma+\eta} + \frac{1}{\sigma+1/\eta} - \frac{2}{\sigma+1}\right]\frac{d\sigma}{\sigma^{\mu}} = \frac{l}{h_0}, \tag{2.14}$$

The pressure p along the valve can be expressed by using Bernoulli's theorem as

$$p(s) = \tfrac{1}{2} u_t^2 - \tfrac{1}{2} u^2(s) \qquad (2.15a)$$

$$= \tfrac{1}{2} u_0^2 \eta^{-2\mu} (1 - (\sigma)^{2\mu}) \qquad (2.15b)$$

with u_t the velocity at the valve tip and at the free streamline. The moment which is exerted by the fluid on the valve is given by

$$m_f = \int_0^l p(s)\, s\, ds \qquad (2.16)$$

The fluid problem is fully defined by (2.12) up to (2.15). First η must be solved from (2.14). η depends only on the given domain parameters μ,l and h_0. Since the equation is a nonlinear integral equation, it is solved numerically. For that purpose (2.14) is redefined as

$$f(\eta) = \frac{l}{h_0} - \frac{\eta^{\mu}}{\pi} \int_0^1 \left[\frac{1}{\sigma+\eta} + \frac{1}{\sigma+1/\eta} - \frac{2}{\sigma+1} \right] \frac{d\sigma}{\sigma^{\mu}} = 0 \qquad (2.17)$$

which is iteratively solved with the Van Wijngaarden-Dekker-Brent method (see appendix E). The integral in (2.17) is evaluated with a combination of the midpoint rule and a Romberg extrapolation scheme (Press,1985). The midpoint rule was used instead of the more efficient combination of trapezoidal rule and Romberg extrapolation because of the integrable $1/\sigma^{\mu}$ singularity at σ=0. Because of this singularity also a change of variables is carried out according to

$$\int_0^1 g(\sigma)d\sigma = \frac{1}{1-\mu} \int_0^1 \beta^{\frac{\mu}{(1-\mu)}} g(\beta^{\frac{1}{(1-\mu)}}) d\beta, \qquad (2.18)$$

in which we used the transformation $\sigma=\beta^{1/(1-\mu)}$. Once η is solved from (2.17), the integration (2.16) is performed using a combination of the trapezoidal rule and a Romberg extrapolation scheme. This integration is not straightforward since (2.13) gives s as function of σ, but in (2.15) σ as function of s is needed. This relation cannot be expressed explicitly, so once again Brent's method is used, in this case for finding σ for a given s. This happens in a similar way as described for the solving of (2.17). In this way the numerical solution for the moment on the valve is found.

An interesting secondary result of the von Mises model is the contraction coefficient κ, defined as (see also figure 2.2)

$$\kappa = \frac{\delta}{h_t} = \frac{h_0}{h_t}\,\eta^{\mu} . \qquad (2.19)$$

κ quantifies the deviation of the flow from a quasi one-dimensional one. In the quasi one-dimensional case $\kappa \equiv 1$ since a plug flow is assumed both before and behind the valve. Once η is solved, κ can be calculated straightforward. In table 2.1 κ is given for some orientations of the valve. From this table follows that, if the valve is far closed, the velocity far behind the valve is about 20% larger than in the quasi one-dimensional case. Since the pressure is proportional to the square of the velocity, the difference is then about 40%. Gurevich has also computed the contraction coefficients (see table 2.1). His results are interpolated by a sixth order polynom. The resemblance is close.

φ (°)	κ_G	κ
0	1.000	1.000
10	0.9323	0.9257
20	0.8705	0.8669
30	0.8155	0.8155
35	0.7907	0.7904

table 2.1: Contraction coefficient κ for several orientations of the valve. κ_G are values based on results of Gurevich (1965).

2.1.3 Finite element fluid model

In this section the numerical method, used for the discretization of the unsteady Navier-Stokes and continuity equations, is summarized. It has been implemented in the SEPRAN software package (Segal, 1984). More details can be found in appendix D and in Cuvelier et al. (1986).

Flow of an incompressible, Newtonian and isothermal fluid must satisfy the Navier-Stokes and continuity equations (1.1) and (1.2). To solve the velocity and the pressure from the momentum and continuity equations for $t > t_0$ in a domain Ω with boundary Γ, boundary and initial conditions are required. In their general form the boundary conditions read:

$$\left.\begin{array}{l} \vec{u}\cdot\vec{n} \text{ or } (S\cdot\vec{n})\cdot\vec{n} = \sigma_n \\ \vec{u}\cdot\vec{t} \text{ or } (S\cdot\vec{n})\cdot\vec{t} = \sigma_t \end{array}\right\} \text{are prescribed on } \Gamma \text{ for } t > t_0$$

with $\vec{n}$ the outward normal unit vector and $\vec{t}$ the tangential unit vector on Γ and S the Gauchy stress tensor. Furthermore as an initial condition the velocity field at $t = t_0$ must be prescribed:

$$\vec{u} \text{ prescribed on } \Omega \text{ for } t = t_0$$

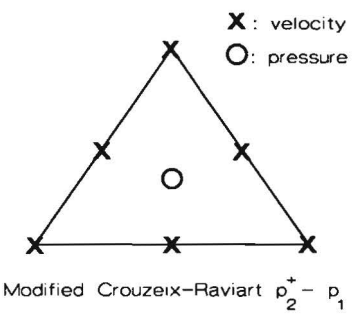

figure 2.3 Modified Crouzeix p_2^+-p_1 element, used for spatial discretization of the Navier-Stokes and continuity equations

To obtain an approximation of the velocity and the pressure field within a two-dimensional domain Ω, a standard Galerkin finite element method is applied. A 7-noded triangular Crouzeix-Raviart element, as shown in figure 2.3, is used (Cuvelier et al., 1986). The basis functions of the velocity are extended quadratic functions. Velocity unknowns are defined in all the nodal points. Pressure unknowns are only defined in the center of the element, which are the pressure itself and its spatial derivatives. The basis functions of the pressure are linear and discontinuous over the element boundaries. The advantage of this approach is that per element the continuity equation is satisfied. The velocity unknowns and the pressure derivatives within the centroid of the element are eliminated by consideration of the Navier-Stokes and continuity equations element-wise. This leads to a total amount of unknowns per element of 13. It can be shown that the element satisfies the Babuska-Brezzi condition (Cuvelier et al., 1986). The accuracy of the velocity is of

order Δx^3 and that of the pressure of order Δx^2, with Δx a characteristic element size. An example of a typical element mesh is given in figure 2.12.

The spatial discretization leads to a set of nonlinear first order differential equations:

$$\underline{\underline{M}}\,\dot{\underline{u}} + [\underline{\underline{S}} + \underline{\underline{N}}(\underline{u})]\underline{u} + \underline{\underline{L}}^T\underline{p} = \underline{f} + \underline{b} \qquad (2.20a)$$

$$\underline{\underline{L}}\,\underline{u} = \underline{0} \qquad (2.20b)$$

where $\underline{u}$ contains the velocity and $\underline{p}$ the pressure unknowns in the nodal points. $\underline{\underline{M}}\,\dot{\underline{u}}$ represents the local acceleration term, $\underline{\underline{L}}^T\underline{p}$ the pressure gradient term, $\underline{\underline{S}}\,\underline{u}$ the viscous term, $\underline{\underline{N}}(\underline{u})\,\underline{u}$ the convective acceleration term and $\underline{\underline{L}}\,\underline{u}$ the velocity divergence term. $\underline{f}$ and $\underline{b}$ represent the volume and boundary forces, respectively. In order to reduce the number of unknowns, a penalty function method is applied. The discretized continuity equation is replaced by:

$$\underline{\underline{L}}\,\underline{u} = \varepsilon\,\underline{\underline{M}}_p\,\underline{p} \qquad (2.21a)$$

or

$$\underline{p} = \frac{1}{\varepsilon}\,\underline{\underline{M}}_p^{-1}\underline{\underline{L}}\,\underline{u} \qquad (2.21b)$$

with $\underline{\underline{M}}_p$ the pressure matrix and ε a very small parameter. Substitution of this relationship into the discretized Navier-Stokes equation leads to:

$$\underline{\underline{M}}\,\dot{\underline{u}} + [\underline{\underline{S}} + \underline{\underline{N}}(\underline{u})]\,\underline{u} + \frac{1}{\varepsilon}\,\underline{\underline{L}}^T\underline{\underline{M}}_p^{-1}\underline{\underline{L}}\,\underline{u} = \underline{f} + \underline{b} \qquad (2.22)$$

which contains only unknowns for the velocity. The matrix $\underline{\underline{L}}^T\underline{\underline{M}}_p^{-1}\underline{\underline{L}}$ is singular (see appendix C). This singular matrix is multiplied by the large parameter $1/\varepsilon$ and added to the regular system matrix. Therefore, for too small values of ε the total system matrix becomes singular, whereas for too large values of this parameter the approximation of the continuity equation is not accurate enough. For the problems solved in this study the value of ε was chosen to be $\varepsilon=10^{-6}$, which leads to values of $\varepsilon\,\|\underline{p}\|$ of $O(10^{-6})$ in the dimensionless formulation which is in the order of the square root of the machine precision $\sqrt{\eta}$, $\eta = 10^{-15}$. More details are given by Cuvelier et al. (1986).

The local time derivative in (2.20) is approximated by the generalized trapezoidal rule:

$$\dot{\underline{u}}^{n+\theta} = \frac{\underline{u}^{n+1}-\underline{u}^{n}}{\Delta t} \tag{2.23a}$$

$$\underline{u}^{n+\theta} = \theta\,\underline{u}^{n+1} + (1-\theta)\,\underline{u}^{n} \tag{2.23b}$$

in which $\underline{u}^n$ is an abbreviation for $\underline{u}(n\Delta t)$ with Δt the time step. If $\theta = 1$ the method is equivalent to the Euler-implicit scheme, which is unconditionally stable and first order accurate in time. If $\theta = 0.5$, the method is a Crank-Nicolson scheme, which is also unconditionally stable and second order accurate in time. Although the Crank-Nicolson scheme has the highest order of accuracy, in this study $\theta = 1$ will be used. The motivation is found in the observation that, for reasons which are not completely clear yet, the computed pressure shows small oscillations around the correct values if a Crank-Nicolson scheme is used (van de Vosse, 1986&1987). Some attention to this phenomena will be paid in section 2.4. The restriction to a first order scheme is not inherent to the fluid-structure interaction algorithm itself (there are no objections for a higher order scheme), but is a result of a limitation of the fluid solver.

The nonlinear convective term $\underline{N}(\underline{u})\,\underline{u}$ in (2.20a) is linearized by a Newton-Raphson iteration scheme:

$$\underline{N}(\underline{u}^{i+1})\,\underline{u}^{i+1} = \underline{J}(\underline{u}^{i})\,\underline{u}^{i+1} - \underline{N}(\underline{u}^{i})\,\underline{u}^{i} \tag{2.24}$$

with i the index of the iteration step and $\underline{J}(\underline{u})$ the Jacobian matrix of $\underline{N}(\underline{u})\,\underline{u}$. Substituting equations (2.21), (2.22) and (2.23) into (2.20) leads to the final set of equations:

$$\left[\underline{M}/\Delta t + \underline{S} + \underline{J}(\underline{u}^{n+1,i}) + \frac{1}{\varepsilon}\underline{L}^{T}\underline{M}_{p}^{-1}\underline{L}\right]\underline{u}^{n+1,i+1} =$$

$$\underline{M}/\Delta t\,\underline{u}^{n} + \underline{N}(\underline{u}^{n+1,i})\,\underline{u}^{n+1,i} + \underline{f}^{n+1} + \underline{b}^{n+1} \tag{2.25}$$

At every time step a full Newton-Raphson iteration is carried out until

$$\max_{j} \|\underline{u}_{j}^{i+1}-\underline{u}_{j}^{i}\| < \delta_{newton} \tag{2.26}$$

with $\delta_{newton}=10^{-6}$. At every iteration step the system (2.25) is built and solved. The condition of the system matrix is bad, due to the use of the penalty function method. So without preconditioning, iterative methods are not suitable for solving the system

of equations. Here, a direct solving technique is used. The system matrix is asymmetric due to the contribution of the asymmetric convective matrix $\underline{N}$. Therefore, symmetric solvers like LDL^T- and GG^T-decomposition of the system matrix are not suitable here and one is forced to use an asymmetric LU-factorization technique (Cuvelier et al., 1986). Attempts have been made to reduce the number of iteration steps but experiments with simplified Newton schemes, when the Jacobian matrix is not updated every iteration step, did not result in a decreasing amount of computing time.

After convergence the pressure at t_{n+1} in the centroid of the element is computed from (2.21b) and its derivatives from the Navier-Stokes equation (Cuvelier et al., 1986). The normal and tangential stresses are interpolated to the element vertices. The total fluid moment acting on the valve is obtained by integrating the local stress over the valve. Since the stresses are known to vary linearly over each element, the fluid moment is integrated exactly (at least within the accuracy of the finite element discretization) in an analytical way.

As initial condition, the steady state solution for a fully opened valve is taken. The boundary conditions are prescribed according to figure 2.4. At the entrance, a fully developed parabolic axial velocity profile is prescribed and the radial flow is set to zero. The entrance channel is chosen to be long enough to guarantee a full development of the unsteady velocity profile. This fully developed entrance condition is used, although it does not correspond to the physiological one, since it facilitates the experimental verification. As contact condition on the valve, the fluid velocity is set equal to the local valve velocity, determined from the actual valve position and that at the previous point of time. At the outlet a stress free flow condition is prescribed.

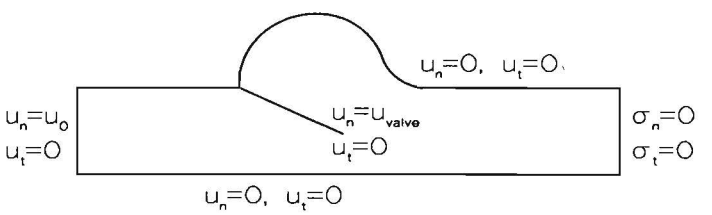

figure 2.4 Boundary conditions applied to the fluid

2.2 Structure model

The aortic valve is modeled as a two-dimensional chain consisting of a finite number (n) of rigid segments, with one degree of freedom each: their angle of rotation (figure 2.5). In the special case when n=1, the valve is completely rigid, rotatable only around its point of fixation. The following forces and moments are acting on the segments: buoyancy force, fluid force and bending moment in the contact points (figure 2.6). In figures 2.7 and 2.8 some segment quantities are defined. The inertia of the valve is neglected.

At each point of time a segment must satisfy the equilibrium conditions

$$f^i_{hx1} + f^i_{hx2} + f^i_{gx} + f^i_{fx} = 0 \tag{2.27a}$$

$$f^i_{hy1} + f^i_{hy2} + f^i_{gy} + f^i_{fy} = 0 \tag{2.27b}$$

$$(f^i_{gy} l^i_g + f^i_{hy2} l_i) \cos\varphi_i + (f^i_{gx} l^i_g + f^i_{hx2} l_i)\sin\varphi_i +$$

$$m^i_{b1} + m^i_{b2} + m^i_f = 0 \tag{2.27c}$$

with f_g the buoyancy force ,f_f the fluid force, f_h the hinge force respectively. l is the length of the segment and l_g the position of the center of mass. Index i refers to segment i, subscripts x and y refer to the horizontal and vertical directions, whereas 1 and 2 refer to the left and right edge, respectively. m^i_f denotes the moment about the contact point with segment i-1 due to the fluid flow. m_b is the bending moment in the contact points. The components of the buoyancy force are given by

$$\begin{aligned} f^i_{gy} &= \gamma_i l_i \cos\varphi_i \\ f^i_{gx} &= 0 \end{aligned} \tag{2.28}$$

with γ the effective weight per length. For the bending moment in the contact points it is assumed that it can be described by

$$m^i_b = \sum_{k=0}^{p} \beta_{ki}(\varphi_i - \varphi_{i-1})^k \tag{2.29}$$

The parameters γ_i, l_{gi} and β_{ki} will be determined experimentally, accompanied with some additional assumptions. This will be discussed in chapter 3. The fluid forces

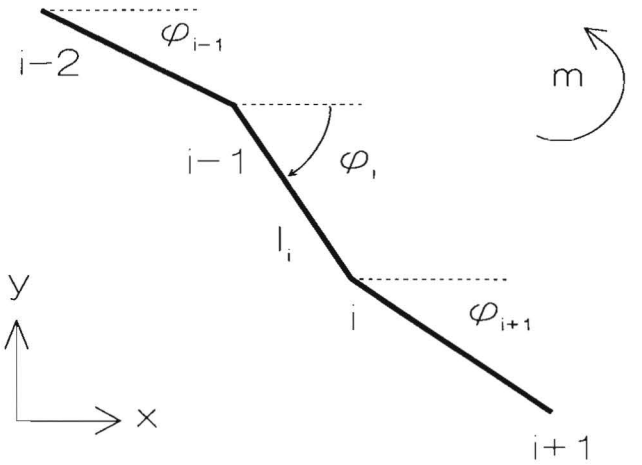

figure 2.5 Definition of the geometry of a segmented valve

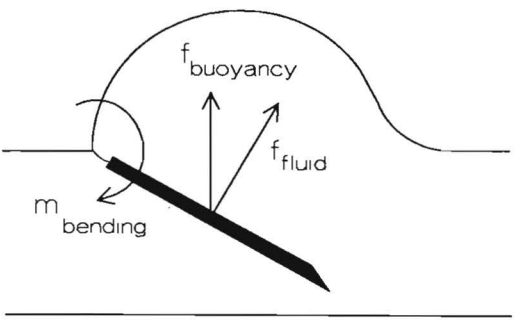

figure 2.6 Forces acting on a valve

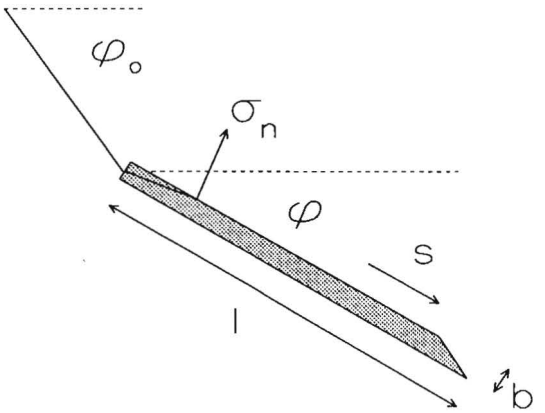

figure 2.7 Definition of some parameters of a rigid valve

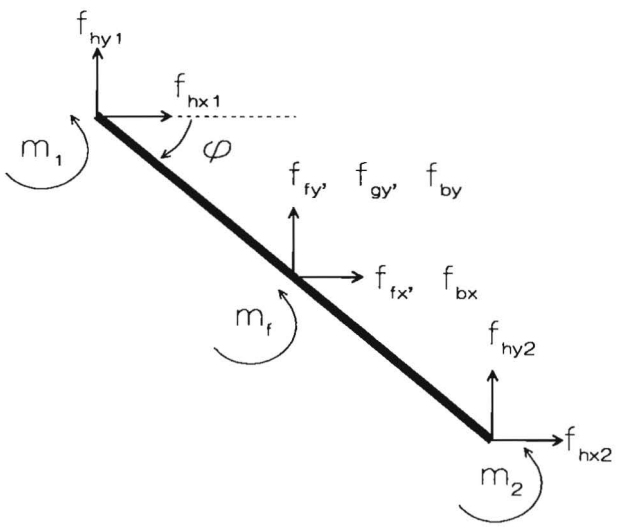

figure 2.8 Definition of forces, acting on a segment of a segmented valve

and moments must be calculated by one of the fluid models from section 2.1. On the segment edges the contact conditions

$$f^i_{hx2} = -f^{i+1}_{hx1} \tag{2.30a}$$
$$f^i_{hy2} = -f^{i+1}_{hy1} \tag{2.30b}$$
$$m^i_{b2} = -m^{i+1}_{b1} \tag{2.30c}$$

are imposed. The boundary conditions for segment n

$$f^n_{hx2} = 0 \tag{2.31a}$$
$$f^n_{hy2} = 0 \tag{2.31b}$$
$$m^n_2 = 0 \tag{2.31c}$$

complete the set of equations. For an arbitrary set φ_i (i=1,n) the system is not in equilibrium. For those states a residual moment m^i_{res} per segment is defined as

$$m^i_{res} = (f^i_{gy}l_{gi} + f^i_{hy2}l_i)\cos\varphi_i + (f^i_{gx}l_{gi} + f^i_{hx2}l_i)\sin\varphi_i + m^i_{b1} + m^i_{b2} + m^i_f \tag{2.32}$$

The unknown contact forces can be calculated in a recursive way:

$$f^i_{hx1} = f^{i+1}_{hx1} - f^i_{gx} - f^i_{fx} \tag{2.33a}$$

$$f^i_{hy1} = f^{i+1}_{hy1} - f^i_{gy} - f^i_{fy} \tag{2.33b}$$

Starting from the valve tip, where boundary conditions (2.31) can be applied, the contact forces f^i_{hx} and f^i_{hy} can be calculated for every segment with (2.33), which in turn can be substituted in (2.32). This leads, together with (2.29) and (2.30) and expressions for the fluid moment and forces from section 2.1, to n equations with unknowns φ_i (i=1,n).

The desired equilibrium state is achieved when all the residual moments (2.32) are zero. This state cannot be found directly because the resulting set of equations can be strongly nonlinear. When a finite element fluid model is applied it is even essentially impossible, since no explicit expression for fluid forces and moments can be given. Therefore, an iterative solving procedure must be used. This is subject of the next section.

2.3 Fluid-structure interaction models

In sections 2.1 and 2.2 several models for fluid and structure have been introduced. They have been treated separately, without taking into account the interaction between them. In this section two models are presented which provide for the interaction between fluid flow and structure motion. The first one is suitable for a rigid valve, which has only one degree of freedom. In that case, the valve equilibrium position is equivalent to the root finding of a nonlinear scalar equation. This approach is not suitable for a segmented valve, which has more degrees of freedom. Therefore, the equilibrium search is reformulated as a minimization problem. Both methods are iterative ones and make an explicit attempt to combine robustness with efficiency.

2.3.1 Single degree of freedom

In section 2.2 the search for the equilibrium position of a rigid valve in a fluid flow is reduced to the root finding of a nonlinear function with one independent variable, say

$$m(\varphi) = 0 \tag{2.34}$$

Since the function is nonlinear, an iterative method is necessary which is expected to result in a sequence $\varphi_0,\ldots,\varphi_j$ with given initial estimate φ_0 and

$$\lim_{j\to\infty} \varphi_j = \alpha \tag{2.35}$$

$$m(\alpha) = 0 \tag{2.36}$$

In general, $m(\varphi)$ may have more roots. If m has only one root then the equilibrium position of the valve is unique. For the solution of such nonlinear scalar equations, a number of methods exists. An important feature of such methods is the order of convergence ρ defined as the largest value of ρ for which the limit

$$\lim_{j\to\infty} \frac{|\varphi_{j+1} - \alpha|}{|\varphi_j - \alpha|^{\rho}} = \kappa \qquad 0 \le \kappa < 1 \tag{2.37}$$

exists. If ρ=1 and $\kappa > 0$ the convergence is linear, if ρ=1 and κ=0 or if ρ>1 it is superlinear. Another important consideration is the fact that the derivative of m with

respect to φ can not be evaluated. A very suitable method for this study is the method of van Wijngaarden & Dekker, later improved by Brent (1973). For brevity it will be referred to as *Brent's method*. In this study, a modified version of the source code, supplied by Press et al. (1985) is used.

Brent's method guarantees global convergence to a root of arbitrary nonlinear equation. It is never significantly slower than the classical bisection method ($\rho = 1$ and $\kappa = 0.5$). Moreover, a fast superlinear convergence is obtained close to roots of continuously differentiable functions ($\rho = \frac{1}{2}(1+\sqrt{5}) \approx 1.62$). Essentially, the method is a combination of bisection and successive interpolation. In this way it combines robustness with fast convergence. A brief outline of the method is given in appendix E. A discussion of its merits is given by Press et al. (1986).

Brent's method guarantees convergence only if the root is initially bracketed. That leaves the problem how to bracket it. There is no general solution for this problem. The strategy of choice heavily depends on the features of the function involved. Important factors are the bounds of the regions on which the function is defined, the existence of multiple roots and singularities and the computational effort required for the evaluation of the function.

The fluid moment is expected to be a regular smooth monotonic function of position. Furthermore, one bracketing interval is a priori known: the equilibrium position *must* be somewhere between the fully opened en fully closed position. So, at first sight the problem is simple: use Brent's method with both extreme positions as starting interval. However, some practical points and some principal problems must be considered.

The motion of the valve can be expected to be a smooth function of time, since the physiological flow rate variations are also smooth. So, the equilibrium position of the previous time step will be a fair estimate for the solution on the next. This will improve the convergence of the Newton iteration for the fluid flow, since it is very sensitive to the quality of the initial estimate. On the other hand, it will also speed up the Brent iteration procedure for the valve position, since close to the root superlinear convergence may be expected. In order to take advantage of the computational work done in the previous time steps, it is important to avoid unnecessary jumps far from the solution. It is especially important to limit the evaluations for a relatively far closed valve, since the further the valve is closed the harder the fluid flow can be solved. Then, finer element meshes and more Newton iteration steps are necessary. On the other hand, care must be taken that the bracketing is carried out fast enough, otherwise the bracketing of the root would be far more expensive than the final convergence to it. 'Going downhill' with a

sequence of careful, small steps can easily be too costly.

The bracketing method which is applied in this study is a restricted extrapolation. As a first estimate the solution of the previous time step is taken. The sign of the moment is tested and as a second estimate a trial step is taken in the direction in which the valve is being pushed. Then a linear extrapolation is performed and the next estimate is taken somewhat further than the zero crossing of the extrapolating line, in order to increase the chance that the root is bracketed indeed. Both the extrapolating step and the extrapolated position are restricted to predefined limits. Successive linear extrapolation is performed until the root is bracketed. The bracketing and interpolation process is illustrated in figure 2.9.

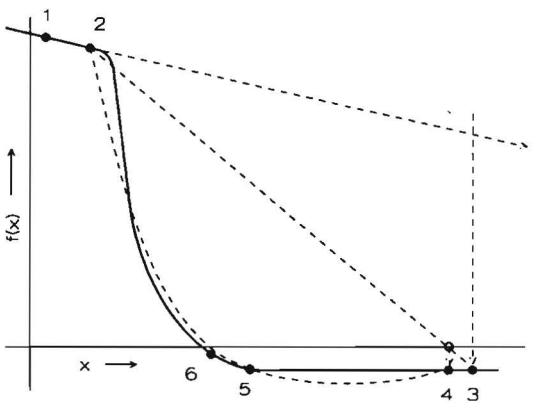

1: Initial estimate
2: Trial step
3: Restricted extrapolation
4: Interpolation
5: Bisection
6: Interpolation

figure 2.9 Diagram of the bracketing and interpolation procedure, used for the convergence to the equilibrium position of a rigid valve

2.3.2 Multiple degrees of freedom

The set of equilibrium conditions for a multi-segment valve (section 2.2) results in a set of n nonlinear equations of n unknowns φ_i. This set of equations is solved by reformulating the problem as a nonlinear least squares problem. Define a residual moment

$$r(\varphi) = \sum_{i=1}^{n} m_i^2(\varphi) \qquad \varphi^T = [\varphi_1,\ldots,\varphi_n] \tag{2.38}$$

where r is total residual moment to be minimized and m_i the moment, acting on segment i, which is a function of a position set φ. Once a minimum of r is found which equals zero, φ contains the equilibrium position of the valve segments and therefore of the valve itself. The segment moments m_i depend on all $\varphi_0,\ldots\varphi_n$. In general no explicit relation for this dependence can be given, especially not when the finite element fluid model (section 2.1.3) is used. A consequence is that derivatives cannot be calculated. Therefore, a method must be used which does not require the evaluation of derivatives. A very suitable nonlinear least squares method for this study is *Powell's hybrid method* (Powell, 1970, implemented in the NAG-library).

Since the problem is nonlinear, the method is an iterative one. Essentially, it is a combination of the classical Gauss-Newton and steepest-descent methods. The Gauss-Newton method converges superlinearly close to minimum, but far from the minimum the convergence can be poor or even absent. The steepest-descent method is much more robust, but its convergence is in general slow. Each next iteration step is a mixture of a Gauss-Newton step and a steepest-descent step. This mixture is controlled by a comparison of the actual reduction, obtained in the previous iteration steps, and the predicted reduction, assuming the residual to be quadratic. If the progress is poor, the steepest-descent step is favored, otherwise the Gauss-Newton step is. At the start of the iteration, the derivatives of the segment moments with respect to the segment positions are approximated by finite differences. Later, the derivative information is updated, using the function evaluations only, by assuming that the segment moments m_i depend linearly on φ (Broyden's rank-one update).

Like Brent's method (section 2.3.1), Powell's method combines a robust convergence far from the equilibrium position, with a fast, superlinear convergence close to it. The well-known Newton-Raphson method for the solution of sets of nonlinear equations lacks this type of robustness and is therefore not applied here.

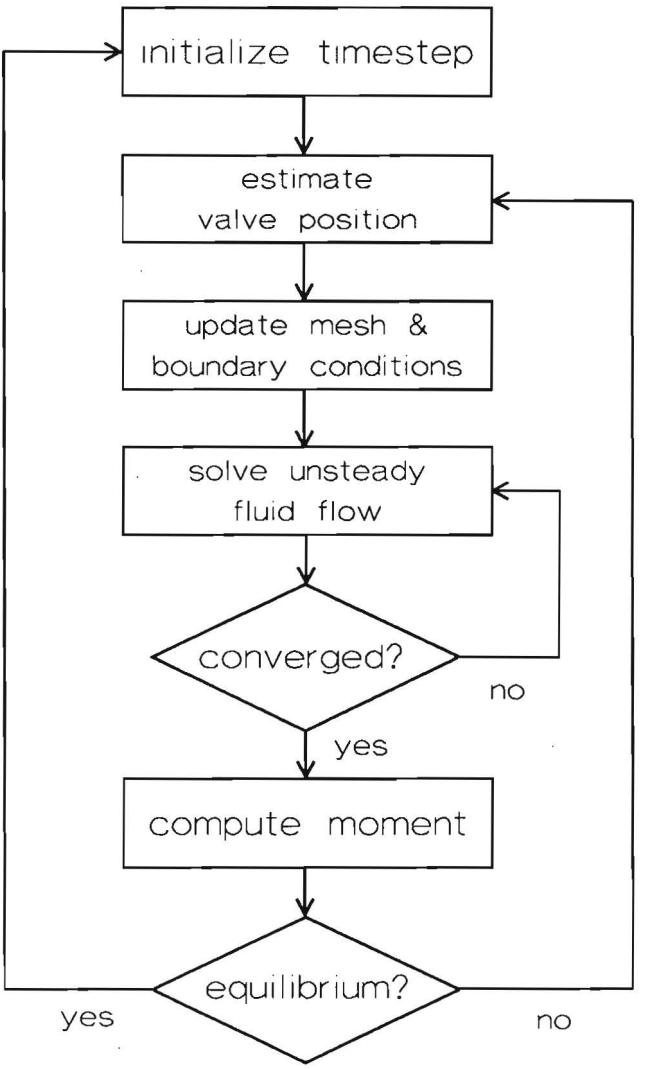

figure 2.10 **Flow chart of the fluid-structure interaction algorithm for each timestep**

More details of Powell's hybrid method are given in appendix E and in Powell (1970) and Scales (1985).

Notwithstanding the robustness of Powell's hybrid method, occasionally it fails to find the equilibrium position. In these cases, a new initial estimate is generated and the iteration process is restarted.

2.3.3 Summary of algorithm

A summary of the resulting algorithm is given in the flow chart of figure 2.10. It is valid for both the rigid and segmented valve.

At the start of each time step some initializations are performed. As an initial estimate for the valve position the position at the previous time step is taken. Then, the finite element mesh is updated and the fluid boundary conditions at the fluid-valve contact surface are updated. The valve velocity is obtained from a straightforward finite difference approximation using its positions on the previous and the current timestep. The normal fluid velocity at the contact surface is set equal to the local valve velocity. The tangential fluid velocity is set to zero.

Next, the fluid velocity field is solved. Since this is a nonlinear problem, a Newton-Raphson iteration is used. If the velocity field is known, the pressure and shear stresses in the element centroids are computed and interpolated to the element vertices. The fluid moment acting on each segment is obtained by integrating the fluid stresses. Then it is checked whether they are in equilibrium with the bending and buoyancy moments. If not, a new valve position estimate is generated using Brent's method or Powell's hybrid method. This is proceeded until the valve is in equilibrium. Then the algorithm proceeds with the next timestep.

2.4 Numerical tests

In this section some aspects of the accuracy of the solution and of convergence and efficiency of the methods are considered.

2.4.1 Finite element mesh

The spatial discretization of the fluid domain into finite elements introduces a truncation error for the velocity solution which is of order $(\Delta x)^p$ with Δx a characteristic element size. If the mesh is refined, so that Δx decreases, the solution of a discretized linear system is expected to converge to the exact solution according

to

$$\lim_{\Delta x \to 0} \frac{\|\underset{\sim}{u}_1 - \underset{\sim}{u}_2\|}{\|\underset{\sim}{u}_2 - \underset{\sim}{u}_4\|} = 2^{\rho} \tag{2.39}$$

with $\underset{\sim}{u}_1=\underset{\sim}{u}(\Delta x)$, $\underset{\sim}{u}_2=\underset{\sim}{u}(\Delta x/2)$ and $\underset{\sim}{u}_4=\underset{\sim}{u}(\Delta x/4)$ and $\| \ \|$ some norm. In order to verify the convergence, as norm a discrete L_2-norm is used, according to

$$\|\underset{\sim}{u}\| = \{\frac{\sum_{i=1}^{n} u_i^2}{n}\}^{1/2} \tag{2.40}$$

with n the number of degrees of freedom. Figure (2.11) shows two of the element meshes which are used for this verification. The element distribution is approximately equidistant and the elements are refined by a factor 2 in each direction at each refinement step. Tables 2.2 shows that the velocity indeed converges if the mesh is refined, with $\rho \approx 2.1$. Table 2.3 shows that the fluid moment converges with $\rho \approx 1.4$.

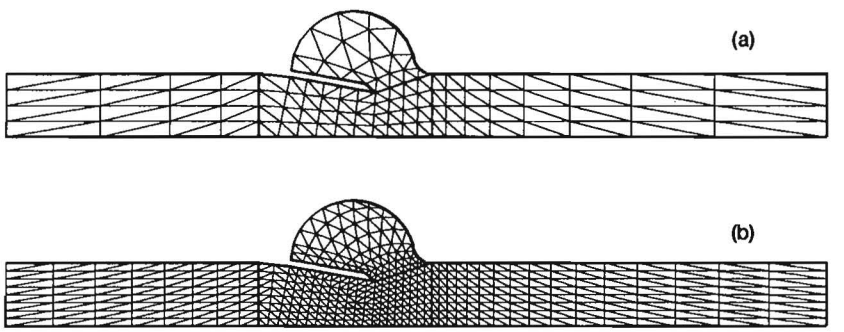

figure 2.11 Finite element meshes used for checking the convergence in the element mesh (a) reference mesh Δx (b) refined mesh $\Delta x/2$

The difference between the velocity solution on the coarsest and that on the finest mesh is only 0.3%, so the coarse mesh is expected to give results for the velocity field with sufficient accuracy for the purpose of this study. This is not true for the fluid moment. The differences between the solution obtained with different mesh distributions increases to 26% at Re = 500, probably due to discretization errors. The

use of a very fine element mesh is not acceptable since it requires an amount of computing time which is too large for an application combined with the iterative fluid-structure interaction algorithms. The accuracy of the coarse mesh can be improved by choosing the element distribution according to figure 2.12 while keeping the number of unknowns approximately equal. The difference between the fluid moment of the optimized mesh and the finest mesh ($\Delta x/4$), which is taken as the reference case, is -0.2% at Re = 100, 4% at Re = 300 and 9% at Re = 500 (see table 2.3). This suggests an acceptable accuracy for the optimized mesh at low values of the Reynolds number, but some care must be taken at higher values. In chapter 4, the computation of the fluid moment will be validated by a comparison with experimental data.

$\|\underset{\sim}{u}_1\|$	0.7448665
$\|\underset{\sim}{u}_2\|$	0.7430119
$\|\underset{\sim}{u}_4\|$	0.7426367
$\|\underset{\sim}{u}_1-\underset{\sim}{u}_2\|$	0.0126023
$\|\underset{\sim}{u}_2-\underset{\sim}{u}_4\|$	0.0029955
ρ = 2.07	

table 2.2 Convergence of velocity if mesh is refined ($\underset{\sim}{u}_1$: velocity from standard characteristic mesh size Δx_s; $\underset{\sim}{u}_2$: $\Delta x = \Delta x_s/2$; $\underset{\sim}{u}_4$: $\Delta x = \Delta x_s/4$)

	Re=100	Re=300	Re=500
m_{f1}	0.70602	4.95348	13.19103
m_{f2}	0.66355	4.44402	11.22894
m_{f4}	0.64762	4.18953	10.44877
ρ	1.42	1.37	1.33
m_{fo}	0.64632	4.35066	11.38194

table 2.3 Convergence of the fluid moment m_f if the mesh is refined isotropically (m_{f1}: standard characteristic mesh size Δx_s; m_{f2}: $\Delta x = \Delta x_s/2$; m_{f4}: $\Delta x = \Delta x_s/4$) and the fluid moment m_{fo} resulting from the optimized mesh

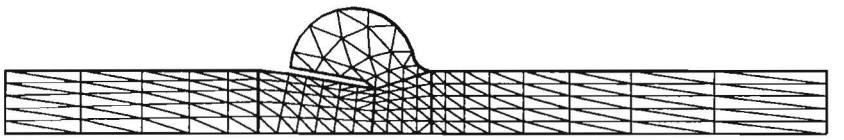

figure 2.12 Optimized finite element mesh, used in the remainder of the study

2.4.2 Time discretization

The time integration is tested for the situation of a rigid valve in a fixed position when flow rate is pulsatile. First, the velocity field is solved and then the fluid moment is computed by integration of the pressure and shear stress over the valve. Figure 2.13 shows the fluid moment obtained by the Euler-implicit and Crank-Nicolson methods for two different time steps.

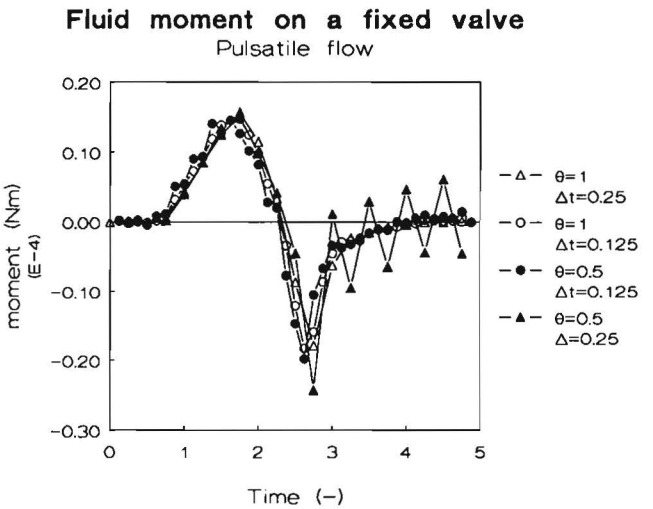

figure 2.13 Numerically computed moment on a fixed valve due to a pulsatile flow rate as a function of time for different time integration parameters

As mentioned before, the implementation of the Crank-Nicolson method in the finite element model exhibits oscillations in the pressure. For a small timestep (Δt=0.125) the oscillations are small but significant. For a somewhat larger timestep (Δt=0.25) the course of the pressure starts smooth, but after the sharp dip of the

deceleration phase, a large oscillation is initiated which continues during the computation (in this case the first computed period is shown). The origin of these oscillations is not yet fully understood. It is assumed that they are caused by the use of the penalty function method. Small fluctuations in the velocity solution which occur during the computation can not be eliminated or damped by the Crank-Nicolson method. These oscillations themselves are small. However, the pressure is computed from (2.21b), so the pressure oscillations are a factor $1/\varepsilon=10^6$ larger than those of the velocity. For computation of the fluid field alone, without any fluid-structure interaction, these oscillations are not troublesome, since they can be eliminated effectively by applying a two-step method which gives the pressure at the intermediate time levels $t = (n+\frac{1}{2})\Delta t$ (van de Vosse, 1987). In cases *with* fluid-structure interaction, this two-step method can not be applied since the fluid moment, and therefore the fluid pressure, at the time levels $t = (n+1)\Delta t$ are required.

If the Euler-implicit scheme is used, no oscillations are observed. A slight difference occurs if the time step is changed, indicating the presence of numerical damping due to the first order truncation error. Since this difference is small and since the solution is close to that of the second order accurate Crank-Nicolson method, the numerical damping is only small here. Therefore, the Euler-implicit method with $\Delta t=0.25$, is found to be of sufficient accuracy for this study.

2.4.3 Convergence

In the algorithm, several iteration methods are used. In this section the convergence of these methods is verified.

A Newton-Raphson iteration is applied for the linearization of the nonlinear convective term of the Navier-Stokes equation. Its theoretical order of convergence, as defined by equation 2.37, is $\rho = 2$. The actual convergence may be judged from the analysis of the behavior of the expression

$$\lim_{j\to\infty} \frac{\|\underline{u}_{j+2}-\underline{u}_{j+1}\|}{\|\underline{u}_{j+1}-\underline{u}_{j}\|^{\rho}} = \kappa \qquad (2.41)$$

with $\|\ \|$ chosen according to (2.40). ρ is equal to the slope of a linear fit in a plot of $\|\underline{u}_{j+1}-\underline{u}_{j}\|$ against $\|\underline{u}_{j+2}-\underline{u}_{j+1}\|$ on a log-log scale. The convergence process is shown in figure 2.14. A superlinear convergence is observed, with a convergence rate close to the theoretical expected one, until the subsequent difference between two iteration steps is decreased to about 10^{-9}. Due to the truncation errors in the finite element

discretization and to the finite machine floating point precision (10^{-15}) the solution does not converge any further. In the remainder of this study, the Newton iteration is stopped when the difference between the solutions of two successive iteration steps is less then 10^{-6}, since this appears to yield a sufficient accuracy.

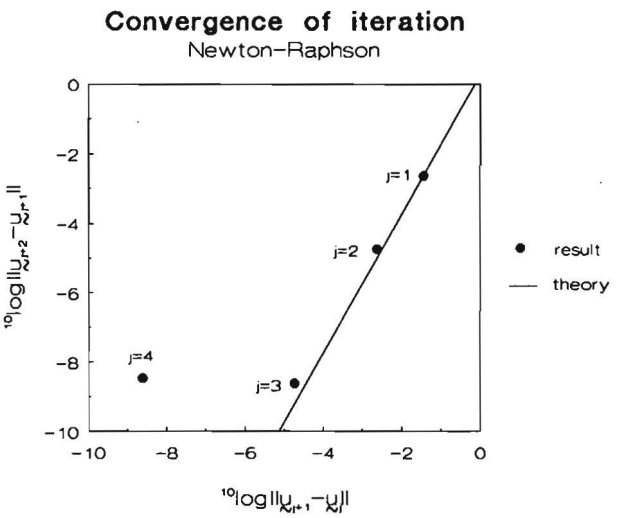

figure 2.14 Convergence test of the Newton-Raphson iteration method, which is applied to solve the set of finite element fluid equations (steady flow, Re=100). j corresponds to the iteration index.

The order of convergence of the Brent iteration is expected to be approximately that of the successive linear interpolation method (secant method), i.e. $\frac{1}{2}(1+\sqrt{5}) \approx 1.62$. The actual convergence is shown in figure 2.15. First, the convergence is checked for the Brent iteration in combination with the analytical quasi one-dimensional fluid model, whose solution is not subjected to truncation or discretization errors. The convergence continues until the difference between two successive iteration steps is in the order of the machine precision. The order of convergence is very close to the theoretical one. If the Brent iteration is used together with the finite element fluid model, the difference between successive iteration steps can not be further decreased than about 10^{-8}, which is approximately the square root of the machine precision. The convergence process is slightly slower than for the analytical fluid model. Especially, beyond a subsequent difference of 10^{-6} the convergence becomes slower. In this study, the Brent truncation criterion is chosen to be 10^{-6}.

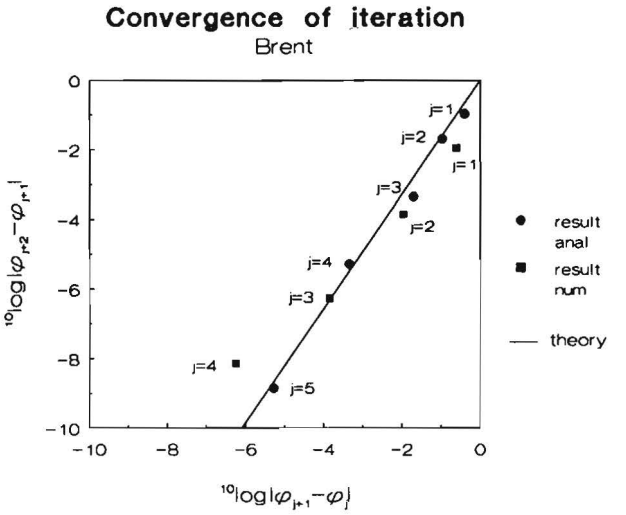

figure 2.15 Convergence test of Brent's method, which is applied to find the equilibrium position of a rigid valve, combined with the quasi one-dimensional analytical and finite element numerical models (steady flow, Re=100). j corresponds to the iteration index.

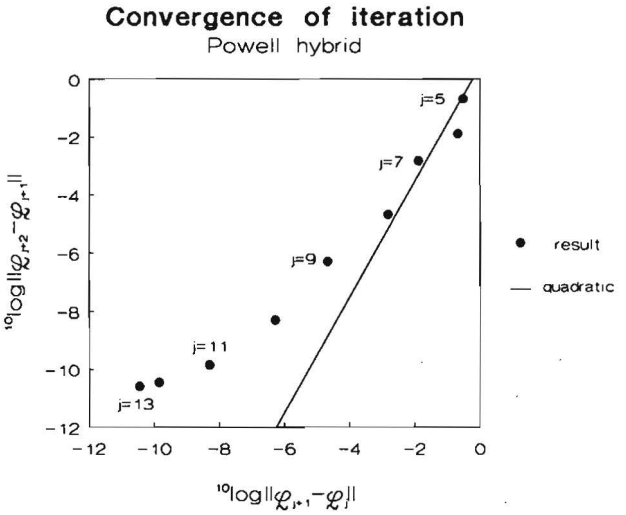

figure 2.16 Convergence test of Powell's hybrid method, which is used to find the equilibrium position of a segmented valve (4 segments) in combination with the finite element fluid model (steady flow, Re=100). j corresponds to the iteration index.

The convergence behavior of Powell's hybrid method is similar to that of Brent's method (figure 2.16). After some initial iteration steps, required for the estimation of the Hessian matrix (j=1,4, not shown in figure 2.16), the convergence is superlinear until a subsequent difference of 10^{-8} (the square root of the machine precision) is achieved. After this point the convergence slows down. The subsequent difference can not be diminished further than about 10^{-10}. As a truncation criterion 10^{-8} is chosen.

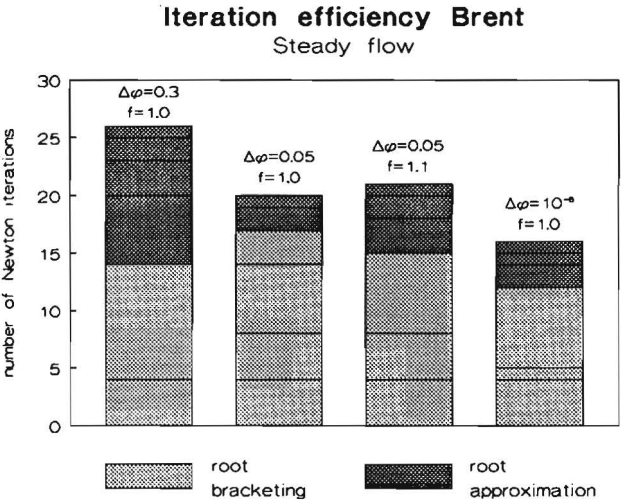

figure 2.17 Cumulative number of Newton iterations required by the finite element fluid model in order to find the equilibrium position of a rigid valve in a steady flow for various bracketing strategies ($\Delta\varphi$:trial step, f: extrapolation factor, Re=300, first estimate φ=0.0,, equilibrium position φ=0.2380, truncation criteria: $\delta_{newton}= 10^{-4}$, $\delta_{brent}=10^{-4}$)

If the finite element fluid model is applied, a Newton iteration is required for each Brent or Powell iteration step, i.e. for each position estimate. In this study, the computation time is dominated by the solving of the fluid equations. Therefore, the computational effort is directly proportional to the number of Newton iterations per timestep. Figure 2.17 shows the number of Newton iterations in case of a steady flow for various bracketing strategies. In this case 6 position estimates and between 16 and 26 Newton iteration steps are required, which are typical numbers for steady flow cases. From figure 2.17 it is evident that the required number of position estimates for the root bracketing equals that for the accurate approximation by Brent's method. Nevertheless, most computational effort is used for the root

bracketing. The total effort depends quite strongly on the bracketing procedure. If a large arbitrary estimation step $\Delta\varphi$=0.3 is chosen, 26 Newton iteration are required. This is decreased to 16 if the step is chosen as $\Delta\varphi$=10^{-6}, which is a gain of 38%. So a careful trimming of the bracketing parameters can reduce the computational effort.

If Brent's method is applied to a case with a pulsatile flow rate, as shown in figure 2.18, the result is similar to that of the steady flow case. About 20 Newton iteration steps per timestep are required. The trimming of the bracketing parameters is somewhat more complicated, since the valve displacement per timestep varies strongly during the flow cycle. As might be expected, the computational effort is smaller if the valve velocity is modest (during diastolic phase and in maximal opened position, which is just after the flow rate maximum as will be shown in chapter 4) than when the valve is accelerated (during flow acceleration and deceleration).

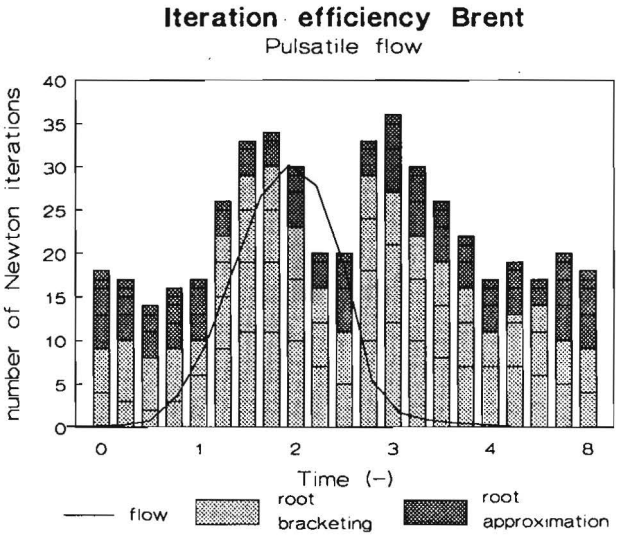

figure 2.18 Cumulative number of Newton iterations required by the finite element fluid model in order to find the dynamic equilibrium position of a rigid valve in a pulsatile flow (Re=313, St=0.69, truncation criteria: δ_{newton}= 10^{-4}, δ_{brent}=10^{-6}, initial bracketing step $\Delta\varphi$=0.03, zero bending moment and buoyancy force)

Figure 2.19 shows the computational effort if Powell's hybrid method is applied. It appears that for a valve of only one segment (which is in fact a rigid valve) Powell's minimization method is only slightly less efficient than Brent's root finding method. Powell's method requires 11 position estimates, whereas for Brent's method only six are sufficient, but the amount of Newton iterations is comparable. This is in

contrast to what was expected, since Brent's method is able to use the signs of the evaluated function values, thus having more information available than Powell's method, which takes only the magnitude into account. Apparently, Powell's method behaves more subtle if the iteration process is still far from the solution. The maximum step which might be taken is carefully controlled by the algorithm itself, resulting in smaller steps than the bracketing method used for Brent's method. The smaller the position step is, the better is the initial estimate of the fluid velocity field for the Newton iteration process. Powell's method requires about 1.7 Newton steps per position estimate, whereas the bracketing+Brent method requires at least 2.7 steps. The computational effort increases with the number of valve segments. For one segment 11 positions estimates and 19 Newton steps are used, whereas a valve of sixteen segments needs 52 position estimates and 70 Newton steps. This increase is fairly modest and is less than for various classical methods, for which the number of function evaluations (i.e. position estimates) is approximately proportional to the number of degrees of freedom (number of segments) (Box,1966)

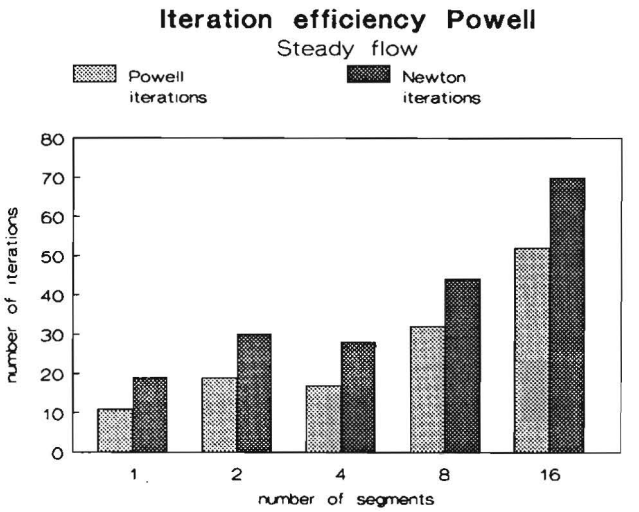

figure 2.19 Cumulative number of iterations required to find the equilibrium position of a segmented valve in a steady flow for various numbers of segments (Re=300, first estimate φ=0.0,, equilibrium position φ=0.2380, truncation criteria: $\delta_{newton}= 10^{-4}$, $\delta_{powell}=10^{-8}$)

2.5 Discussion

Each of the interaction methods for a rigid or a segmented valve can be combined with a particular fluid model, thus resulting in a variety of model evolutions. As will be obvious and as will be shown in chapter 4, the finite element method yields the most versatile and accurate fluid model. The computations are performed on an Apollo-DN3000 minicomputer and on an Alliant FX/4 mini-supercomputer with two parallel vector processors.

The interaction algorithm inherently satisfies the physical equilibrium conditions and the contact conditions at the fluid-structure interface. Since the fluid flow is integrated in time with an unconditional numerical stability and since the structure at the end of each timestep is guaranteed to be in equilibrium with the fluid, an unconditional numerical stability for the total algorithm may be expected.

In this study it is assumed that the equilibrium situation of the fluid-structure system is a unique one. In general, this condition is not necessarily satisfied. The structure may have more than one (local) equilibrium position or bifurcations in the fluid or structure solution may occur. Since the Reynolds number is rather low ($Re \leq 1000$), fluid flow bifurcations are not expected. The valve is always exposed to external fluid stresses, so it is likely that the solution of the structure will be well determined. The initial estimate at each timestep (the solution at the previous one) will be not far away from the equilibrium position, since the fluid moment is continuous in time. Therefore, if a minimum of the residual moment is found (which equals zero), it is very likely that it is indeed the correct equilibrium position. The existence of the solution is in the problem at hand not a point of discussion, since it is known that the valve *must* be somewhere between the fully opened and fully closed position. Because of these considerations, in this study no special care is taken to avoid the problems mentioned above.

The applied trial and error mesh optimization method yields an element distribution which is approximately optimal for the specific geometry and flow under consideration. A more advanced optimization method would be an adaptive mesh strategy, in which the mesh is adapted in every situation in such a way that the spatial discretization error is distributed homogeneously over the domain.

In the structure model, elastic, visco-elastic and inertial effects are not taken into account. This simplification is not inherent to the algorithm, but it is induced by the subject of study, in which these phenomena are not relevant. Elasticity and visco-elasticity can readily be incorporated in the structure equilibrium equations. If a

more sophisticated model is required, the equilibrium of the structure may be evaluated by a finite element method. If inertial effects are relevant, the equilibrium condition of a segment can be generalized according to the familiar equation

$$\Sigma m = j_v \ddot{\varphi} \tag{2.42}$$

with j_v the moment of inertia of the valve and $\ddot{\varphi}$ the angular acceleration. The second order time derivative can de discretized by either

$$\ddot{\varphi}^{n+1} = [\varphi^{n+1} - 2\varphi^n + \varphi^{n-1}]/\Delta t^2 + O(\Delta t) \tag{2.43}$$

or, if a second order accurate fluid solver is used,

$$\ddot{\varphi}^{n+1} = [2\varphi^{n+1} - 5\varphi^n + 4\varphi^{n-1} - \varphi^{n-2}]/\Delta t^2 + O(\Delta t^2) \tag{2.44}$$

These expressions can be verified by using Taylor series expansions.

Extension of the analytical fluid models to moving valves can easily be developed, especially with respect to the quasi-one-dimensional model. Since this is not of primary interest in this study, no further attention is paid to such extensions.

3. EXPERIMENTS

The theoretical models, introduced in the previous chapter, will be validated by means of a comparison of theoretical predictions to experimental results. In sections 3.1 through 3.3 the experimental setup is described. Section 3.4 gives the results of some experimental tests. Finally, the estimation of the valve parameters and its impact on the accuracy of the computed valve equilibrium position are described in sections 3.5 and 3.6.

3.1 Experimental setup

The experimental setup is shown in figure 3.1. The flow system consists of three reservoirs and a steady pump, maintaining a constant pressure difference. The flow rate in the actual model is regulated by an electrically controlled motor valve. Behind the valve a diffusor is present in order to break down vortices. The inlet length before the model is long enough to ensure that the flow is fully developed and laminar, in both steady and unsteady cases. As fluid water is used, to which 0.05% of an oil emulsion (Dromus Shell, normally used as cooling fluid during drilling and milling) is added as seeding for laser Doppler measurements. 0.0002% $CuSO_4$ is added to prevent the growth of micro-organisms.

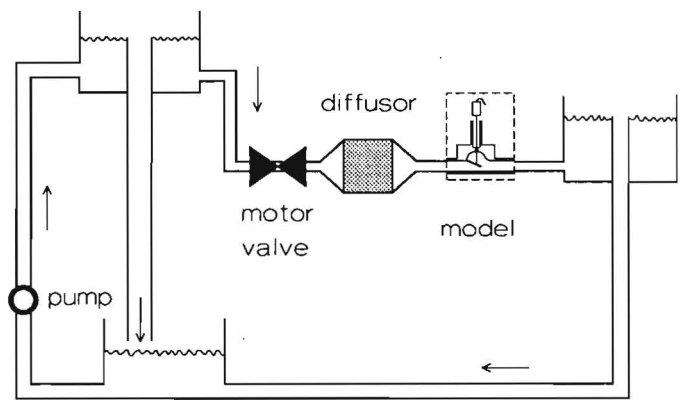

figure 3.1 Diagram of the experimental setup

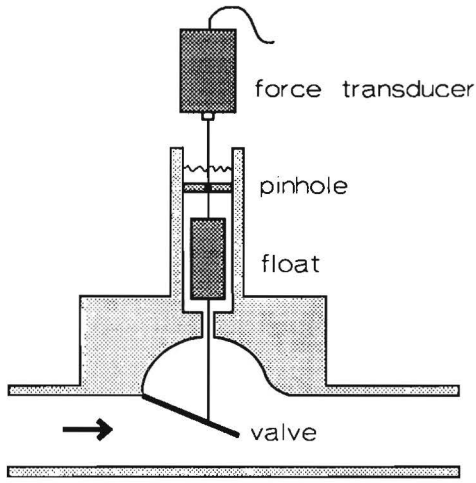

figure 3.2 Detail of the experimental rigid valve model. A similar setup is used for a segmented valve

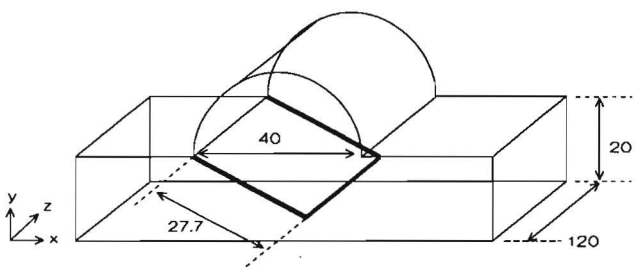

figure 3.3 Three-dimensional sketch of the experimental aorta model (sizes are in mm)

The aorta model is shown in some more detail in figure 3.2. Valve, aorta and sinus can be recognized. A sketch of the three-dimensional shape is given in figure 3.3. The channel height is 20 mm. The ratio of height to depth is 1:6 in order to create a situation which is approximately two-dimensional.

In the remainder of this study, two different experimental situations will be considered. The first is that of the valve held in a fixed position. In this situation a force transducer is mounted to the valve, which measures the forces acting on the valve by the fluid flow, the buoyancy and/or the membrane. An adjustable float prevents the force transducer from being overloaded. Especially in the unsteady flow case, some leakage flow through the connection hole in the top of the sinus is present. In order to minimize this flow, an adjustable pinhole is present. The diameter of the transducer rod is 1.5 mm, the diameter of the pinhole 1.9 mm. This choice is a compromise between the minimization of the leakage flow at one hand and of the friction between rod and pinhole at the other. By measuring the rise of the fluid level in the vertical tube, it is estimated that the leakage flow rate is about 0.2-0.4% of the aorta flow rate.

The second experimental situation is that of a valve which is allowed to move freely in the fluid. In this case the valve will always be in dynamical equilibrium with the fluid. The position and motion of the valve will be registered.

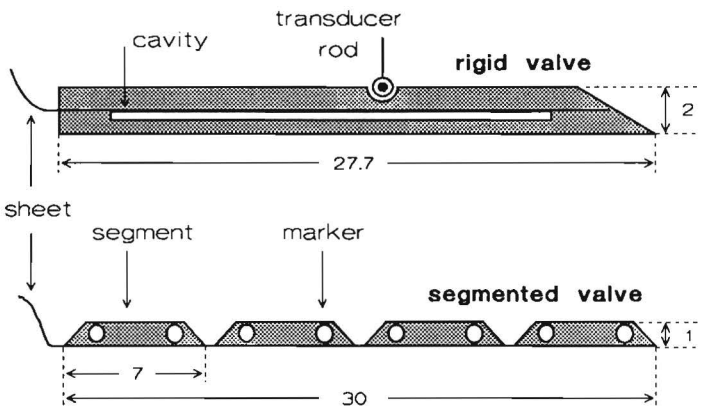

figure 3.4 Detailed sketch of the rigid and segmented valve models (sizes in mm)

The rigid valve is constructed from two slices of polystyrene attached to a silicon rubber sheet (see figure 3.4). The part of the sheet which sticks out on the back of the valve is used to fix the valve to the aorta wall. The fixation angle is 0.785 rad (45°). In one of the slices a cavity is machined out in order to make the resultant density of the valve less than that of water. The density of the valve is about 95% of that of the fluid. The tip of the valve is sharp (tip angle is 30°) in order to assure that the flow always separates at the tip. The length of the valve is 27.7 mm,the thickness is 2.1 mm and the width is 119.2 mm, leaving a slit of 0.4 mm between the valve and the front and rear channel walls. The force transducer rod can be fixed to the valve by a hinge at a distance l_f = 12.7 mm from the edge where the valve is connected to the wall. The transducer fixation point is 10 mm from the symmetry plane of the aorta model in order to minimize the flow disturbances in the central part of the flow channel. The relationship between the measured force f and the moment m is given by

$$m = f\, l_f \cos \varphi.$$

The segmented valve is constructed from four slices of polyethylene, fixed on the top side of a silicon rubber sheet, as shown in figure 3.4. The length of each slice is 7.0 mm, the total length of the valve is 30 mm. The thickness is 1 mm and the width is 119.0 mm. The density of the polyethylene is about 0.94 kg/m^3. On every segment two markers of retro-reflective material are placed. The segments are trapezoidal in order to prohibit contact between the segments when the valve is moving. The tip angles are 45°. The valve is fixed to the aorta wall at an angle of 0.392 rad (22.5°).

Apart from the more elaborated experiments with the rigid and segmented valves, an indicative experiment is performed with a flexible valve consisting of a very thin (3μm) polyethylene sheet (110 x 30 mm^2).

3.2 Flow characterization

The inlet flow is characterized by the Reynolds number Re, the Strouhal number St and the shape of the flow rate curve as a function of time. Re and St are defined as

$$Re = \frac{u_c h_c}{\nu} \qquad (3.1)$$

$$St = \frac{h_c}{u_c \tau} \qquad (3.2)$$

with h_c the channel height (20 mm) and ν the kinematic viscosity. For water, ν equals approximately 10^{-6} m^2/s. The temperature dependency of ν is taken into account. As characteristic velocity u_c is chosen the mean velocity, averaged over the channel height, at the moment of maximum flow rate. A typical value for u_c is 15 mm/s, which corresponds to Re = 300. This value of Re is chosen, in spite of the fact that it is much lower than the physiological value (4500), since it can be handled numerically. Both steady and unsteady flow will be used. In case of an unsteady flow rate, it will be pulsatile as shown in figure 3.5. This flow rate is determined by

Definition of a pulsatile flow

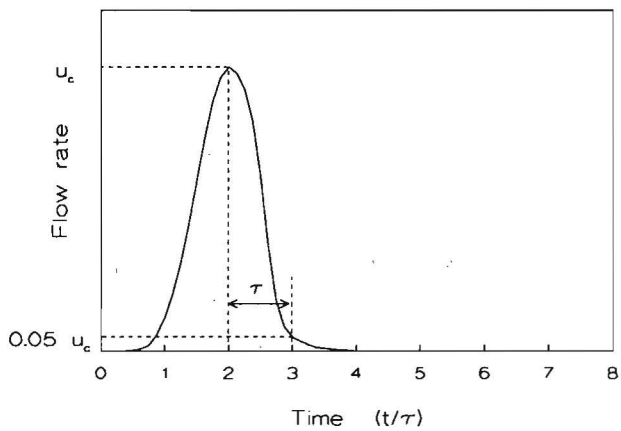

figure 3.5 Definition of the pulsatile inlet flow rate as a function of time, used both for experiments and numerical computations

measuring the axial fluid velocity in the symmetry plane at the inlet and integrating it over the channel height. Since the flow rate deceleration time is an important parameter in the valve closure mechanism (van Steenhoven,1979), this time is chosen as the characteristic time τ. It is defined as the time interval between the moment the flow rate reaches its maximum and the moment it has decreased to 5% of its maximum value (see figure 3.5). The length of the period is 10τ. The moment of maximum flow rate is defined to be at 2τ. In this study τ =1.8s, corresponding to St = 0.69 at Re = 300. Lower values of τ could not be achieved due to irregularities of the speed of the motor valve at low rotation frequencies.

3.3 Measurement equipment

The local fluid velocity is measured with a standard one-channel laser Doppler anemometer system (Dantec), consisting of optics, a Bragg-cell to provide a frequency shift and a frequency tracker. The size of the measuring volume is 0.2 mm in the direction perpendicular to the model and 0.06 mm in the other directions (0.3% of the channel height). In steady flow cases, the mean velocity is determined over an interval of 10 to 100 seconds. If the flow is pulsatile, averaging takes place over 5 flow periods. The resulting accuracy (defined as the 95% confidence interval) of the velocity is $5 \cdot 10^{-4}$ m/s^2 (3% of the characteristic velocity at Re = 300).

The force transducer is a linear variable differential transformer (T&S FT5A) with a range of ± 0.05 N. The maximum error is $5 \cdot 10^{-4}$N and the frequency band width is 0-50 Hz. The maximum displacement is 0.1 mm (0.5% of the channel height). If the valve is held in a fixed position and if the pinhole is removed, the force transducer does not show a measurable hysteresis. If the pinhole is present, a hysteresis of $2 \cdot 10^{-4}$N is observed, which is less than the maximum error of the transducer. It is probably caused by a slight friction in the pinhole. The resulting accuracy for the moment is $6 \cdot 10^{-6}$ Nm. If the valve is moved from one position to another the hysteresis is $2 \cdot 10^{-4}$ N, independent of the fact whether a pinhole is present or not. It is plausible that this hysteresis is caused by friction in the hinge which connects the valve and the transducer rod (figure 3.4).

The velocity and force data are digitized and read by a micro-computer, which also provides the automatic positioning of the laser Doppler system by means of stepper motors.

The positions of the rigid and the flexible valves are measured by means of a standard video-system. In case of the rigid valve, the image is projected on a screen, on which the valve angle is measured manually. The accuracy is 0.4° or 0.007 radians, which is 1% of the valve angle in fully closed position. The position of the flexible valve is copied manually from a monitor.

In case of the segmented valve, the segment positions are measured with a digital marker tracking system which is capable to track real-time the motion of a set of reflective markers. The system consists of a Hamamatsu C1181 random access camera and a Hentschel 84.330 video-tracking system. In contrast to a conventional camera, in which repeatedly the full image is scanned, the random access camera is capable to address directly only specific, relevant parts of the image. Here, these relevant parts are reflective markers on the valve. Since only a small part of the image is scanned, a high scanning frequency can be obtained. The random access

mechanism of the camera is controlled by the tracking system. First, an initial scanning of the full image is performed, in order to locate the start position of the markers. Around each marker a scanning window is defined. During the remainder of the measurement, in which the markers are allowed to move, only these scanning windows are addressed. After each scanning the marker positions are recomputed and the scanning windows are moved in such a way that the center of the marker is placed in the center of the new window. So, at each point in time the image coordinates of the window coincide with the marker position. These image coordinates are collected real-time by a micro-computer. Afterwards, the image coordinates are transformed to the laboratory coordinates. The required transformation is obtained by measuring the image coordinates of three calibration markers which are placed on positions in the model whose laboratory coordinates are well-known. By this strategy errors due to parallax and refraction are compensated also.

In this study, two markers per segment and four calibration markers are used, which leads to a total of 12 markers. The scanning frequency is 137 Hz (which may be higher if less markers are used). The size of the measurement area is approximately 120x120 mm^2. The resolution within each window is 256 x 256 $pixels^2$. The size of a window is 2 % of the measurement area or 2.4 x 2.4 mm^2. So, the theoretical resolution is ±0.01 mm which still can be improved by averaging over a number of samples. In practice however, the accuracy is less due to noise and transformation errors. By comparing the measured positions of well defined markers with their actual positions, the real error appears to be ±0.15 mm (95% confidence interval). This is less accurate than theoretically obtainable. It is expected that the accuracy can be improved by the application of a more advanced calibration and transformation strategy, using more calibration markers as applied by Peters (1987). The resulting accuracy for the segment orientation angle is ±0.04 rad (2^o).

3.4 Test of experimental model

In the theoretical models, it is assumed that the flow is two-dimensional. By making the width of the model six times larger than its height, an attempt is made to achieve a flow which is, at least in a major part of the model, two-dimensional as well. This is verified by measuring velocity profiles of the axial component along lines, parallel to z-axis (perpendicular to the symmetry plane of the experimental model) for the case of a steady flow around a fixed, rigid valve. The results are shown in figures 3.6 and 3.7.

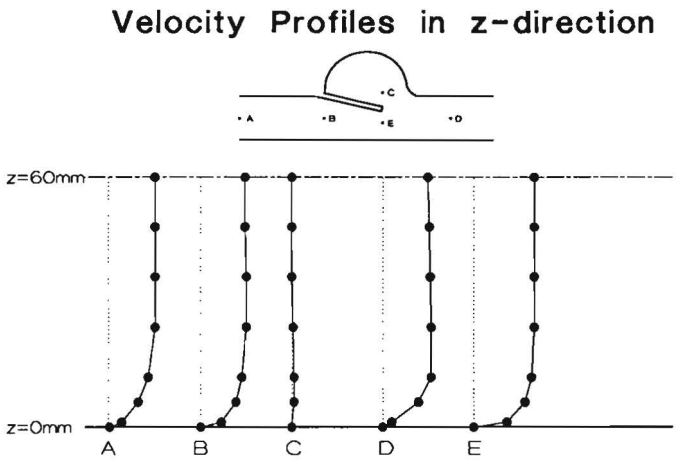

figure 3.6 Variation of the axial velocity along lines perpendicular to the symmetry plane of the experimental model. z=60mm corresponds to the symmetry plane. (Re = 100, φ =12.3^{o})

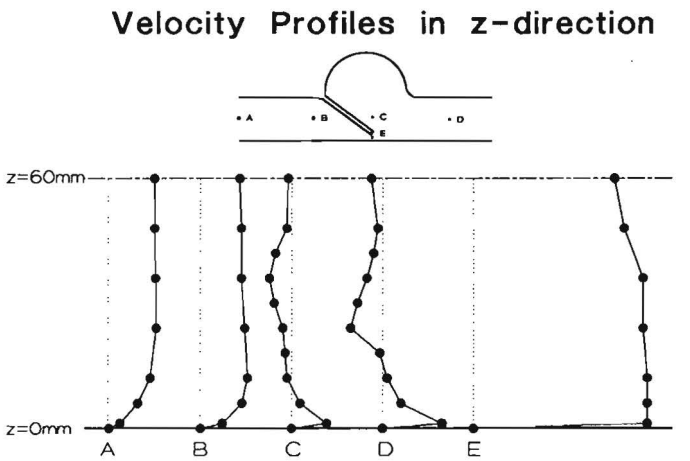

figure 3.7 Variation of the axial velocity along lines perpendicular to the symmetry plane of the experimental model. z=60mm corresponds to the symmetry plane. (Re = 100, φ =35^{o})

Figure 3.6 shows that when the valve is moderately closed ($\varphi = 12.3^{\circ}$), the flow is in a good approximation two-dimensional, apart from the boundary layer. The boundary layer occupies about 15% of the flow channel. If the valve is further closed, this approximation does not hold anymore. Figure 3.7 shows the situation in which $\varphi = 35^{\circ}$ and the valve opening is reduced to 2.5 mm. This opening is of the same order as the total width of the slits between valve and the front and rear channel walls (1mm). Especially in the sinus and behind the valve, large disturbances of the two-dimensionality are observed. Upstream the valve, the profiles are comparable to the moderately closed case: a flat velocity profile, apart from the boundary layer. Below the valve, the velocity is high and the boundary layer is very thin. Above and behind the valve, the velocity profiles are highly irregular: high velocities occur close to the wall and in the center of the channel the flow is reversed. Flow visualization with ink injection showed that in this situation a large double helical vortex is present behind the valve (figure 3.8). Therefore, the flow in the experimental model around a far closed valve cannot be regarded as being two-dimensional. The validation of the theoretical models is restricted to cases with a moderate valve closure.

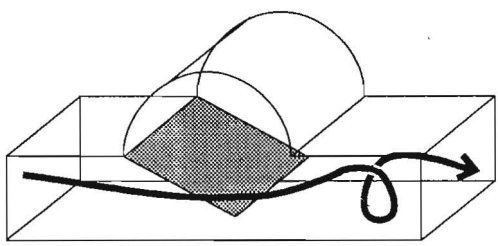

figure 3.8 Sketch of the three-dimensional fluid flow phenomena in the experimental model

3.5 Parameter estimation

In equations (2.28) and (2.29) the valve parameters γ_i, l_{gi} and β_{0i}, ..., β_{pi} are defined. γ is the effective weight per length, l_{gi} is the position of the center of mass and β_{0i}, ..., β_{pi} are the bending parameters. Estimates and/or assumptions for the parameters of the experimental valves are required as input data for the numerical models.

An obvious assumption would be to set β_{0i} equal to zero, since in general there will be no bending moment if $\varphi_i = \varphi_{i-1}$. Furthermore, since the segments are symmetrical in a good approximation, the position of the center of mass could be assumed to be in the middle of a segment so $l_{gi} = l_i/2$, with l_i the length of the segment. For the segmented valve these assumptions will be made indeed. However, since the rigid valve is slightly asymmetric and hollow, the assumption $l_g = l/2$ does not hold for this type of valve. Furthermore, since the density of the valve is very close to that of water, the density difference is difficult to measure accurately. Several attempts were made to determine γ and l_g experimentally or to compute them from the valve dimensions, but the desired accuracy was not obtained. Therefore, an alternative approach is chosen. The effects of buoyancy and bending are combined in one intrinsic valve moment m_b according to (2.29) with $\beta_0 \neq 0$. There is no distinction made between the individual contributions of buoyancy and bending. This strategy does not allow computing the buoyancy *force* which is needed in (2.33) to eliminate the hinge forces, but, since there is in this case only one segment present, elimination is not required, so this does not matter.

The model parameters are determined by measuring the valve moment as a function of position in the situation that no fluid flow is present. The results of the measurements are shown in figure 3.9. Some hysteresis is present, which is larger than the accuracy limit, but significantly smaller than the range of the valve moment itself. It is caused by friction in the hinge where the force transducer rod is fixed on the valve. (This type of friction must not be confused with the, much smaller, friction at the diaphragm.) A linear least square curve fit is applied to determine the valve parameters. A second order polynom with parameters β_0, β_1 and β_2 appears to yield sufficient accuracy.

As mentioned before, for a segmented valve β_{0i} is set to zero and it is assumed that $l_{gi} = l_i/2$. The determination of the other parameters γ_i and β_{0i}, ..., β_{pi} is more complicated than in the rigid valve case. Since even in the latter relatively simple case both a direct experimental determination and a computation from the valve geometry did not yield a sufficient accuracy, no attempt has been made to repeat this for the more complicated segmented valve. After some trial and error, the

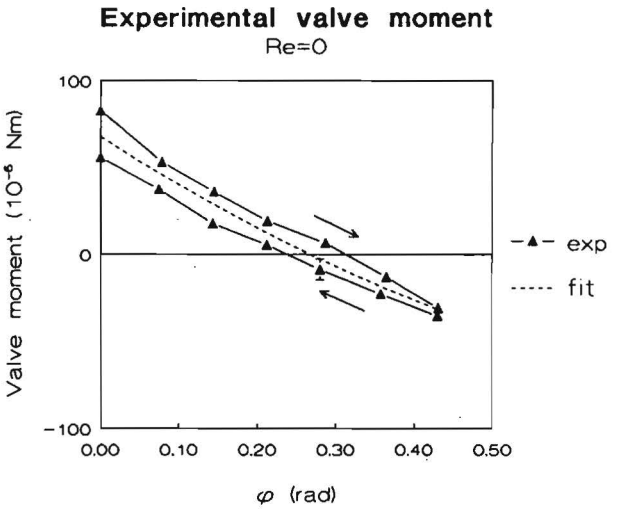

figure 3.9 Experimental valve moment at Re = 0 as a function of position. The dashed line denotes the applied linear least square fit, used to quantify the valve parameters

following method has been used. Various well-known external loads are applied to various locations on the valve. These loads may be either small brass weights placed on top of the valve or small pieces of cork, mounted on the bottom side. The weight of the messing and cork weights is determined separately with a balance. The accuracy is ±0.03 N. By varying the loads and the location on the valve, the valve is deformed in ways, which resemble the valve deformation due to the fluid flow. Totally, 21 situations as shown in figure 3.10a are considered. The deformations are measured by using the marker-tracking system described earlier. The loads and deformations are substituted in the valve equilibrium equations (2.27), (2.28) and (2.29), which yields estimations for the valve parameters. The fact that the center of mass of the applied weights does not coincide with that of the valve segments is taken into account. A nonlinear least squares method (Gill & Murray, 1978, implemented in the NAG-library) is applied in order to find the optimal set of valve parameters. In order to eliminate spurious effects due to temperature fluctuations and changes in the material behavior, the valve parameters have always been determined just before carrying out the fluid-structure interaction experiments. A set of eight parameters γ_i and β_{1i} (i=1,4) appears to be the optimal choice. If fewer parameters are used by choosing γ or β_1 to be equal for all or some segments, insufficient accuracy is achieved, whereas a second order approach as in the rigid

valve case does not essentially improve the accuracy.

In chapter 5 it will appear that the actual deformations in the fluid-structure experiments cover only a subrange of the ones shown in figure 3.10a: a modest valve closure and a concave valve shape. It might be expected that a set of parameters obtained from a reduced set of deformations, only covering this subrange, will yield a better agreement between experimental and numerical results. Therefore, the valve parameters are also determined from the reduced set of six deformations shown in figure 3.10b, which are in better agreement with the actually observed deformations.

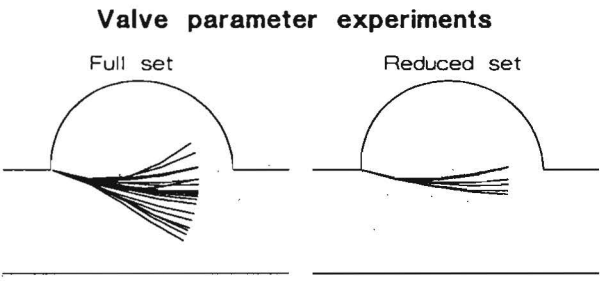

figure 3.10 Valve positions used for the experimental determination of the valve parameters (a) full set of positions (b) set of positions reduced to those positions, representative for those during the fluid-structure experiments

3.6 Error estimates

Errors in the determination of the valve parameters affect the accuracy of the computed valve equilibrium position. In this section, the influence of this experimental errors is analyzed.

Since the system equations are nonlinear, coupled and partly given in a recursive form, a straightforward error propagation can not be applied. The analysis method which is used in this study is illustrated by figure 3.11. The basic idea is the simulation of the parameter estimation and equilibrium search procedures starting from artificially simulated, and therefore well-known, reference cases. The resulting valve positions obtained from the combination of parameter estimation and equilibrium search are compared with the reference case, thus giving an estimate of the resulting error of the complete method.

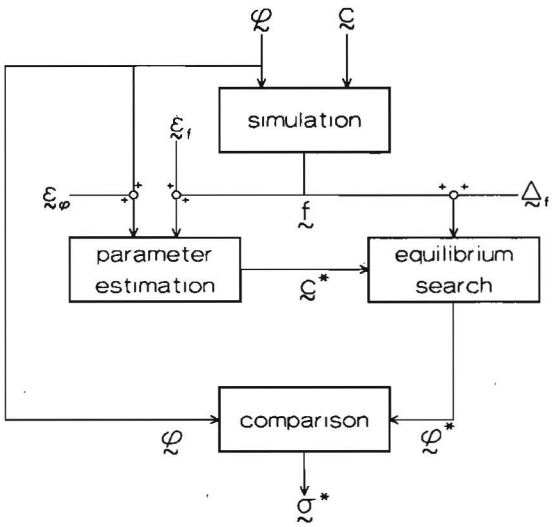

figure 3.11 Flow chart of the error estimation method

First, sets of valve parameters $\underset{\sim}{c}$ and valve positions φ are chosen. $\underset{\sim}{c}$ will be the set of experimentally determined parameters. For φ a representative selection of possible valve positions is chosen. For a rigid valve 20 equidistant positions between φ=0.0 and φ=0.4 are used and for the segmented valve the positions as shown in figures 3.10a and 3.10b. Substitution of these sets in the valve equilibrium equation yields the external forces $\underset{\sim}{f}$, needed to assure the equilibrium of the valve. As in the real experimental case, the valve parameters $\underset{\sim}{c}^*$ are estimated from the valve positions φ and the corresponding applied external forces $\underset{\sim}{f}$ by means of an optimization method. To both φ and $\underset{\sim}{f}$ random normally distributed noises $\underset{\sim}{\varepsilon}_\varphi$ and $\underset{\sim}{\varepsilon}_f$ are added, simulating the effect of stochastic experimental errors. The standard deviation of the noise is chosen equal to the half of the experimental error, thus defining the experimental error as the 95% confidence interval. With the estimated parameter set $\underset{\sim}{c}^*$ and the external forces a new set of equilibrium positions φ^* can be computed. In this computation the external forces $\underset{\sim}{f}$ are the equivalent of the fluid forces. To these external forces a relative systematic error Δ_f can be added, representing the effect of numerical errors in the computation of the fluid moment due the discretization. Finally, the computed equilibrium positions are compared with the original reference positions. If experimental errors are considered, an estimate for the standard deviation σ^* of the computed valve position is given by

$$\sigma^{*2} = \sum_i (\varphi_i - \varphi_i^*)^2/n \qquad (3.3)$$

with n the number of positions. The reliability interval for the computed equilibrium position is defined as twice this standard deviation. The systematic error of the valve position is defined as the difference between reference and computed position if only systematic errors in the fluid moment are considered.

ε_φ	ε_f	Δ_{fm}	Δ_φ
0	0	0	$\pm 2.10^{-6}$
0.007	0	0	±0.001
0	5	0	±0.005
0.007	5	0	±0.006
0	0	-0.2	+0.002
0	0	4	-0.01
0	0	9	-0.02
rad	10^{-4}N	%	rad

table 3.1 Effect of various errors on the accuracy of the numerically computed position of a rigid valve. ε_φ and ε_f: experimental stochastic errors in the measurement of the valve position and valve force (both are required for the determination of the valve parameters), Δ_{fm}: systematic numerical error in the computation of the fluid moment, Δ_φ: error in the computed valve position

Table 3.1 summarizes the results of the error estimation for the rigid valve. If $\underset{\sim}{\varepsilon}_\varphi$, $\underset{\sim}{\varepsilon}_f$ and Δ_f are all set to zero, the error is about $\pm 2 \cdot 10^{-6}$ rad due to the truncation error of the equilibrium search. If also the experimental errors $\underset{\sim}{\varepsilon}_\varphi$ and $\underset{\sim}{\varepsilon}_f$ are considered, the accuracy of the equilibrium position becomes ±0.006 rad (0.3^o), which is in the same order as the experimental error. The error of the external forces gives the major contribution. The systematic numerical errors of the fluid moment have a somewhat larger impact on the valve position. If the relative error Δ_f is +4% (which corresponds to the Re=300 case in section 2.4.1) the error of the valve position is -0.01 rad, which increases to -0.02 rad if Δ_f = +9% (Re=500 in section

2.4.1). For Re ≤ 300 the resulting accuracy is acceptable. The results for higher values of the Reynolds number are considered to have mainly an indicative value.

Figure 3.12 shows the dependence of the resulting error on the angle measurement error. For a rigid valve (1 segment), the increase of the resulting error is approximately linear. The contribution of the measurement error to the resulting error is negligible indeed. For the segmented valve however, the angle measurement error is crucial. The resulting error increases very fast with the angle measurement error. Furthermore, the angle measurement error is six times larger than in the rigid valve case. For an angle measurement error of 0.04 rad, the resulting error is approximately 0.16 rad (9^o), which is rather large. The extreme sensitivity of the resulting error is probably due to the fact that an error in one segment directly affects the force and moment balances of the others. From figure 3.12 it is clear that if the angle measurement error would be reduced with a factor two or three (which is felt to be possible by improving the calibration and transformation procedure), the magnitude of the resulting error would be acceptable. The errors in the external load and in the lever length appear to have a small or negligible influence on the resulting error (0.02 rad due to the load error and 10^{-4} rad due to the lever length error).

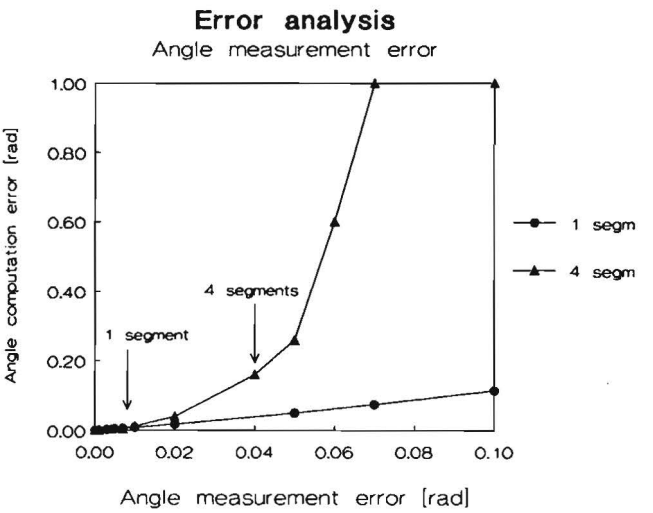

figure 3.12 Resulting error in the computed valve equilibrium position due to experimental errors in the position measurement during the parameter estimation experiments

4. RIGID VALVE

The models of chapter 2 are first applied to a rigid valve. The results will be given in this chapter. They will be validated by a comparison with experimental results, obtained by the methods described in chapter 3. Before presenting the results of a freely moving valve in sections 4.3 and 4.4, the theoretical fluid models and the experimental methods are tested in a situation in which the valve is held in a fixed position. In this case the interaction model is not yet applied.

4.1 Fixed valve in a steady flow

An essential part of the interaction model is the moment exerted by the fluid on the valve. The computation of this fluid moment is tested independently from the total interaction model by keeping the valve in a fixed position. The fluid moment is computed and compared with the results obtained from the different analytical models and with experimental data. In this section steady flow situations are considered. In the next, the flow rate will be pulsatile. Unlike the analytical models, the finite element fluid model also gives, apart from the fluid moment, detailed information on the total velocity field around the valve. The computed velocity field will be compared with the results of laser-Doppler measurements.

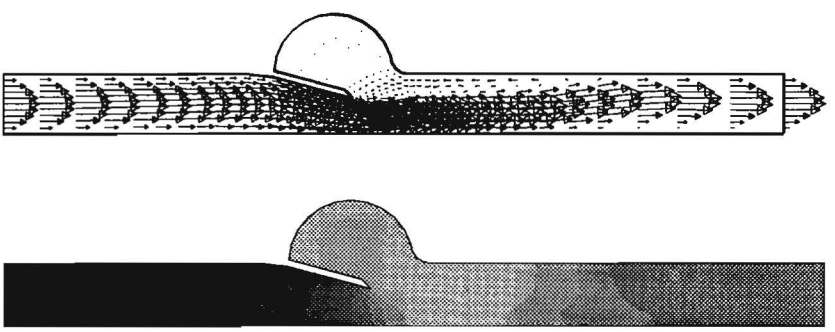

figure 4.1 Velocity and pressure fields around a fixed valve in a steady flow (Re = 400, φ =15^{o})

Figure 4.1 gives a typical example of the velocity field and the pressure distribution for a moderately closed valve (valve angle 15^{0}). The flow separates at the valve tip, forming a wake and a vortex behind it. The flow reattaches at a distance of about the sinus diameter. The pressure in the sinus is low and approximately equal to the pressure at the valve tip. These observations correspond

with the assumptions, made for the quasi one-dimensional analytical fluid model in section 2.1.1. Because of the flow reattachment, the assumption of a horizontal streamline far behind the valve in the von Mises model is not completely satisfied. This reattachment is at least partly caused by a viscous diffusion of the jet-like flow right behind the valve. Since in the von Mises model no viscous effects are present (apart from the flow condition at the valve tip), this model ignores this type of diffusion.

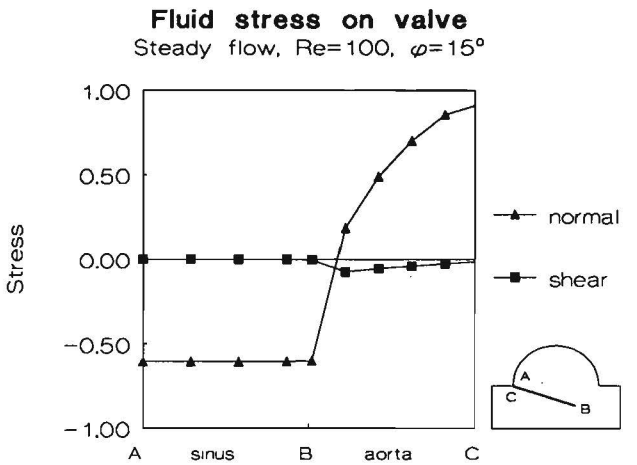

figure 4.2 Numerical normal and shear stresses along a fixed valve due to a steady flow (Re = 100, $\varphi = 15^{o}$)

The pressure distribution obtained from the finite element model is shown in more detail in figure 4.2. At the sinus side of the valve the pressure is constant. At the aortic side, the pressure is high near the fixation point and drops nearly quadratically in the direction of the tip. The shear stresses are much smaller than the pressure. Since also the lever length of the shear stress is small (approximately the thickness of the valve), the contribution of these stresses to the total fluid moment is in this case of minor importance. The numerical computations are performed for two different element meshes, shown in figure 4.3. In order to compare these computations with experimental data, in figure 4.4 velocity profiles of the axial component are given on several locations. The differences between the results of both meshes are smaller than 1% and are too small to be visible in the figure. In a good approximation, the shape of the velocity profiles remains parabolic until it reaches the valve tip. The velocity in the sinus is approximately zero. Behind the

valve, some reversed flow is present, indicating the existence of a weak vortex. Apart from the wake, the agreement with the experimental results is close. In the wake, a slight difference occurs. A close examination shows that in the numerical case, the vortex is somewhat closer to the valve than is observed experimentally.

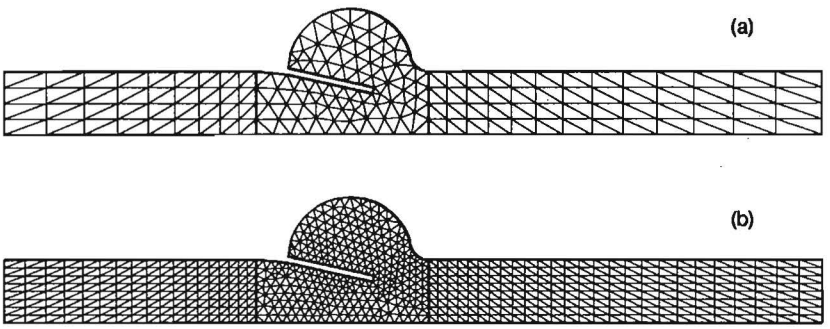

figure 4.3 Finite element meshes, used for the computation of the velocity profiles in figure 4.4 (a) 327 elements, 1139 unknowns (b) 1266 elements, 4729 unknowns

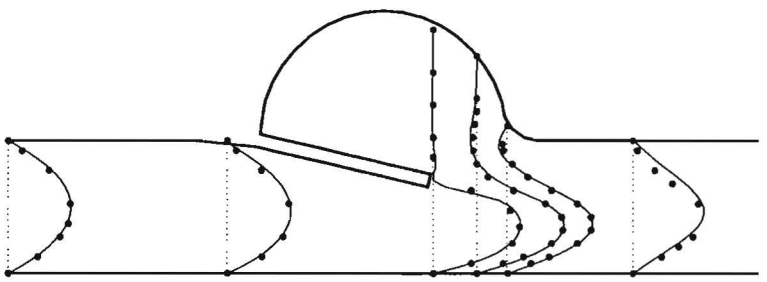

figure 4.4 Experimental (•) and numerical (-) profiles of axial velocity for both standard and fine mesh (φ = 12.4°, Re = 100)

Figure 4.6 shows that this discrepancy increases when the valve is further closed. Now, some differences between the numerical results for the coarse and the fine mesh (figure 4.5) are present. The coarse mesh causes some oscillations at the valve tip and somewhat behind it, indicating that it is too coarse for this situation. These oscillations disappear when the mesh is refined. Also the global form of the velocity profiles is different for both meshes, but still the results for the fine mesh do not fully agree with the experimental ones. In chapter 3 it is shown that the flow in the experimental model is not two-dimensional if the valve is in this far closed position. Essentially three-dimensional flow phenomena occur in this case.

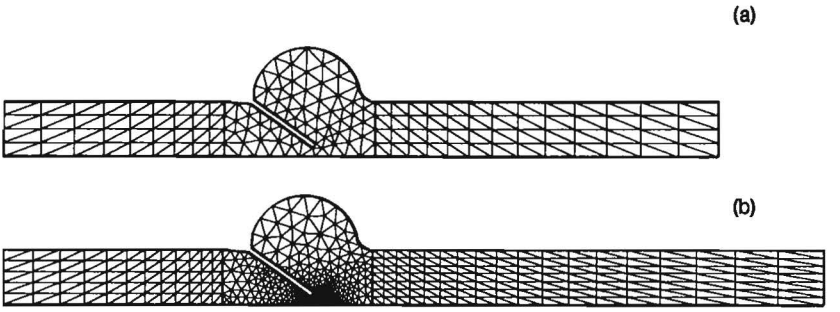

figure 4.5 Finite element meshes, as used for the computation of the velocity profiles of figure 4.6 (a) 310 elements, 1073 unknowns (b) 1270 elements, 4745 unknowns

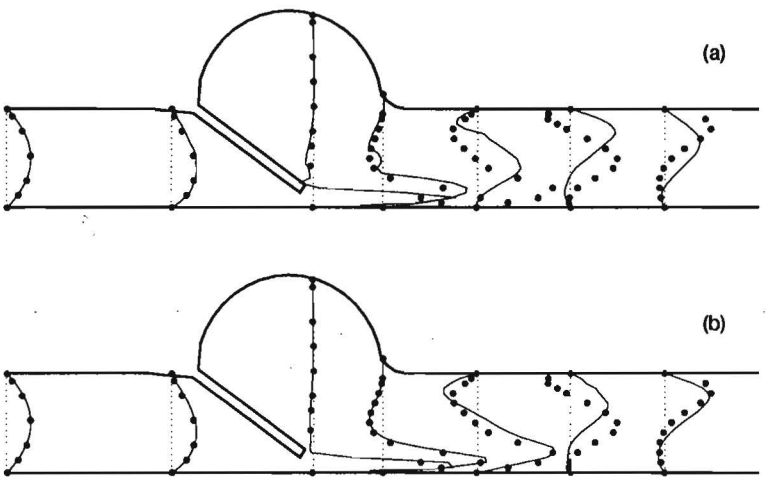

figure 4.6 Experimental and numerical profiles of axial velocity ($\varphi = 35^{o}$, Re = 100), (a) 310 elements, (b) 1270 elements (see figure 4.5)

Therefore, at least part of the deviations found will be caused by three-dimensional effects in the experiments.

The previous comparisons show that for moderately closed valves, both element meshes yield proper results. When the valve is far closed, the coarse mesh is not suitable. A finer mesh gives better results, but the computational effort will be too large, when used in combination with the fluid-structure interaction algorithm. Also the experimental data are not reliable in this situation. For these reasons, in the remainder of this study, the valve positions will be restricted to moderate angles (up

to approximately 20^0).

The moment exerted by the fluid on the valve as a function of the Reynolds number is shown in figure 4.7. Experimental, analytical and numerical results are given. The analytical fluid moments increase essentially quadratic if the Reynolds number (or better: the flow rate) increases. This follows directly from Bernoulli's theorem. Also the experimental and numerical results increase quadratically in a good approximation, thus showing that the viscous phenomena within the fluid have only a slight effect (apart from the flow separation on the valve tip), since the moment would increase only linearly with the flow rate if viscous phenomena were dominating the flow field. The tendency of all theoretical results agrees well with the experimental ones. As might be expected, the agreement improves when the model becomes more sophisticated.

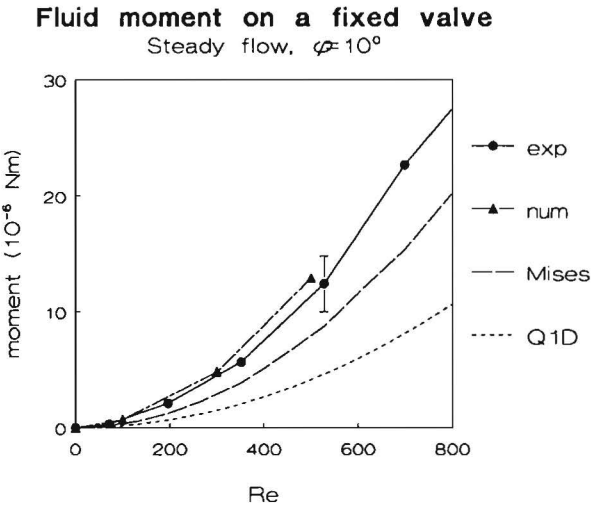

figure 4.7 Experimental, analytical and numerical fluid moments, acting on a valve in a fixed position (φ=10°) due to a steady flow, as a function of the Reynolds number

The qualitative agreement for the quasi one-dimensional model is good, suggesting that the most important physical phenomena are incorporated in it. However, since the relative deviations from the experimental results can raise to almost 300%, the model is too rough to give precise results. The fact that the inlet velocity profile is flat (in contrast to the fully developed parabolic one in the experimental case) is not responsible for the observed deviation. In appendix F it is estimated that a parabolic profile decreases the pressure gradient over the valve

slightly (approximately 14%). For the von Mises model, the relative differences are about 25%. This shows that a large improvement is obtained when two-dimensional flow phenomena are incorporated. The remaining deviation is caused by the ignorance of the viscous phenomena and the convection due to vortex formation and flow reattachment. For the finite element model, the agreement is close. The model predicts a somewhat larger fluid moment, but the deviations fall within the experimental accuracy limit. On the other hand, in chapter 3 it has been observed that the fluid flow in the experimental model is in a good approximation two-dimensional (for these moderate valve angles), apart from the boundary layers at the front and rear channel walls, which occupy about 16% of the valve width. At Re=500, the experimental fluid moment is about 14% less than predicted numerically. Therefore, it is likely that the (small) deviation can be explained partly from this imperfectness of the experimental model. With the applied standard element mesh the maximum Reynolds number for which the fluid solver converged was about 500.

4.2 Fixed valve in a pulsatile flow

If the fixed valve is exposed to a pulsatile flow, the fluid moment on it will be time dependent. The flow rate as a function of time is shown in figure 4.9. The velocity field and pressure distribution on certain time levels are shown in figure 4.8. At t = 0.0, the flow rate is zero and velocities are small. A very weak vortex behind the valve is present, persisting from the previous period. At t=1.0, the fluid starts accelerating. The vortex is swept away. At t=1.5 (about halfway the accelerating period), the velocity profiles are nearly flat. At t=2.0 (maximum flow rate) a new vortex is being formed behind the valve, which rapidly grows during flow deceleration (t=2.5). At t=3.0 the flow rate is almost zero again. Near the boundaries a region of small reversed flow is present. A strong vortex remains. Just downstream this vortex, a secondary vortex is being formed which has grown at t=4.0, when the main vortex is already decaying. Both vortices lose strength in the remainder of the flow cycle until t=10.0, when the situation is identical to that at t=0.0. In the numerical computations, the flow phenomena become already periodically at the start of the second period.

In figure 4.9 experimental, analytical and numerical data on the fluid moment as a function of time are given. All data show that the fluid moment is not only related to the flow rate itself but that it is more or less proportional to the time derivative of it. The moment is positive (in valve opening direction) when the flow

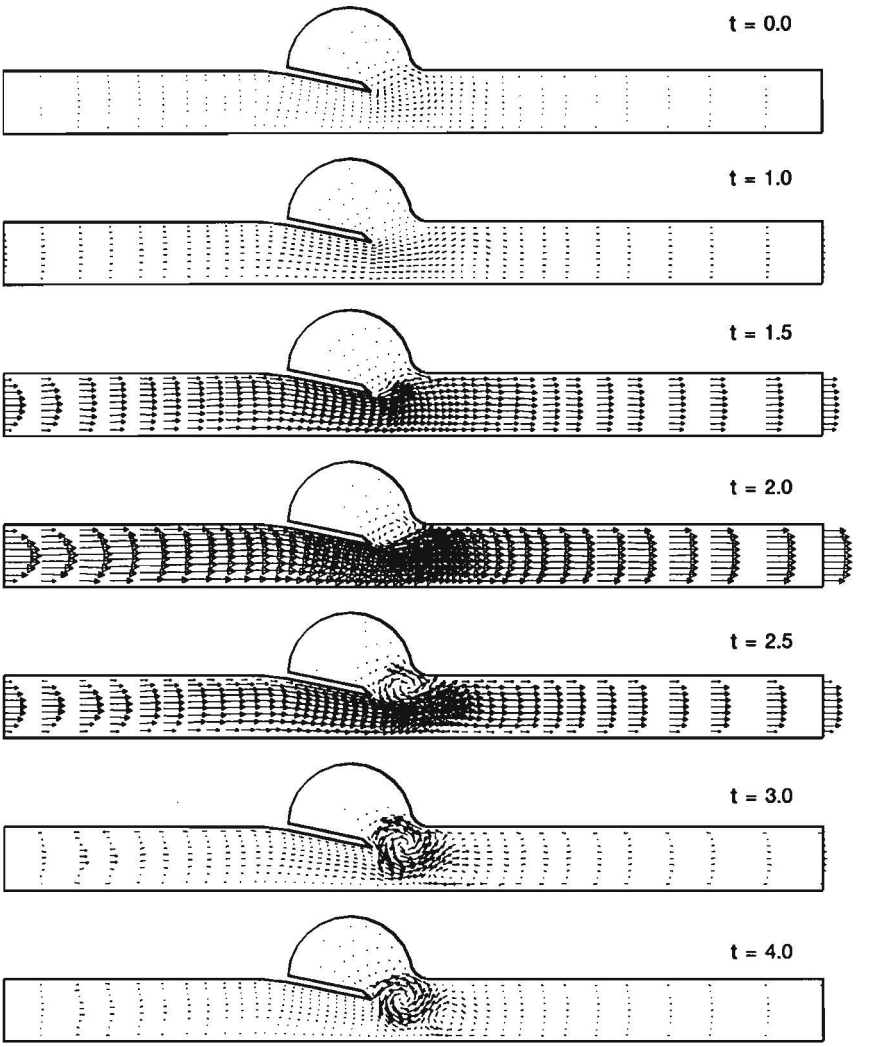

figure 4.8 Velocity field around a fixed valve at 12° in a pulsatile flow (Re = 313, St = 0.69) on several dimensionless time levels (maximum flow rate at t=2.0, pulse width = 1.0, see figure 4.9)

accelerates, approximately zero when it is constant and negative (towards the closed position) during flow deceleration. This follows directly from the unsteady Bernoulli equation (2.2). The fact that the deceleration of the flow generates a fluid moment which attempts to close the valve, causes the early state closure of the natural aortic valve (van Steenhoven and van Dongen, 1979). The zero crossing of the moments do not coincide exactly with the flow rate maximum, since a steady component is superimposed, which is approximately proportional to the square of the flow rate (see figure 4.7).

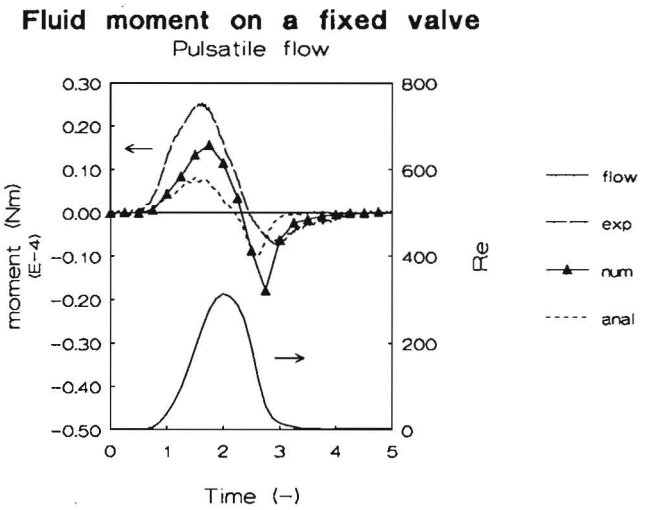

figure 4.9 Experimental, analytical and numerical fluid moments, acting on a valve in a fixed position (φ=10°) due to a pulsatile flow, as a function of time (Re_{max} = 313, St = 0.69)

The agreement between experimental and theoretical results is not as close as in the steady flow case. Apart from the amplitude, the numerical and analytical results agree fairly well. Both are more or less symmetrical around zero showing a sharper pulse during flow deceleration than during acceleration. This is caused by the asymmetry of the flow rate pulse, which drops somewhat faster than it rises. The zero crossings do not exactly coincide. The amplitudes differ about a factor 2, slightly less than in the steady flow case. The reasons for these deviations are similar to those discussed in the previous section. Figure 4.10 shows that the time integration step, the inlet length and the element mesh do not affect the numerical results essentially. The inlet length and mesh distribution hardly show any effect. Decreasing the time step shows that a small amount of numerical damping is present.

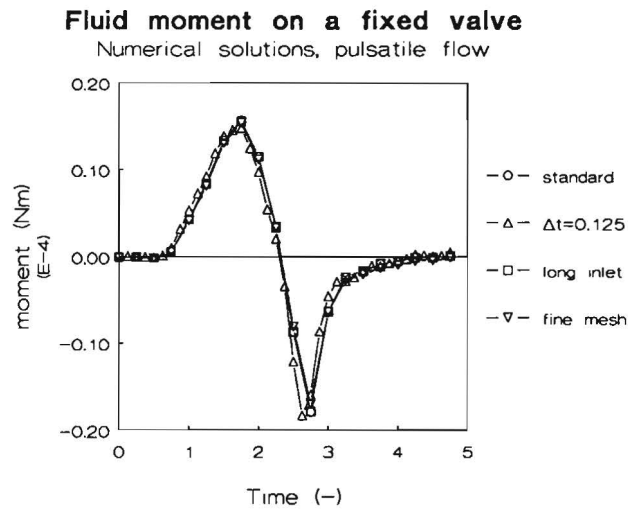

figure 4.10 **Comparison of numerical fluid moments on a valve in a fixed position in a pulsatile flow. The standard case is also shown in figure 4.9 and is computed using the standard mesh and inlet length and Δt=0.25.**

The experimental results are rather different. The amplitudes of numerical and experimental fluid moment agree fairly well, but the course of the experimental fluid moment is more asymmetrical and the zero crossing lags more behind the flow rate than the theoretical results do. It is plausible that the experimental results are disturbed by the boundary layer at the front and rear sides of the flow channel. In this boundary layer, the relative importance of the viscous effect, compared to inertial effects, are larger than in the main flow. Therefore, the pressure gradient in the boundary layer will be more in phase with the flow rate than it is in the remainder of the channel. The pressure gradient in both the main flow and the boundary layer contribute to the experimentally observed moment, so it will be more in phase than in the purely two-dimensional theoretical cases. The experimental course of the moment as a function of time can be thought as being a superposition of a part which is proportional to the flow rate curve and another part, proportional to its time derivative. This is observed indeed in figure 4.9. Experimentally, the moment is shifted in positive direction so the zero crossing alters and the negative peak decreases. An additional cause of this discrepancy is the fact that, although minimized by the presence of the diaphragm in the sinus, a small leakage of flow still exists in the sinus. Furthermore, it is possible that the rod connecting valve and

transducer is subjected to some friction at the diaphragm, causing an hysteresis effect.

4.3 Steady free valve

The previous sections of this chapter have dealt with a valve in a fixed position, when no full interaction of valve motion and fluid flow is present. In this section, the elementary but illustrative case is studied of a free valve which is in its equilibrium position in a steady flow. Since the valve is allowed to move freely, this equilibrium position is not known in advance and therefore the interaction model of section 2.3.1 is applied.

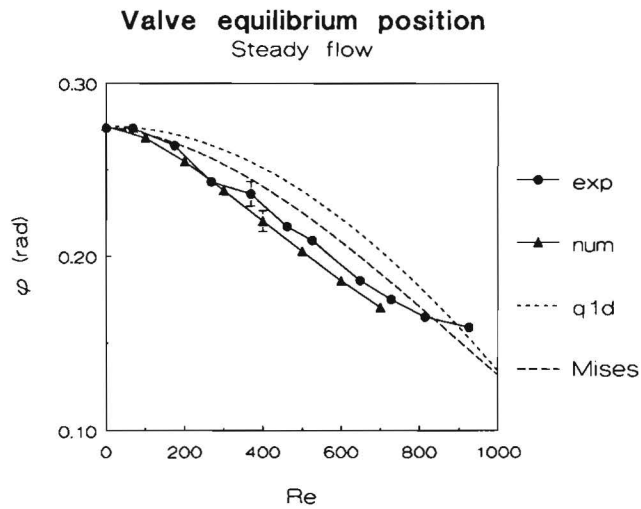

figure 4.11 Experimental, analytical and numerical valve equilibrium positions of a free valve in a steady flow as a function of the Reynolds number

The valve equilibrium position is computed as a function of the Reynolds number. The results are shown in figure 4.11. Since from figure 4.7 it is observed that the fluid moment increases when the Reynolds number increases, it is obvious that the valve will be more opened at higher Reynolds numbers. This is found indeed, both experimentally and theoretically. Also the global tendency of the theoretical valve positions resembles the experimental one. The analytical models predict less effect of the Reynolds number than is observed. This is consistent with the observation in section 4.1 that they underestimate the fluid moment. The finite

element fluid model gives fairly accurate results. The valve angles are somewhat smaller than the experimental ones because of the fact that the finite element model predicts a somewhat larger fluid moment (see figure 4.7), so the valve is pushed up a little more.

4.4 Moving free valve

In this section some transient cases are considered of a valve which is moving while interacting with a fluid. The interaction model of section 2.3.1 is used in combination with the full unsteady Navier-Stokes equation for the fluid. The analytical models of chapter 2 do not incorporate the motion of a valve, so they are not applied here.

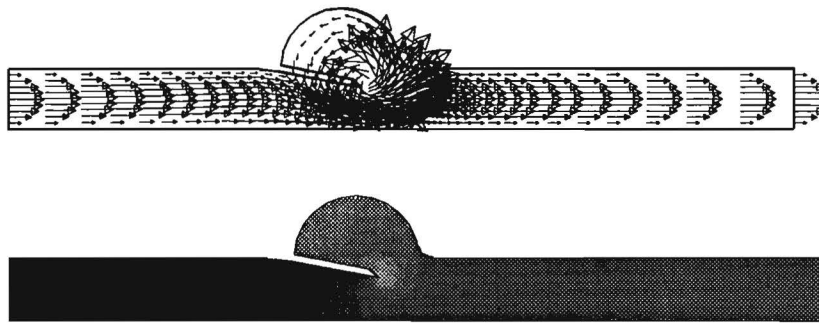

figure 4.12 Velocity and pressure fields around a free valve moving under constant flow rate conditions from fully opened position to its steady equilibrium position (Re = 130, St = 1, Δt=0.1, t=0.2)

The first case is that of a closing valve under a constant flow rate condition. The valve is fixed in fully opened position until t=0 and then released. The valve will move towards its equilibrium position. Figure 4.12 shows the fluid phenomena at a typical timestep. The valve velocity is large compared to the fluid entrance velocity. The contents of the sinus rotates together with the valve. This observation supports the negligence of the inertia of the valve, since it is much smaller than that of the fluid surrounding it. In figure 4.13 the position of the valve as a function of time is shown. After a short acceleration period, the valve moves downward with an approximately constant velocity until a maximum is reached and then it moves to its steady state equilibrium position in a damped oscillatory way. This behavior is found both experimentally and numerically. The numerical solution with the largest timestep shows considerable numerical damping, due to the Euler implicit time integration scheme: the solution lags behind the experimental motion and the extremes are

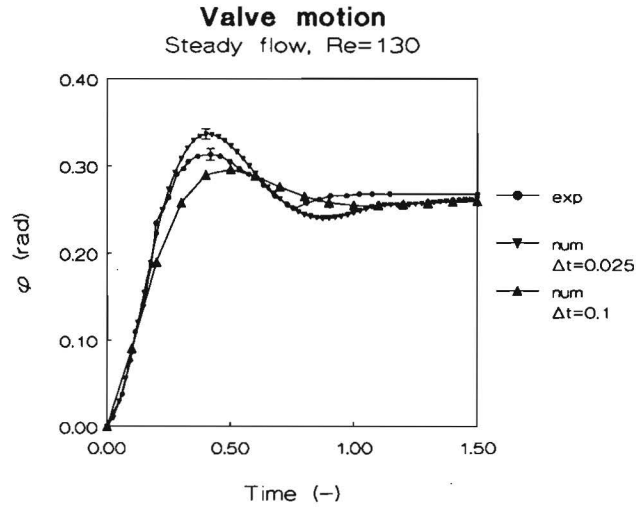

figure 4.13 **Experimental and numerical valve positions as a function of time for a valve which is held in fixed horizontal position until t=0 in a steady flow (Re=130) and then released**

smaller. The agreement between the numerical solution for a small time step and the experimental results is much better. In the first part of the motion, the agreement is very close. The maxima coincide in time, but experimentally it is somewhat smaller than it is predicted numerically. The minima at about t=0.8 do not coincide. The numerical minimum lags behind and is slightly larger; the experimental motion is damped out earlier. Magnitude and origin of the difference between the final equilibrium position are similar to that found for the steady state case (see figure 4.11). In principle, two possible explanations could be given for the differences between the experimental and numerical valve motions. Although for the small time step the numerical solution is much smaller than for the large time step, there will still be some numerical damping left. This might account partly for the lagging of the numerical minimum. However, it does not explain why the numerical extremes are larger than the experimental ones. Therefore, a more likely cause is that the fluid flow in the experimental model is not perfectly two-dimensional, as shown in figure 3.6. The motion of the valve will be affected by friction forces due to the boundary layers at the front and rear panel of the flow channel. This causes an extra damping of the valve motion, which is not accounted for in the numerical model.

4.5 Parameter variations

With the numerical model some more simulations are performed. Figure 4.14 shows the motion of the free valve due to a harmonically varying flow rate. The first period is a start-up effect, but after that the valve motion becomes harmonic. It is interesting to note that the valve moves already towards its closed position during flow deceleration, just like the natural aortic valve does. This observation is consistent with the results of section 4.2.

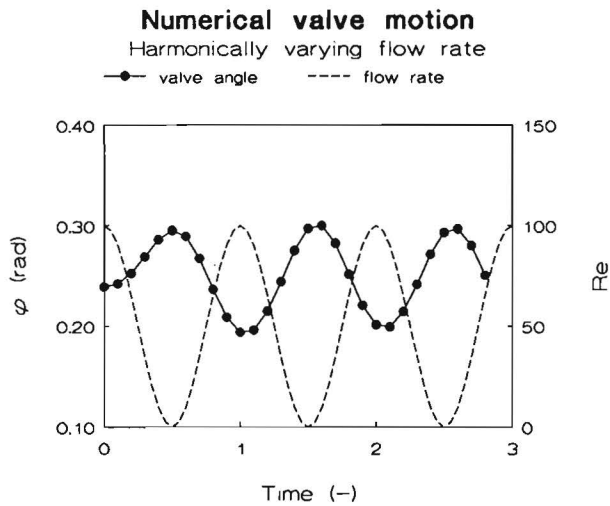

figure 4.14 Numerical simulation of the valve motion in the case of a harmonically varying flow rate (Re_{max} 100, St = 1)

Figure 4.15 shows the valve motion due to a pulsatile flow according to the experimental situation. The Reynolds and Strouhal numbers are kept equal to those in the fixed valve case. In figure 4.15 a parameter k is introduced by which the experimentally determined valve parameters are multiplied. k=1 corresponds to the original, experimental situation. k=0.1 and k=0.01 correspond to hypothetical valves for which both the buoyancy and the hinge bending are made smaller relative to the fluid moment. The steady equilibrium positions of these valves at Re=0 coincide with those for the k=1 case. At Re=0, the buoyancy force balances the hinge bending moment. So, they may be regarded as valves whose bending hinge is made more flexible and whose density is adapted in order to maintain the original equilibrium position. This enables a comparison between the different cases. The case k=0 is a fully free valve, which is not subject to any buoyancy and hinge bending. Such a

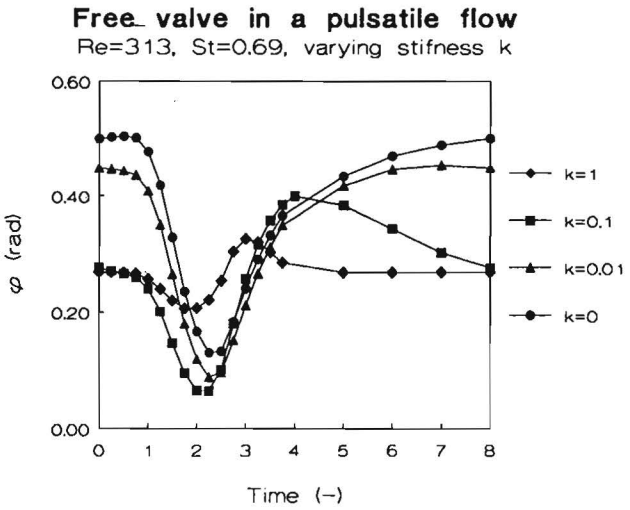

figure 4.15 Numerical simulation of the valve motion due to a pulsatile flow rate for various valve parameters. (Re_{max} = 313, St = 0.69)

valve has no well determined equilibrium position on its own. The motion and equilibrium are completely induced by the surrounding fluid flow.

It appears that for k=1 the valve amplitude is rather small. The position of the valve is in a good approximation in phase with the fluid moment on a fixed valve as shown in figure 4.9. Apparently, the displacements are too small to generate a significant contribution by the inertia of the surrounding fluid. The valve opens during flow acceleration, it tends to close in the deceleration phase and it remains in its equilibrium position if the flow rate is zero.

If the hinge is more flexible (k=0.1 and k=0.01) the valve amplitude increases and the motion is not in phase with the fluid moment as observed in the fixed valve case. This indicates an increasing inertial fluid effect. For k=0.1, the hinge moment is still large enough to force the valve into its equilibrium position, albeit just at the end of the flow period. If k is less than 0.1 the valve hinge becomes too weak to accomplish this. The extreme is the fully free valve (k=0) when the valve has a pseudo-equilibrium position at $\varphi \approx 0.55$. This corresponds to a valve closure of about 75%. The valve motion becomes periodical after about three flow cycles. Figure 4.16 shows the velocity field for this case. Globally, it resembles the flow field for the fixed valve case (figure 4.8). At t=0.0 the velocities are small. A vortex is present in the sinus. It is closer to the valve than in the fixed valve case. At t=1.0 the fluid is accelerated and the valve starts to open. At t=1.5 the valve has reached its

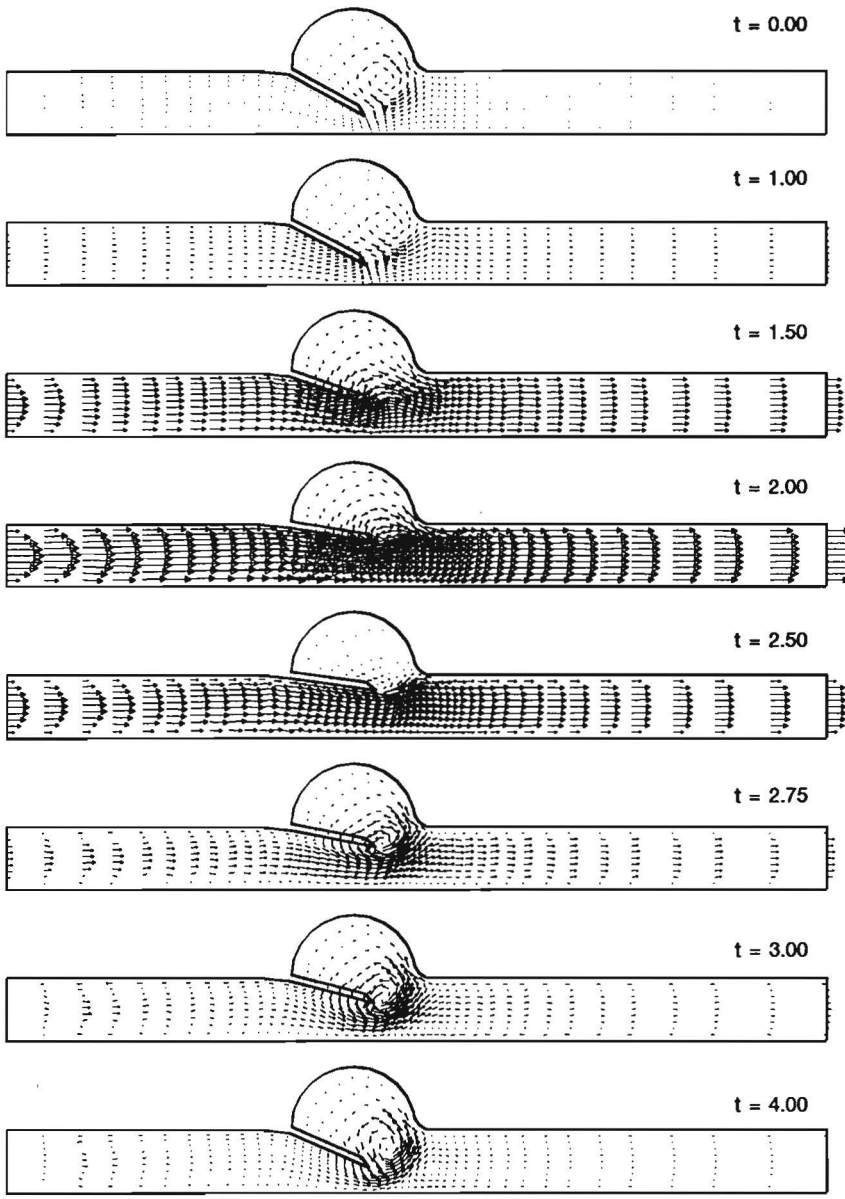

figure 4.16 Velocity field around a free valve in a pulsatile flow (Re = 313, St = 0.69, k=0) on several time levels

maximum velocity and pushes the contents of the sinus out. On t=2.0 the flow rate is maximal, the valve is slowing down but still moving towards the fully opened position. Just at t=2.5, when the flow has its maximum deceleration, the valve reaches its maximum position and its velocity becomes zero. At t=2.75 the valve is moving towards the closed position. A vortex in the sinus is being formed. At t=3.0, when the flow rate is nearly zero, the valve has its maximal closing velocity. At t=4.0 the valve has nearly reached its pseudo-equilibrium position and its velocity becomes zero.

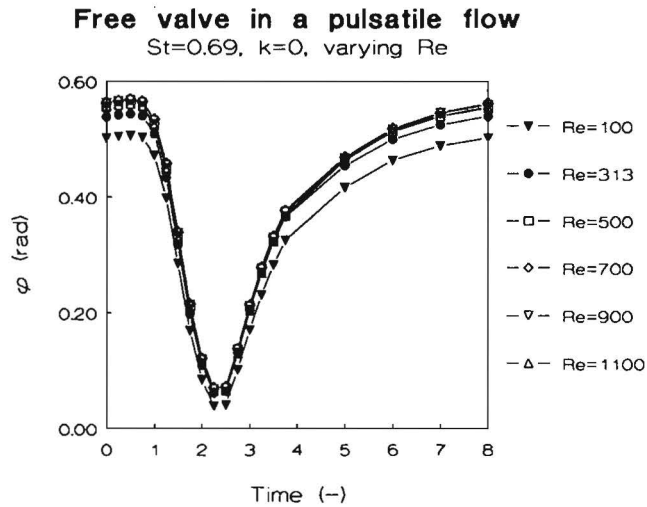

figure 4.17 Numerical simulation of the valve motion due to a pulsatile flow rate for various Reynolds numbers (k = 0, St = 0.69)

The simulations in figure 4.15 are performed for the experimental flow conditions (Re=313 and St=0.69). Figure 4.17 shows the effect of a variation of the Reynolds number for St=0.69 and k=0. It is clear that the effect is only marginal for Re=300-1100 for this rather large value of the Strouhal number. The fluid flow solver does not allow computations for Re>1100. The effect of the Strouhal number is larger, as is shown in figure 4.18. The physiological relevant case corresponds to St=0.06. The pseudo equilibrium position is in all cases around φ=0.55 rad (72% closure). For low Strouhal numbers the motion of the valve is nearly in phase with the flow rate and its amplitude is large. The maximum opened position is negative (further than horizontal) and coincides with the maximum flow rate. At the end of the systolic phase, the valve is nearly at its final diastolic position. This is consistent with the experimental and theoretical results from Bellhouse et al. (1969 & 1971), van Steenhoven & van Dongen (1979), Lu & Talbot (1979) and Wippermann (1985). No

full valve closure is observed here, since no back flow is present. The higher the Strouhal number, the smaller the valve amplitude and the more the valve motion becomes out of phase with the flow rate. At St=0.2 the moment of maximal opened position is halfway the deceleration phase and the valve does not reach his pseudo-equilibrium state before the end of the period. The fluid acceleration forces are proportional to the Strouhal number. This explains the phase change of the valve motion.

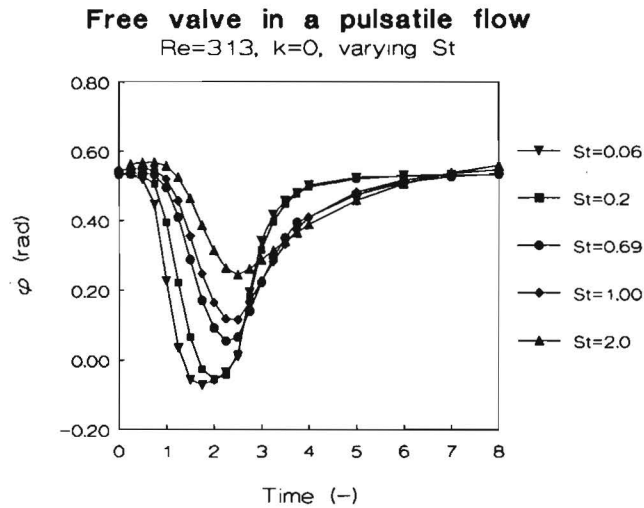

figure 4.18 Numerical simulation of the valve motion due to a pulsatile flow rate for various Strouhal numbers (k = 0, Re = 313)

In order to make a comparison with the work of van Steenhoven & van Dongen (1979) on the early valve closure, the case is studied of a linearly decreasing flow rate according to

$$\begin{aligned} u_o &= 1 && t \le 0 \\ u_o &= 1 - t && 0 < t < 1 \\ u_o &= 0 && t \ge 1 \end{aligned} \qquad (4.1)$$

Their experimental and analytical data are shown in figure 4.19. Their model is based on the same assumptions as the quasi one-dimensional model used in this study, but it also incorporates the motion of the valve. It is only valid at the onset of the valve closure, i.e. $\varphi << \pi/2$ or $|\lambda - 1| << 1$, with

$$\lambda = 1 - l \sin \varphi \qquad (4.2)$$

Because of the absence of viscosity, the theoretical Reynolds number is infinite. Their experiments are performed with a two-dimensional flexible leaflet valve at Re = 3100 and St = 0.06. This large value of the Reynolds number can not be handled by the finite element fluid model, so computations are performed at Re = 300 and Re =1000, as shown in figure 4.19. The numerical results share the main characteristic with those for the case with a pulsatile flow rate: at the end of the deceleration phase, the valve is far closed. In this case, the valve closure is about 50%. The dependence on the Reynolds number is somewhat larger than in the case with a pulsatile flow rate. The agreement with the experiments is fair, especially at the end of the deceleration phase. In the early phase the differences between experimental, analytical and numerical results are quite large. Numerically, the valve starts slowly and keeps moving slowly until the second half of the deceleration phase. The valve velocity in the initial phase for the analytical model is about three times as large. The experimental results are somewhere in between. The difference between the results of the numerical and the analytical model is caused by the presence of viscosity in the former one. This can be shown by considering the dimensionless Navier-Stokes equation (1.1). If the valve is fully opened, it can be simplified to the quasi one-dimensional form

$$St \frac{\partial u}{\partial t} + u \frac{\partial u}{\partial x} + \frac{\partial p}{\partial x} - \frac{1}{Re} \frac{\partial^2 u}{\partial y^2} = 0 \qquad (4.3)$$

The flow is linearly decelerating according to (4.1). If the fluid flow is assumed to be quasi-steady, the velocity profile is parabolic. This yields:

$$\frac{\partial u_o}{\partial t} = -1$$

$$u_o = 6y\,(1-y) \qquad (4.4)$$

so that for a fully opened valve the initial pressure difference p(l,0)-p(0,0) is:

$$\Delta p = l\,(St - \frac{12}{Re}) \qquad (4.5)$$

with l the length of the valve. For l = 1.385 St = 0.06 and Re = 300, Δp = 0.028,

while for $Re \rightarrow \infty$, $\Delta p = 0.083$. Therefore, in the numerical case the pressure gradient, which is the driving force for the valve closure, is approximately a factor 3 smaller at Re = 300 due to the viscous forces.

From (4.5) it follows that valve closure only occurs if $St > 12/Re$. Furthermore, it explains the difference in the dependence on the Reynolds number between the pulsating and the decelerating flow case. In the pulsatile flow case St=0.69 and $100 \leq Re \leq 1100$, so the pressure gradient varies between 0.79 and 0.94, which is a change of less than 20 %. In the decelerating flow case, St is much lower (0.06) so the pressure gradient varies from 0.03 at Re=300 to 0.07 at Re=1000 which is an increase of more than a factor 2.

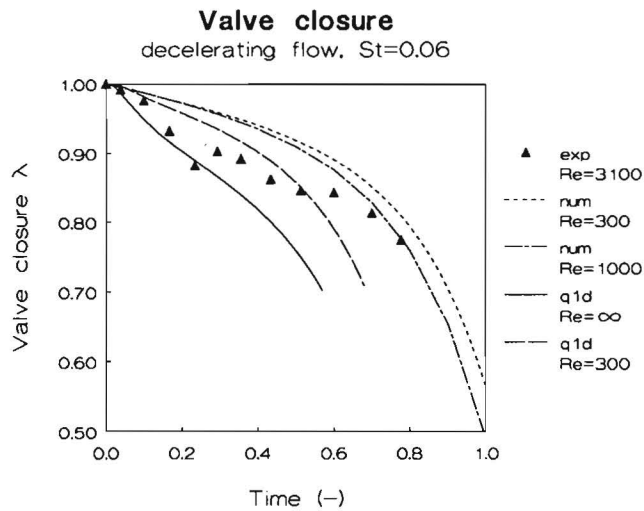

figure 4.19 Comparison of the experimental and analytical quasi one-dimensional results of van Steenhoven and van Dongen (1979) with numerical results and results of an extended quasi one-dimensional model for a rigid valve in a linearly decreasing flow rate, starting from the steady state (St=0.06, $\lambda = 1 - l \sin \varphi$

For a further analysis, the effect of the fluid viscosity can be incorporated in the model of van Steenhoven & van Dongen in a simplified way. Substitution of (4.4) in (4.3) and integration yields

$$p(x,t) = p_o + \tfrac{1}{2}u_o^2 - \tfrac{1}{2}u^2 - St\frac{\partial}{\partial t}\int_o^x u\,dx - \frac{12}{Re}x \qquad (4.6)$$

with p_o the pressure at the entrance plane of the valve. Again the valve closure parameter λ is introduced according to (4.2) and it is assumed that $|\lambda - 1| \ll 1$. The continuity equation is substituted in (4.6) and the mean pressure across the valve is assumed to be equal to zero, i.e.

$$\int_o^l [p(x,t) - p(l,t)]\, dx' = 0 \qquad (4.7)$$

The pressure in the sinus is taken equal to that at the valve tip. This leads to a differential equation for λ of the form

$$St^2 l^2 \frac{d^2\lambda}{dt^2} + \left(\frac{16}{3} St\, l\, u_o \frac{d\lambda}{dt}\right) + \left[4u_o^2 + \frac{8}{3} St\, l \frac{du_o}{dt}\right] \lambda =$$

$$4u_o^2 + \left(\frac{20}{3} St\, l \frac{du_o}{dt}\right) + \frac{48}{Re} l\, u_o \qquad (4.8)$$

with initial conditions $d\lambda/dt = 0$ and $\lambda = 1$ at $t=0$. The third term at the right hand side of (4.8) is the contribution of the fluid viscosity. Equation (4.8) is integrated with a standard central difference method. For Re = 300, the result is given in figure 4.19. Clearly, the numerical results agree much better with those of the extended analytical model than with those of the original one, especially in the early phase of the valve closure. In the later stages, both the original and the extended analytical model become inaccurate. The assumption that $|\lambda - 1| \ll 1$ is not satisfied then. Furthermore, the velocity profile is not a quasi-steady parabolic one then, since unsteady flow development will occur. This is indicated by the Womersley parameter α, with $\alpha^2 = Re\ St > 12$, which is the ratio of inertial over viscous forces. Unsteady flow development would only be negligible if $\alpha \ll 1$.

4.6 Discussion

From the results in the previous sections it is concluded that the interaction model, combined with the finite element model, can be successfully applied to the analysis of the interaction between the fluid flow and the valve motion. It is expected that the model is also applicable to other comparable fluid-structure interaction problems, characterized by highly coupled, nonlinear system equations, complex fluid phenomena and large structure displacements. An unconditional numerical stability has been achieved.

The close agreement between the experimental and numerical results for the falling valve problem suggests that the discrepancy between the experimental and numerical unsteady fluid moments is not caused by the numerical fluid model but mainly by a shortcoming of the experimental setup.

The number of position estimates required to locate the dynamic or steady equilibrium position at each timestep varies from five to eight. In general, two or three estimates are needed to bracket the equilibrium position and the remainder is used by Brent's algorithm in order to locate it within the required accuracy (10^{-4} rad). Per position estimate, between two and eight Newton iterations are necessary to solve the fluid problem. The number of Newton iterations decreases when the equilibrium position is being reached, since a better initial estimate for the Newton iteration is available. For the typical number of unknowns of 721, the numerical procedure requires about 30 minutes computing time per time step on an Apollo DN3000 minicomputer and about 1.5 minutes on an Alliant FX/4 mini-supercomputer with two parallel vector processors. This gain of a factor 20 is caused mainly by a higher clock speed (factor 4) and by the vectorization of the matrix solving routine (factor 4). Parallelism has only a small effect (factor 1.2).

Restrictions for the application of the interaction model are imposed by the finite element fluid model. It would be preferable if the time integration scheme would be second order accurate in order to eliminate numerical damping as a possible error source and to reduce the number of time steps while keeping the same accuracy. Furthermore, the range of the Reynolds number is not large enough to apply it to fully physiological flow rate situations ($Re_{max} \approx 4500$). Finally, the analysis of flow around far closed valves requires many elements and therefore much computational effort. On the other hand, the effect of the Reynolds number is not a dominant one in the analyzed range and since no new physical phenomena are expected beyond that range, this restriction is not an essential one. Furthermore, the fluid-interaction strategy as developed here, can easily be combined with any numerical or analytical fluid solver, which meets the requirements for a particular problem, as is illustrated by the quasi-one-dimensional and von Mises models.

The fully free valve (k=0) corresponds to a disc-type valve prosthesis, which is allowed to move freely (within limits). As is shown here (figure 4.15), such a valve is able to close due to flow deceleration, just as the natural valve does. Here, no full valve closure is achieved (the valve closes only for about 65%) since no back flow is present. If the simulation of a full physiological flow cycle is required, including back flow and full valve closure, the model must be extended with a closure algorithm, which is not included in the present model.

5. SEGMENTED VALVE

In this chapter, the multiple degrees of freedom model is applied to a segmented valve consisting of four rigid segments. The fluid field will be calculated using the finite element fluid model. In sections 5.1 and 5.2 the model is validated by a comparison with experimental results. In section 5.3 more features of the model are demonstrated in a short parameter study.

5.1 Free valve in a steady flow

The equilibrium position of the valve is studied as a function of the Reynolds number. A global presentation of the numerical results is given in figure 5.1. Just as in the rigid valve case, the valve opens more if the Reynolds number is increased. Due to the presence of buoyancy the shape of the valve is concave. If no buoyancy was present, at Re = 0 the valve would be straight in a position of 0.39 rad (22.5^{o}), which is the angle of fixation. With increasing Reynolds number, the shape and the curvature of the valve hardly changes. This valve behavior is also observed during the experiments. Apparently, the bending forces are relatively large compared to the variation of the fluid force.

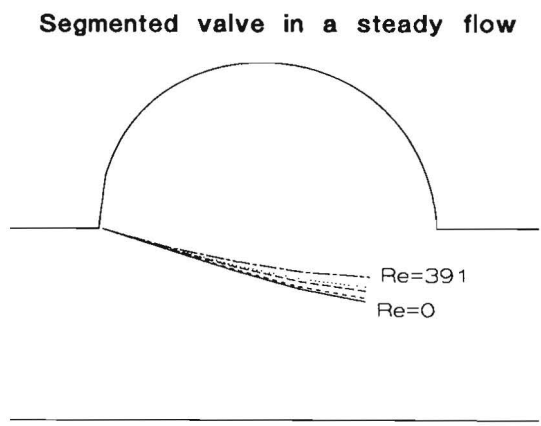

figure 5.1 Numerical position of a segmented valve in a steady flow for various Reynolds number (parameters determined from a subset of the parameter estimation experiments)

A comparison between numerical and experimental results is shown in figure 5.2. The relative valve opening (the space between valve tip and bottom divided by the channel height) is plotted as a function of the Reynolds number. If the valve parameters are estimated using the full set of parameter estimation experiments as discussed in chapter 3, then the agreement is only modest, albeit well within the predicted accuracy limits given in chapter 3. Experimentally, the valve hardly changes position. Numerically, the valve starts at a more closed position but if the Reynolds number is increased it opens faster, until at Re = 400 the agreement is close. The deviations can be explained partly from the sensitivity of the valve parameters to the measurement errors in the parameter estimation experiments. Furthermore, it can be argued that only a subset of the rather arbitrary set of valve positions in the valve parameter estimation experiments are relevant for the flow situation at hand, namely those situations in which the valve is pushed upward and when it has a concave shape. If the valve parameters are estimated using only such a subset, then the agreement improves, as is demonstrated in figure 5.2.

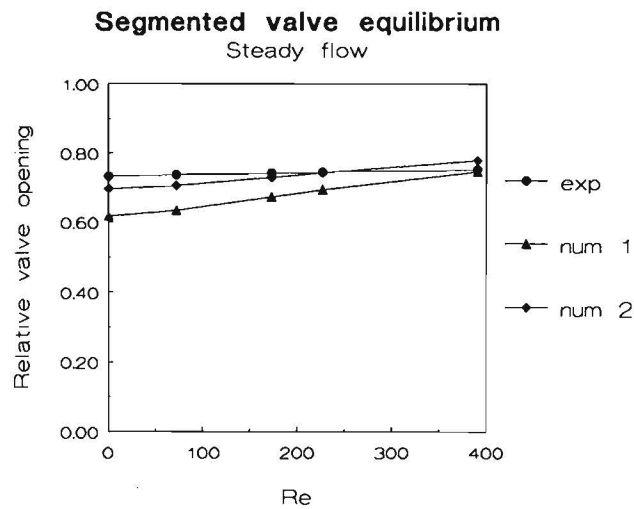

figure 5.2 Experimental and numerical relative valve opening of a segmented valve in a steady flow for various Reynolds numbers (num 1: valve parameters determined form all available parameter estimation experiments, num 2: valve parameters determined from a subset of the parameter estimation experiments)

5.2 Free valve in a pulsatile flow

In order to validate the computation of the dynamic behavior of the segmented valve, the motion due to a pulsatile flow is studied both experimentally and numerically. As shown in figure 3.5, The flow rate changes as a function of time in a similar way as in the rigid valve case. Figure 5.3 globally shows the valve position at some characteristic points of time. At t=1, the onset of the systolic phase, the valve is in its

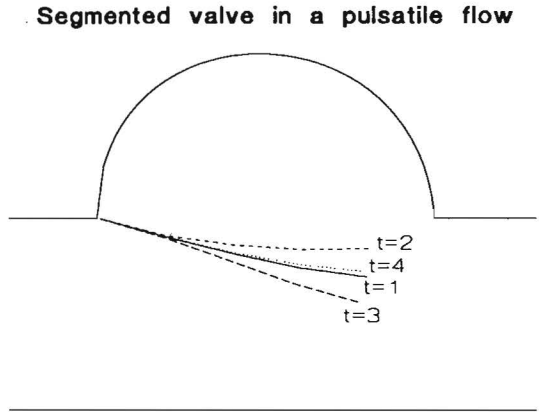

figure 5.3 Numerical position of a segmented valve in a pulsatile flow (Re = 178, St = 0.83, valve parameters determined from subset of parameter estimation experiments)

steady state position, corresponding to Re = 0 in figure 5.1. At t=2, the instant of maximum flow rate, the valve is at its maximum opened position. During the second part of the systolic phase the valve tends to close due to flow deceleration and bending stiffness. At t=3, the end of the systolic phase, the valve has reached its maximal closed position, which is further closed than the steady state position. Afterwards, it moves gradually back to its steady state position. Due to buoyancy, the shape of the valve remains nearly always concave, very similar to the steady state cases of figure 5.1. Only at t=3, a slight S-form of the valve is observable. Since the bending forces are relatively large compared to the fluid forces, the displacement and deformation of the valve is only modest. A comparison between experimental and numerical data is given in figures 5.4 and 5.5, where the relative valve opening is plotted as a function of time. The numerical results in figure 5.4 are obtained with valve parameters determined from the full set of parameter estimation results, as

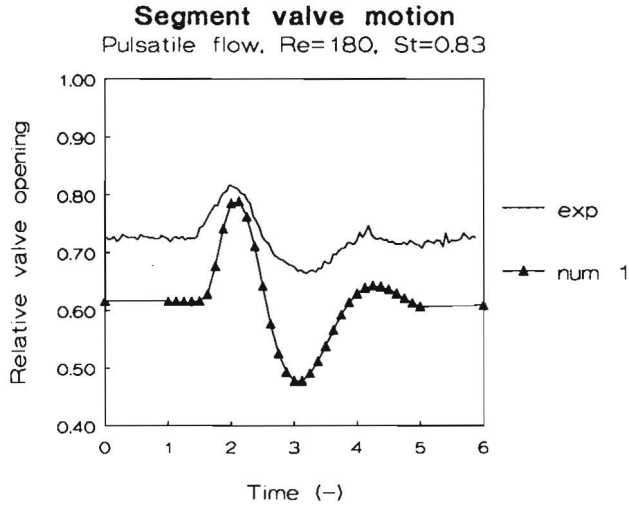

figure 5.4 Experimental and numerical relative valve opening of a segmented valve in a pulsatile flow as a function of time (valve parameters determined from all available parameter estimation experiments)

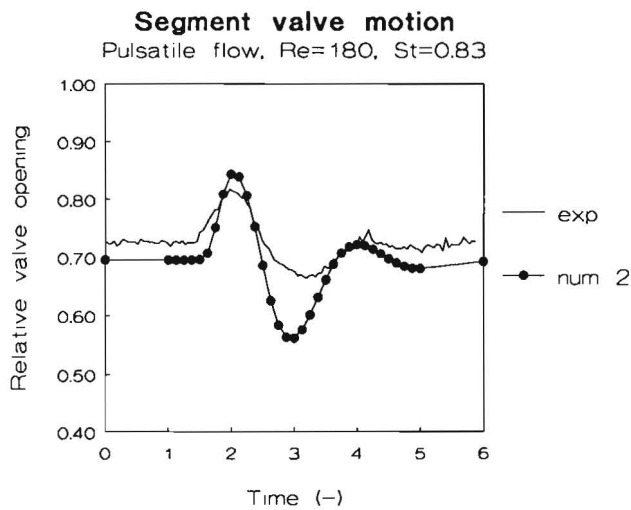

figure 5.5 Experimental and numerical relative valve opening of a segmented valve in a pulsatile flow as a function of time (valve parameters determined from a subset of the available parameter estimation experiments)

discussed in chapter 3 and in the previous section. The qualitative agreement is fair. Both the experiment and numerical simulation show the behavior discussed above. In addition, they show a local maximum at t=4, which is in the early phase of the diastolic phase. The quantitative agreement shows similar deviations as in the steady state case of the previous section. The diastolic position shows the same deviation as the steady state position at Re = 0. Furthermore, the numerical valve amplitude is larger than is observed experimentally. For the major part this can be explained from the steady state deviation observed in figure 5.1. If the valve parameters are estimated using the same subset of parameters estimation experiments, as discussed in the previous section, the quantitative agreement improves (cf. figure 5.5). Especially, the diastolic position agrees much better. The difference in valve amplitude is not diminished. The remaining deviations are attributed to the limited accuracy of the estimation of the valve parameters and to the presence of a boundary layer at the front and rear wall of the experimental model, which slows down the valve motion in a similar way as discussed in the previous chapter. This three-dimensional phenomenon is not included in the two-dimensional numerical model.

5.3 Parameter variation

With the numerical model for the segmented valve some more simulations are performed. Since the model is intended for application to flexible leaflet valves, some special attention will be paid to the role of the bending stiffness. Also the Strouhal number is varied and both a pulsatile and a harmonically varying flow rate are applied. Furthermore, the results are given of an indicative experiment with a two-dimensional flexible leaflet valve.

In this section, a pulsatile flow rate is used, which is given by

$$\begin{aligned} u_0 &= \sin^2(\tfrac{1}{2}\pi t) && \text{if } 0 \le t < 2 \\ &= 0 && \text{if } 2 \le t < 4 \end{aligned}$$

with a periodicity of 4, shown in 5.6. The systolic phase is very similar to the one defined in chapter 3. The diastolic phase is shorter to resemble the flow conditions of the earlier performed flexible leaflet experiments.

Figure 5.7 shows the experimentally observed motion of a two-dimensional, very thin flexible leaflet valve due to the pulsatile flow. At t=0, the valve leaflet is almost straight and nearly fully opened. During flow acceleration (0<t<1), the valve is

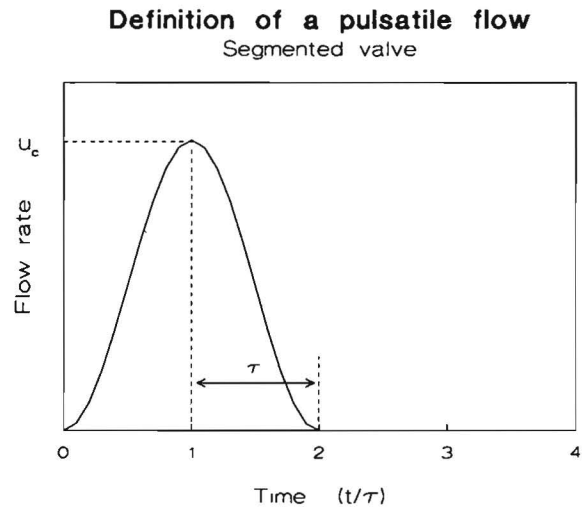

figure 5.6 Definition of the pulsatile flow rate as used in this section

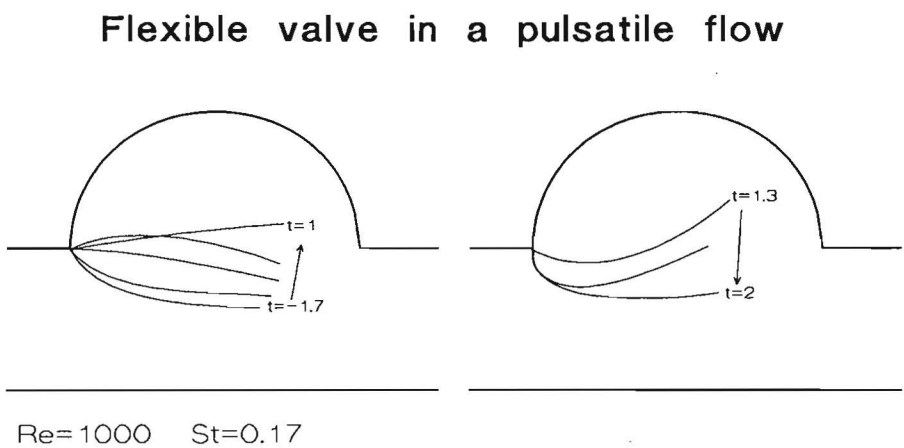

figure 5.7 Experimentally observed motion of a flexible valve in a pulsatile flow

pushed into the sinus and the shape of the valve is convex. During flow deceleration ($1<t<2$), the valve starts to close, beginning with the part close to the point of attachment, since there the pressure difference over the valve is larger than at the valve tip. The shape of the valve quickly changes into a concave one, with the largest curvature close to the point of attachment. The motion of the valve tip lags behind and the curvature change is only modest at that point. During the diastolic phase ($2\leq t\leq 4$), the valve tip comes at equal height as the rest of the valve and the valve more or less stretches itself. The maximum valve closure is about 50%. Due to viscous damping in the boundary layers at the front and rear wall of the experimental model, the sides of the valve near the boundary do not move exactly in phase with the center part of the valve. So, the valve does not remain flat, but it is curved in the direction perpendicular to the model plane. The positions shown in figure 5.7 are those of the center part of the valve. Because of this, the results of this experiments have only an indicative value.

In figure 5.8 some results of numerical simulations for a segmented valve are given. As in chapter 4, a relative bending stiffness parameter k is used, where k=1 corresponds to the experimental case. The absolute bending stiffness in the contact points of the segmented valve is about equal to the bending stiffness in the point of attachment of the rigid valve. Buoyancy is not present here. The fixation angle of the valve (and so its equilibrium position at Re=0) is 0.39 rad (22.5^{o}). In order to restrict the amount of computation time the Reynolds number is chosen to be 300, which is 30% of its value during the experiments.

First, the Strouhal number is chosen equal to that of the flexible valve experiment, i.e. St = 0.17. Figure 5.8a shows the results for a relative stiff valve (k=0.1). At the start of the systolic phase, the valve is nearly at its maximum closed position (about 80% closed). During flow acceleration it opens until at t=1 (maximum flow rate) it is in nearly fully opened position. During the deceleration phase and the diastolic phase it moves again towards the closed position. The maximum closed position is reached just before the end of the diastolic phase. Then, due to its bending stiffness, the valve bounces back, just before it is accelerated by the fluid flow. Also due to the bending stiffness, the shape of the valve is concave if it is opened further than its equilibrium position and convex if it is closed further than this position. The motion of the valve tip is in phase with the part close to the point of attachment. The overall behavior of this rather stiff valve resembles that of the rigid valve. Figure 5.8b shows that when the bending stiffness is decreased by a factor 5 (k=0.02), no essential changes in the valve behavior are observed. The valve amplitude and the curvature changes are somewhat larger. Apparently, the stiffness

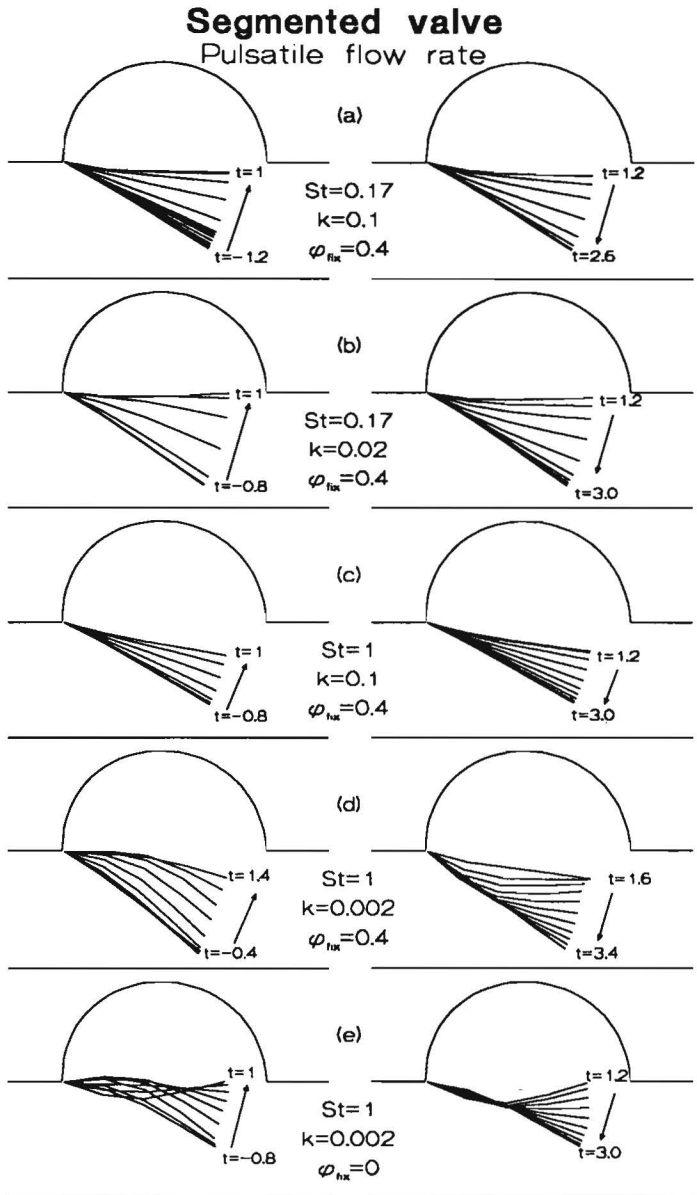

figure 5.8 Numerical simulation of the motion of a segmented valve in a pulsatile flow for various values of the Strouhal numbers St, the relative bending stiffness k and the fixation angle (Re = 300, Δt=0.2)

of the valve is still larger than in the experimental case of the fully flexible valve.

For the pulsatile flow and a Strouhal number of St = 0.17, no convergence has been obtained for $k < 0.02$. Unlike the rigid valve model, the segmented valve model does not converge unconditionally. No strict convergence limit is encountered but the convergence slows down more and more if the bending stiffness and/or the Strouhal number is decreased, until the limits of the available computation time are reached. This decreasing rate of convergence is caused by the fact that the dynamical equilibrium position becomes undetermined if both the internal forces due to the bending stiffness and the external forces due to the fluid flow become zero. Especially in the diastolic phase, in which also the steady component of the fluid force is absent, this situation may occur or at least may be approached. Apparently, for cases close to this undetermined state, the residual moment varies so little close to the minimum that it can not be located accurately. An incidental cause for the breakdown of the convergence process is that sometimes a valve position must be evaluated which is beyond the capacity of the mesh generator or the fluid solver, e.g. a case in which a part of the valve lies outside the fluid domain. Additional precautions, which are not taken here, would circumvent these events.

If the Strouhal number is increased to St = 1, then for k=0.1 (figure 5.8c) the valve behavior is similar to that of the St = 0.17 case. Due to the increase of the inertial effects the valve amplitude is somewhat less. For St = 1, the bending stiffness can be decreased further. Convergence is obtained for k down to k=0.002, a factor 500 less than the reference case. The result is shown in figure 5.8d. Now, the valve behavior has changed. The curvature changes have increased and resemble more the experimental case of the fully flexible valve. The motion of the valve tip lags behind that of the part close to the point of attachment. During valve acceleration ($0 \le t < 1$) the valve has a convex shape whereas its shape is concave during flow deceleration ($1 \le t < 2$). As in the previous cases, the valve displacement is large. Figure 5.8e demonstrates the effect of the fixation angle. It has been changed from 0.39 rad (22.5°) to 0°. As might be expected, the valve position range is shifted somewhat more into the sinus, resulting in a less complete valve closure. The agreement with the experimental results shown in figure 5.7 is improved.

Some more details of the velocity field are shown in figure 5.9 for the case earlier shown in figure 5.8d. Globally, the results resemble those of the rigid valve case, shown in chapter 4. At the start of the systolic phase, the valve is in its maximum closed position and the fluid velocities are small. A weak vortex behind the valve is persisting from the previous period. During flow acceleration the valve

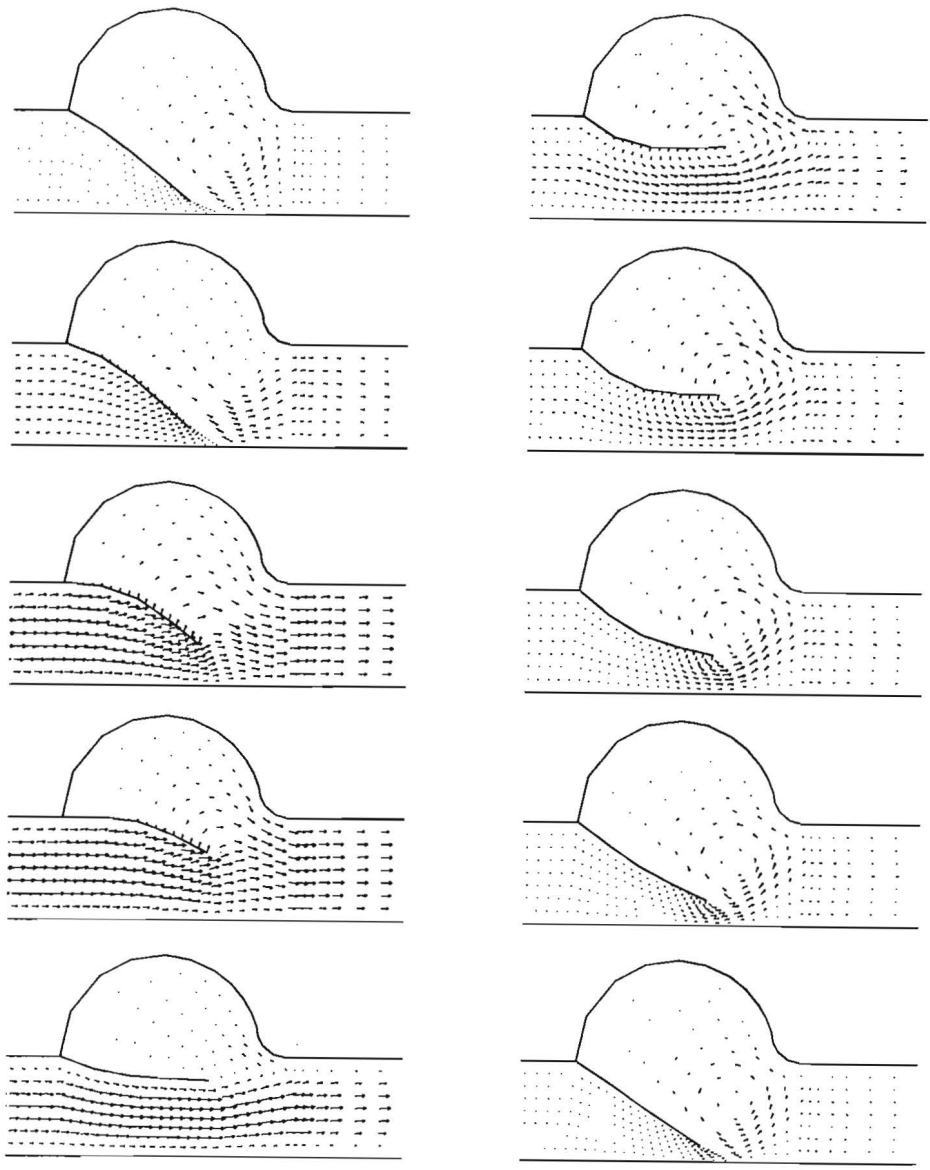

figure 5.9 Velocity field for a segmented valve in a pulsatile flow (Re = 300, St = 1, k = 0.002) upper left: t=0, bottom right: t=3.6, Δt=0.4

moves up and the contents of the sinus is pushed out. The vortex disappears. The valve reaches its maximum opened position halfway the deceleration phase. Then its shape changes from convex to concave and it starts closing. A new vortex is formed behind it. In the diastolic phase, the valve keeps moving down and finally stretches itself. The vortex is diffusing until the start of the new flow cycle.

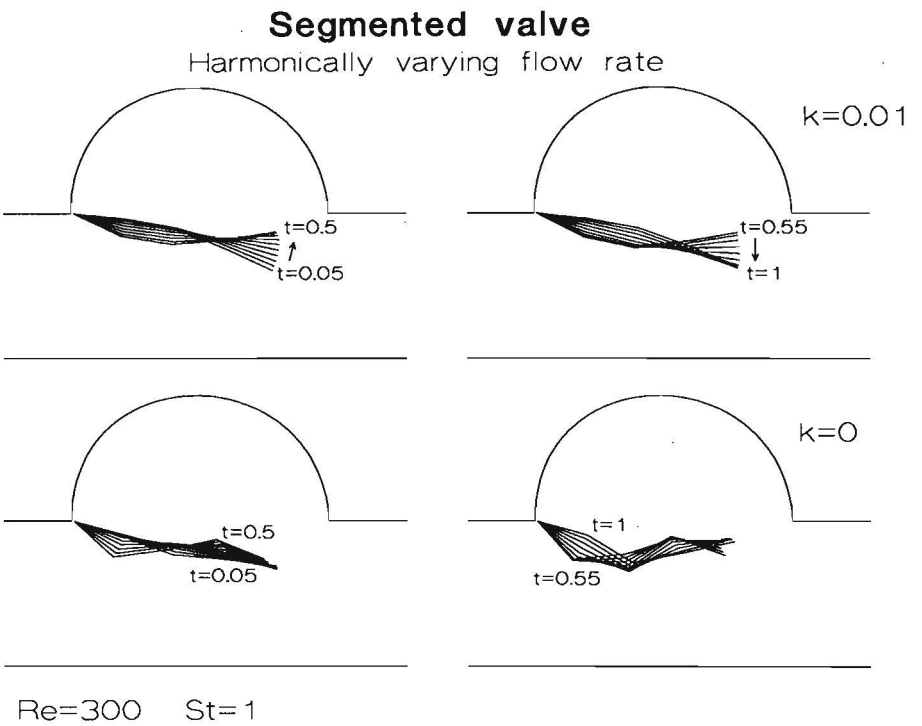

figure 5.10 Numerical simulation of the motion of a segmented valve due to a harmonically varying flow rate for various relative bending stiffness k (Re=300, St=1, Δt=0.05)

In the previous cases, the flow rate has been pulsatile according to figure 5.6. Then, the valve amplitudes are large but the curvature changes are only modest. The curvature changes increase if the valve becomes more flexible and if the fluid inertial forces become larger. In order to demonstrate the capabilities of the model, also the case of a harmonically varying flow rate according to figure 4.14 is studied. The Strouhal number is chosen to be St = 1, with the characteristic time defined as the periodic time. The results are shown in figures 5.10 and 5.11. Generally, the valve displacement is much smaller than for a pulsatile flow. The curvature changes

are much larger and that holds also for the phase difference between the motion of the valve tip and that of the part close to the point of attachment. The latter moves more or less in phase with the flow rate, while the valve tip may lag considerably behind. If k=0.01 (figure 5.10a) both parts of the valve have approximately an opposite phase, resulting in a resonance-like behavior. If the bending stiffness is set equal to zero (for which convergence is achieved in this case) the valve motion becomes wave-like, with large deformations and different parts of the valve moving in different directions. The latter is clearly visible in figure 5.11. Due to the absence of the diastolic phase and the relative large inertial fluid forces, it is less likely that the dynamic equilibrium of the valve becomes nearly undetermined than in the case with pulsatile flow rate. This is reflected in the range of convergence, which is wider and also incorporates the fully flexible valve with k=0. For the previous simulations, four segments seem to be sufficient. A practical application of the k=0 case would require a larger number of segments.

5.4 Discussion

From the results of the previous sections it is concluded that the interaction model can be applied to heart valve models and other fluid-structure systems with more than one degree of freedom. The qualitative agreement between the experimental and numerical results is good. The quantitative agreement is reasonable. If the valve marker positions are measured more accurately and if more attention is paid to the choice of parameter estimation experiments, a better agreement may be expected. For this study, a valve consisting of four rigid segments appeared to yield an adequate description of the behavior of a flexible valve, except when the deformation is very large. The numerical segmented valve model yields results similar to those of an indicative experiment with a flexible leaflet valve.

If the valve is relatively stiff, the algorithm converges rapidly and the required amount of computation time is limited. The number of Newton iteration steps per time step (which each requires the solving of the fluid system) is comparable to the number in the rigid valve case. However, if the valve becomes more flexible, the number of position estimates and Newton iterations increases. No strict convergence limit has been encountered. In practice, the convergence is limited by the amount of computation time available. The largest computational effort, encountered in this study, was a requirement of about 2900 Newton iterations for one individual timestep, using about 4 hours CPU on an Alliant FX/4. Additional safeguards may be added to the algorithm in order to prevent incidental breakdown of the computation

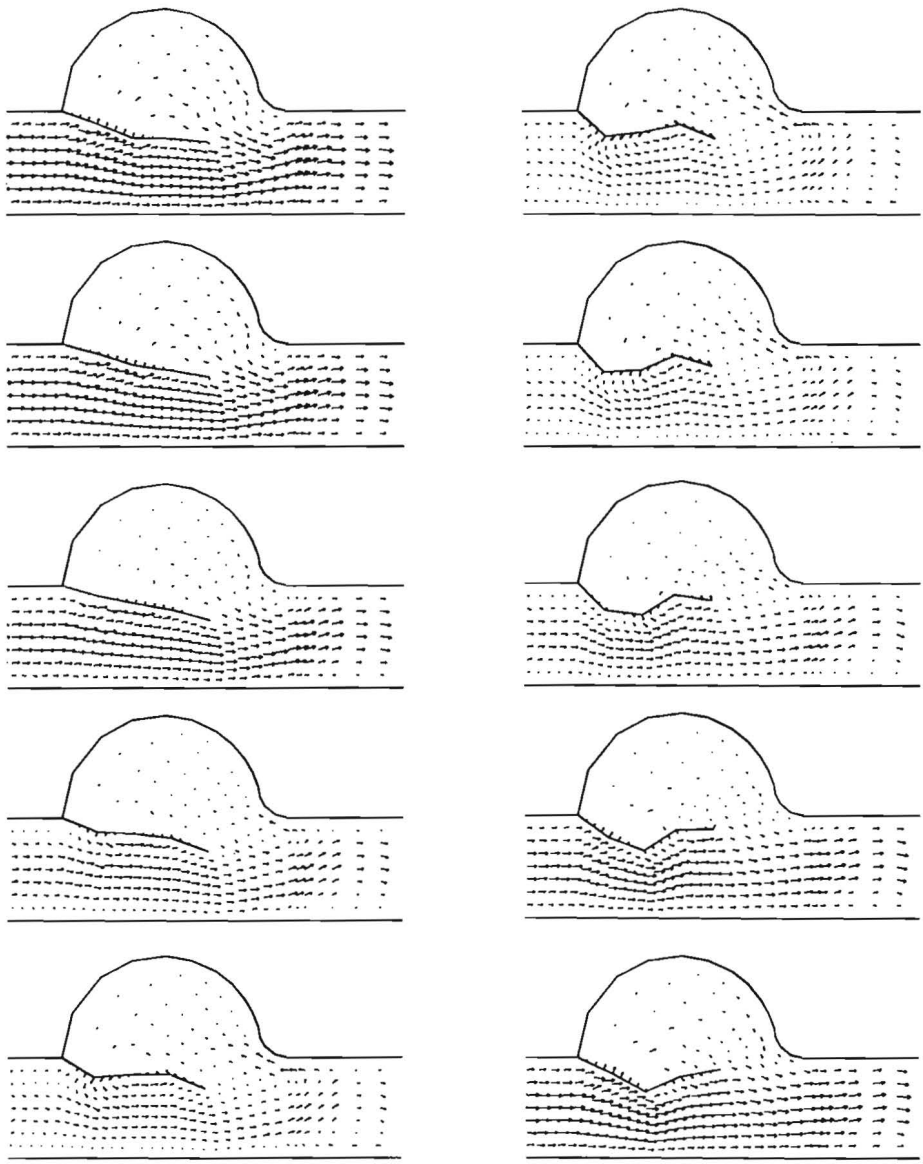

figure 5.11 Velocity field for a segmented valve in the case a harmonically varying flow rate (Re = 300, St = 1, k = 0.0) upper left: t=0, bottom right: t=0.9, Δt=0.1

when a valve position must be evaluated which is beyond the capability of the mesh generator or the fluid solver.

Like in the rigid valve case, it would be preferable when the time integration scheme would be second order accurate and when the Reynolds number could be increased to physiological values.

If the simulation of a full physiological flow cycle is required, including back flow and full valve closure, the model must be extended with a closure algorithm, which is not included in the present model.

6. Summary and conclusions

In the present study a numerical fluid-structure interaction model has been developed for the analysis of the dynamic behavior of a prosthetic heart valve. Experiments have been performed to validate the numerical results.

Two different valve types have been considered. The first is a rigid valve which can rotate around its point of attachment. It resembles the case of a disc-type valve prosthesis, which has only one degree of freedom. The second type is a segmented valve, consisting of several rigid segments connected to each other. This type is intended for the design of valve prostheses with more degrees of freedom such as flexible bio-prosthetic or artificial leaflet valves. The buoyancy, the bending stiffness and the load due to the fluid flow are included in the valve equilibrium equation. Friction in the contact points and the inertia of the valve have not been considered, but could be incorporated easily if desired. The constitutive equations may be nonlinear. Large displacements and deformations are allowed.

Various fluid models have been incorporated in the fluid-structure interaction model. The simplest is a quasi one-dimensional analytical model. It is based on Bernoulli's theorem and conservation of mass. Velocity gradients in radial direction are not considered in this model. Somewhat more advanced is the model of von Mises (Gurevich, 1967). This is a two-dimensional potential flow model which explicitly takes into account the contraction of the flow behind the valve. Both models have been applied to a rigid valve in a steady state position. Furthermore, a finite element fluid model based on the two-dimensional unsteady Navier-Stokes equations has been applied. This model gives a full description of the fluid flow in complex shaped domains. The Navier-Stokes and continuity equations are spatially discretized by means of a standard Galerkin finite element method. A 7-noded triangular element is used in which the velocity is approximated by an extended quadratic function. The pressure is approximated by a linear function being discontinuous over the element boundaries. The pressure unknowns are eliminated from the momentum equation using a penalty function approach. The time integration is performed with an Euler implicit scheme. As a contact condition on the valve, the fluid velocity is set equal to the local valve velocity. This velocity is determined from the actual valve position and the position at the previous point in time. The spatial accuracy of the velocity is of third order. The accuracy of the pressure is of second order. The temporal accuracy is of first order for as well as the velocity and the pressure. The finite element fluid model has been applied to both the rigid and the segmented valve. Reynolds numbers up to 1100 have been achieved, which are

lower than the physiological value of 4500. The Strouhal number has been varied between 0.06 (the physiological value) and 2.

The coupled fluid-structure system is solved by a fully coupled, iterative method: both the fluid and the structure subsystem are evaluated separately (one subsystem is solved while the other is kept constant) and an iteration is performed until equilibrium is achieved. Since the rigid valve has only one degree of freedom, its equation of motion is a nonlinear scalar equation. The root of this equation corresponds to the equilibrium position. The method of Brent (1973) is used to locate this root. This method does not require the evaluation of derivatives with respect to the valve position (which are not available in the present study) and it combines robustness with a fast local convergence. The equilibrium position of the segmented valve is found by formulating the problem as a nonlinear least squares problem in which the sum of the squares of the residual segment moment is minimized. Powell's hybrid method (Powell, 1970) has been applied for this minimization. Like Brent's method it does not require the evaluation of derivatives and it combines robustness and fast local convergence.

Experiments have been performed to validate the fluid-structure interaction models. The computation of the velocity field has been checked by comparing the results to those of laser-Doppler measurements. The computed fluid load exerted on the valve has been compared with experimental data obtained with a force transducer mounted to the valve. The valve motion has been recorded with a video system and compared to numerical predictions. Steady and unsteady cases have been considered. Separate experiments have been performed to determine the parameters in the constitutive equations.

The results of the rigid valve model are quite satisfactory. The quasi one-dimensional fluid model and the von Mises model have been applied to compute the fluid load due to a steady flow and the steady equilibrium position as a function of the Reynolds number. They yield good qualitative agreement with the experiments. However, the quantitative agreement of the quasi one-dimensional model is poor, whereas the von Mises model gives much better results. This indicates that the two-dimensionality of the flow, in the form of flow contraction behind the valve, is an important phenomenon in this steady flow case. The finite element method proves to yield the most accurate results. The agreement between experiments and numerical simulations is close. In case of an unsteady flow some small deviations occur, which can be attributed to spurious three-dimensional flow phenomena in the experimental model. The model valve shows an early state closing behavior which resembles that of the natural aortic valve. The influence of

the Reynolds number, the Strouhal number and the bending stiffness has been analyzed. As expected, the valve amplitude increases if the valve becomes less stiff. The effect of the Reynolds number on the valve motion is not a dominant one. So, it is believed that results, obtained for lower Reynolds numbers than the physiological ones, are useful for physiological applications. The Strouhal number is more important. An unconditional numerical stability is achieved, independently of the bending stiffness and buoyancy, which both may be zero.

The segmented valve model demonstrates a good qualitative agreement between the experimental and numerical results. Some deviations occur due to the limited accuracy of the constitutive parameters of the valve and due to three-dimensional flow phenomena in the experimental model. When the bending stiffness is small, the valve shows large displacements and large curvature variations. The numerical solution procedure converges to the dynamic equilibrium position for a wide range of parameter sets. Also in cases without any buoyancy and bending, convergence has been obtained. The behavior of a four segment valve resembles largely that of a fully flexible valve.

It is believed that the fluid-structure interaction models presented in this study may contribute to the development of improved heart valve prostheses. In the present form the models can be used for an indicative study of the dynamic behavior of existing or newly developed one- or bileaflet disc type or flexible leaflet type prostheses. If required, valve inertia or visco-elasticity can easily be incorporated. For a complete analysis of the dynamic valve behavior a three-dimensional fluid model must be applied. Furthermore, some special care should be taken to incorporate the possibility of full valve closure, which is not considered in the present study.

Apart from the application to heart valve prostheses, the models can be used for a rather general class of fluid-structure interaction problems. The model will be useful especially in those cases in which a full description of the fluid is required, when the structure has a relatively few degrees of freedom and when the structure displacements and deformations are large. If a full description of the fluid is not required, an analogous fully coupled iterative approach can be used with a simplified fluid model, as has been demonstrated with the quasi one-dimensional and potential fluid models. If the structure has negligible inertia, internal damping and stiffness during at least part of the computation, fully coupled iterative methods, like the ones at hand, are probably the only applicable methods.

References

- Arts, M.G.J., *A mathematical model of the dynamics of the left ventricle and the coronary circulation,* PhD-thesis, University of Limburg, Maastricht, The Netherlands, 1978
- Batchelor, G.K., *An introduction to Fluid Dynamics*, Cambridge University Press, Cambridge, Great Britain, 1983
- Bellhouse, B.J. & L. Talbot, "The fluid mechanics of the aortic valve", *J. Fluid Mechanics vol 35*, pp721-735, 1969
- Belytschko, T, "Fluid- structure interaction", *Computers and structures vol 12*, pp459- 470,1980
- Bergel, D.H. (ed), *Cardiovascular fluid dynamics,* Academic Press, London, 1972
- Box, M.J., "A comparison of several current optimization methods and the use of transformations in constrained problems", *Comput. J. 9*, pp67-77, 1966
- Brent, R.P., *Algorithms for minimization without derivatives*, Prentice- Hall, Englewood Cliffs, N.J., USA, 1973
- Caro, C.G., J.G. Pedley, R.C. Schroter & W.A. Seed, *The mechanics of the circulation*, Oxford University Press, Oxford, 1978
- Cuvelier, C., A. Segal & A.A. van Steenhoven, *Finite element methods and Navier- Stokes equations*, D. Reidel Publishing Company, Dordrecht, The Netherlands, 1986
- Frederiks, W., H.C.J. Hilberink & J.A. Sparenberg, "On the Kutta condition for the flow along a semi-infinite elastic plate", *J. Engin. Math. v20,* pp27-50, 1986
- Gad-el-Hak, M., "Boundary layer interactions with compliant coatings: an overview", *Applied Mechanics Review v39 n4*, pp511-523, 1986
- Gill, P.E., & W. Murray, "Algorithms for the solution of the nonlinear least-squares problem", *Siam. J. Numer. Anal. vol 15 n 5*, pp977-992, 1978
- Gurevich, M.I., *Theory of jets in ideal fluids*, Academic Press, New York, 1965
- Idelsohn, S.R., L.E. Costa & R. Ponso, "A comparative study of blood flow through prosthetic heart valves using the finite element method", *J. Biomechanics v18 n2*, pp97-115, 1985
- Kulak, R.F., "A finite element quasi-Eulerian method for fluid-structure interaction in three-dimensional space", *J. Pressure Vessel Technol. 103*, pp183-190, 1981
- Kulak, R.F., "A finite element formulation for fluid-structure interaction", *Computers & Structures vol 18 n 2*, pp319-332, 1984
- Kulak, R.F., "Three-dimensional fluid-structure coupling in transient analysis", *Computers & Structures vol 21 n 3*, pp529-542, 1985
- Lee, C.S.F & L. Talbot, "A fluid-mechanical study of the closure of heart valves", *J. Fluid Mech. v91*, pp41-63, 1979
- Milne-Thomson, L.M., *Theoretical aerodynamics*, Dover Publications, New York, USA, 1966
- Milnor, W.R, *Hemodynamics*, Williams & Wilkins, Baltimore, USA, 1982
- Nerem, R.M. & W.A. Seed, "An in vivo study of aortic flow disturbances", *Cardiovasc. Res. v6*, pp1-14, 1972
- Peters, G., *Tools for the measurement of stress and strain fields in soft tissue, application to the elbow joint*, PhD-thesis, Eindhoven University of Technology, Eindhoven, The Netherlands, 1987
- Park, K.C. & C.A. Felippa, "Partitioned analysis of coupled systems", in: T. Belytschko & T.J.R. Hughes (eds.), *Computational methods for transient analysis*, North- Holland, Amsterdam, 1983

- Peskin, C.S., "Numerical analysis of blood flow in the heart", *J. of Comp. Physics vol 25*, pp220- 252, 1977
- Powell, M.J.D., "A hybrid method for nonlinear equations", in: P. Rabinowitz (ed.), *Numerical methods for algebraic equations*, Gordon & Breach, 1970
- Press, W.H., B.P. Flannery, S.A. Teukolsky & W.T. Vetterling, *Numerical Recipes*, Cambridge University Press, New York, 1986
- Reid, K., "The anatomy of the sinus of Valsalva", *Thorax v25 n79*, pp79-85, 1970
- Renterghem, R.J. van, *Aortic valve geometry during cardiac cycle*, PhD-thesis, University of Limburg, Maastricht, The Netherlands, 1983
- Rousseau, E.P.M., *Mechanical specifications for a closed leaflet valve prosthesis*, PhD-thesis, Eindhoven University of Technology, Eindhoven, The Netherlands, 1985
- Sauren, A.A.H.J., *The mechanical behaviour of the aortic valve*, PhD-thesis, Eindhoven University of Technology, Eindhoven, The Netherlands, 1981
- Scales, L.E., *Introduction to nonlinear optimization*, Macmillan, 1985
- Segal, A., *SEPRAN Manual*, Ingenieursbureau SEPRA, Delft, The Netherlands, 1984
- Steenhoven, A.A. van, *The closing behaviour of the aortic valve*, PhD-thesis, Eindhoven University of Technology, Eindhoven, The Netherlands, 1979
- Steenhoven, A.A. van & M.E.H. van Dongen, "Model studies of the closing behaviour of the aortic valve", *J. Fluid Mechanics v90*, pp 21- 32, 1979
- Steenhoven, A.A. van & Dongen, M.E.H. van, "Model studies of the aortic pressure rise just after valve closure", *J.Fluid Mech. v166*, pp93-113, 1986
- Stevenson, D.M. & A.P. Yoganathan, "Numerical simulation of steady turbulent flow through trileaflet aortic valves I: computational scheme and methodology", *J. Biomechanics v18 n2*, pp899-907, 1985
- Swanson, W.M. & R.E. Clark, "Dimensions and geometric relationships of the human aortic valve as a function of pressure", *Circ. Res. v35*, pp871-882, 1974
- Thalassoudis, K. & J. Mazumdar, "Mathematical model for turbulent blood flow through a disc-type prosthetic heart valve", *Med. & Biol. Engin. & Comput v22*, pp529-536, 1984
- Thubrikar, M.J., Skinner, J.R., Eppink, R.T. & Nolan, S.P., "Stress analysis of porcine bioprosthetic heart valves in-vivo", *J.Biomed. Mater. Res. v16*, pp811-826, 1982
- Tu, C. & C.S. Peskin, "Stability and instability in the computation of flows with moving immersed boundaries: a comparison of three methods", Personal communication, 1989
- Wippermann, F.K., "On the fluid dynamics of the aortic valve", *J. Fluid Mechanics vol 159*, pp 487- 501, 1985
- Vosse, F.N. van de, A.A. van Steenhoven, A. Segal & J.D. Janssen, " A finite element analysis of the unsteady two- dimensional Navier- Stokes equations", *Int. J. of Numerical Methods in Fluids vol 6*, pp427- 443,1986
- Vosse, F.N. van de, *Numerical analysis of carotid artery flow*, PhD-thesis, Eindhoven University of Technology, Eindhoven, The Netherlands, 1987

List of symbols

Convention

a	scalar
$\dot{a}$	rate of a
$\vec{a}$	vector
$\dot{\vec{a}}$	rate of $\vec{a}$
$\underset{\sim}{a}$	column of scalars
$\underset{\sim}{a}^T$	transpose of $\underset{\sim}{a}$
$\boldsymbol{A}$	second-order tensor
$\boldsymbol{A}^c$	conjugate of $\boldsymbol{A}$
$\boldsymbol{A}^{-1}$	inverse of $\boldsymbol{A}$
$\underline{A}$	matrix of scalars
$\underline{A}^T$	tranpose of $\underline{A}$
$\underline{A}^{-1}$	inverse of $\underline{A}$
$\vec{a}\cdot\vec{b}$	dot product
$\det(\boldsymbol{A})$	determinant of $\boldsymbol{A}$
$\boldsymbol{A}:\boldsymbol{B}$	double dot product of two tensors

Symbols

$\vec{f}$	force
h	local vertical valve position
$\boldsymbol{I}$	unit tensor
k	bending stiffness, relative to reference case
l	valve/segment length
$\underline{L}$	divergence matrix
l_g	buoyancy force lever
m	valve/segment moment with respect to fixation point
$\underline{M}$	mass matrix
n	number of segments
$\vec{n}$	normal vector
$\underline{N}$	convection matrix
p	pressure
Re	Reynolds number
s	local coordinate along valve

S	Gauchy stress stensor
$\underline{S}$	diffusion matrix
St	Strouhal number
t	time
$\vec{t}$	tangential vector
$\vec{u}$	velocity
x	axial/horizontal coordinate
y	radial/vertical coordinate
z	coordinate perpendicular to twodimensional model plane
β	valve/segment bending parameter
γ	valve/segment buoyancy parameter
Γ	boundary
δ	truncation criterion
Δt	timestep
Δx	characteric element size
ε	penalty function parameter
η	von Mises source position; machine precision
θ	time integration parameter; argument complex von Mises velocity
κ	flow contraction coefficient; asymptotic convergence constant
λ	relative valve opening
μ	von Mises valve angle
ν	kinematic viscosity
ρ	order of convergence
σ	stress; von Mises coordinate along valve; standard deviation
τ	characteristic time scale
φ	valve/segment angle
Ω	domain
∇	gradient vector operator
∇^2	Laplace operator

Indices

b	bending
c	characteristic
f	fluid
g	buoyancy
h	hinge

with $\vec{u}$ the velocity vector, ρ the density, $\boldsymbol{S}$ the Cauchy stress tensor, $\boldsymbol{F}$ the deformation tensor, ∇ the gradient vector operator and the superscript dot $\cdot$ the local (spatial) time derivative. Subscripts f and s refer to the fluid and structure system, respectively. The subscript o refers to the reference state. Assuming that the fluid is Newtonian and that the structure is elastic the following constitutive relations must be satisfied:

$$\boldsymbol{S}_f = -p_f\boldsymbol{I} + \eta((\nabla\vec{u}_f)^c + (\nabla\vec{u}_f)) \qquad \text{in } \Omega_f \qquad \text{(A.2a)}$$

$$\boldsymbol{S}_s = \boldsymbol{G}(\boldsymbol{F}_s) \qquad \text{in } \Omega_s \qquad \text{(A.2b)}$$

with p the pressure, $\boldsymbol{I}$ the unit tensor and $\boldsymbol{G}$ some tensor specifying the constitutive behavior of the structure. Superscript c denotes the conjugate and η the dynamic viscosity. The contact conditions on Γ are:

$$\vec{u}_s = \vec{u}_f \qquad \text{(A.3a)}$$

$$\vec{\sigma}_s = -\vec{\sigma}_f \qquad \text{(A.3b)}$$

with $\vec{\sigma}$ the local stress defined as $\vec{\sigma} = \boldsymbol{S}\cdot\vec{n}$, with $\vec{n}$ the unit outward normal vector on Γ.

To solve the set of equations (A.1), (A.2) and (A.3) simultaneously, several techniques can be applied. Here a reference system is employed whose points move in Ω_f=Ω_r independent of the motion of the fluid. Variables referring to these reference points are denoted by a subscript r. The position of the reference points and structure points are referred to as $\vec{x}_r$ and $\vec{x}_s$, respectively. Using this concept the momentum equation (A.1a) is rewritten as

$$\rho_f\vec{u}_f' + \rho_f(\vec{u}_f - \vec{u}_r)\cdot\nabla\vec{u}_f = \nabla\cdot\boldsymbol{S}_f \qquad \text{in } \Omega_r \qquad \text{(A.4)}$$

Here the accent ' denotes the time derivative of a quantity in point of the moving reference system. The points of the reference system may be moved with an arbitrary velocity as long as the contact condition

$$\vec{u}_r = \vec{u}_s = \vec{u}_f = \vec{x}_r' \qquad \text{on } \Gamma \qquad \text{(A.5)}$$

is satisfied. The reference system can be regarded as a solid with $\vec{u}_f$ and p_f as relevant state variables.

To obtain an approximation of the fluid velocity and the pressure fields within

Ω_r and of the structure displacements in Ω_s, the method of the weighted residuals is applied. This yields for the momentum equations (A.4) and (A.1c):

$$\int_{\Omega_r} \vec{w}_r \cdot [\rho_f \dot{\vec{u}}_f' + \rho_f(\vec{u}_f - \dot{\vec{u}}_r)\cdot\nabla \vec{u}_f]\, d\Omega_r = -\int_{\Omega_r} (\nabla \vec{w}_r)^c : S_f\, d\Omega_r + \int_{\Gamma} \vec{w}_r \cdot \vec{\sigma}_f\, d\Gamma \qquad \text{(A.6a)}$$

$$-\int_{\Omega_s} (\nabla \vec{w}_s)^c : S_s\, d\Omega_s + \int_{\Gamma} \vec{w}_s \cdot \vec{\sigma}_s\, d\Gamma = 0 \qquad \text{(A.6b)}$$

with $\vec{w}$ weighting functions. The continuity equations (A.1b) and (A.1d) yield similar expressions and are not considered here. The position of the reference and structure points are time dependent and not a priori known. As a consequence the gradients ∇ can not be elaborated, Furthermore, the domains Ω_f=Ω_r and Ω_s and the boundary Γ are not a priori known, so the integrals in (A.6) can not be evaluated. Following a method, well-known in nonlinear solid mechanics, it is assumed that an estimated solution of the set of equations has been determined. Estimations of the unknown variables (denoted with a superscript asterisk *) are $\dot{\vec{u}}_r^*$ and $\vec{x}_r^*$ on Γ, $\vec{x}_s^*$, $\vec{u}_f^*$ and p_f^*, which can be used to compute ∇^*, S_s^*, F_s^* and S_f^*. Together with the known reference state and the unknown current state, the estimated state is shown in figure A.2.

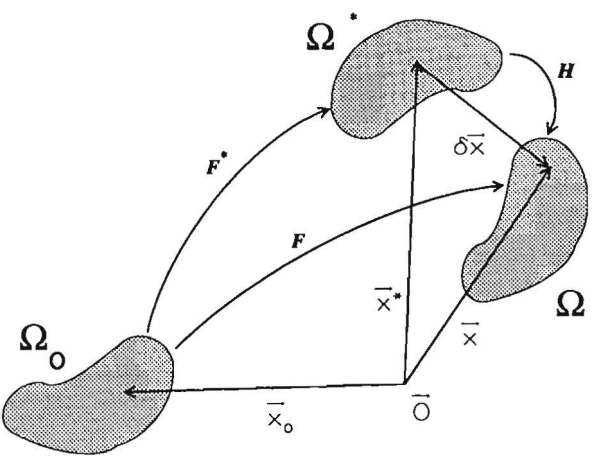

figure A.2 Definition of position vectors and transformation tensors

The value of the relevant reference state in the current state can be written as the sum of their estimated values and iterative changes, according to

$$\vec{x}_r = \vec{x}_r^* + \delta\vec{x}_r \tag{A.7a}$$
$$\vec{x}_s = \vec{x}_s^* + \delta\vec{x}_s \tag{A.7b}$$
$$\vec{u}_f = \vec{u}_f^* + \delta\vec{u}_f \tag{A.7c}$$
$$p_f = p_f^* + \delta p_f \tag{A.7c}$$
$$S_s = S_s^* + \delta S_s \tag{A.7e}$$

Using a tensor $\boldsymbol{H}$, which describes the deformation form the estimated state to the current state the following expressions can be derived

$$\nabla = \boldsymbol{H}^{-c}\nabla^* \tag{A.8a}$$
$$d\Omega_r = \det(\boldsymbol{H})\, d\Omega_r^* \tag{A.8b}$$
$$d\Omega_s = \det(\boldsymbol{H})\, d\Omega_s^* \tag{A.8c}$$
$$d\Gamma = \det(\boldsymbol{H})\, \|\boldsymbol{H}^{-c}\cdot\vec{n}^*\|\, d\Gamma^* \tag{A.8d}$$

Substitution of (A.7) and (A.8) in (A.6) yields:

$$\int_{\Omega_r^*} \vec{w}_r\cdot[\rho_f\dot{\vec{u}}_f' + \rho_f(\vec{u}_f\cdot\vec{u}_r)\cdot\{\boldsymbol{H}^{-c}\nabla^*\vec{u}_f\}]\det(\boldsymbol{H})d\Omega_r^* =$$

$$\int_{\Omega_r^*} \{(\nabla^*\vec{w}_r)^c\cdot\boldsymbol{H}^{-1}\}:\{-p\boldsymbol{I} + \eta(\nabla^*\vec{u}_f)^c\cdot\boldsymbol{H}^{-1} + \eta\boldsymbol{H}^{-c}\cdot(\nabla^*\vec{u}_f)\}\det(\boldsymbol{H})d\Omega_r^* +$$

$$\int_{\Gamma^*} \vec{w}_r\cdot\vec{\sigma}_f \det(\boldsymbol{H})\|\boldsymbol{H}^{-c}\cdot\vec{n}^*\|\, d\Gamma^* \tag{A.9a}$$

$$\int_{\Omega_s^*} \{(\nabla^*\vec{w}_s)^c\cdot\boldsymbol{H}^{-1}\}:(S_s^* + \delta S_s)\det(\boldsymbol{H})\, d\Omega_s^* +$$

$$\int_{\Gamma^*} \vec{w}_s\cdot(\vec{\sigma}_s^* + \delta\vec{\sigma}_s)\det(\boldsymbol{H})\|\boldsymbol{H}^{-c}\cdot\vec{n}^*\|\, d\Gamma^* = 0 \tag{A.9b}$$

Here, $\boldsymbol{H}$, δS_s and δS_f are nonlinear functions of $\delta\vec{x}_s$, $\delta\vec{x}_r$, $\delta\vec{u}_f$ and δp_f. In order to solve the system (A.9) it is linearized and discretized. This will eventually lead to a set of linear equations of the form

$$\underline{\underline{M}}\,\underline{a} = \underline{f} \tag{A.10a}$$

$$\underline{a} = [\delta\underline{u}_f\ \delta\underline{p}_f\ \delta\underline{x}_r\ \delta\underline{x}_s]^T \tag{A.10b}$$

So the final set (A.10) contains the unknowns of both fluid and structure, which are solved simultaneously.

In the process of linearization of (4.9) numerous simplifications and additional assumptions can be made. For instance, a relationship between $\vec{u}_r$ and $\vec{x}_s$ can be chosen in order to eliminate $\vec{u}_r$ as unknown. This could lead to an Arbitrary Langrange-Euler approach, in which the nodal points of both fluid and structure move with a prescribed velocity. The process of linearization, simplification and implementation is a tedious one and, which is more important, does not guarantee to the stability of the solution of the resulting set of equations, especially when the structure displacements are large.

APPENDIX B: VON MISES FLUID MODEL

In this appendix some details are given of the analytical potential fluid model for the steady flow around a rigid valve as developed by von Mises (Gurevich, 1965).

A sketch of the fluid domain is given in figure 2.2. The domain is regarded as a complex plane, the z-plane. In this plane a velocity vector is defined as

$$\vec{u} = u\, e^{i\theta} \tag{B.1}$$

with u the amplitude and θ the argument of the velocity. Defined are also the complex conjugate of the normalized velocity

$$\xi = \frac{u}{u_t} e^{-i\theta} \tag{B.2}$$

with u_t the magnitude of the velocity at the valve tip and on the free streamline. Define also a complex velocity potential W and its complex conjugate W^c, satisfying

$$\frac{dW^c}{dz} = \vec{u} \tag{B.3}$$

so

$$\xi = \frac{1}{u_t} \frac{dW}{dz} \tag{B.4}$$

The velocity field in the physical z-plane is transformed by the transformation

$$\xi = t^{\mu} \tag{B.5}$$

to a half sphere in another complex plane, which we will call the t-plane (see figure B.1). The orientation of the valve is defined as $\mu\pi$. This can be shown as follows. From the z-plane it is clear that in E $u=u_t$ and $\theta=0$. From (B.2) and (B.5) it follows that t=1. On the rigid walls EH and HC is also valid that $\theta=0$; the local velocity there is smaller than u_t and equals zero in the stagnation point C. So, EH and HC are transformed to the interval $t\epsilon[0;1]$ of the positive real axis in the t-plane. The point C is a special one, since the derivative $\frac{d\xi}{dt}$ is not bounded there, so the transformation is locally not conform. This problem is avoided by considering a half circle around C in the t-plane with arbitrary small radius ε. Then $t=\varepsilon\, e^{i\alpha}$ and according to (B.5)

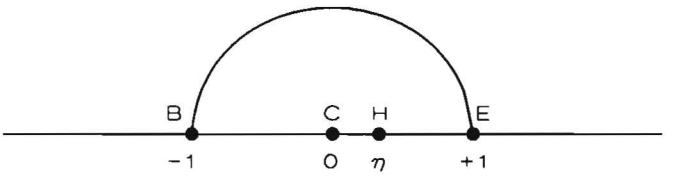

figure B.1 Von Mises fluid domain, transformed to a half circle in the complex t-plane

$\xi=\varepsilon\mu e^{i\mu\alpha}$. It follows that an increment α in the t-plane corresponds to an increment $\mu\pi$ in the z-plane and that happens to be the orientation of CB. Point B transforms to t=-1 (in B $u=u_t$ and $\theta=\mu\pi$, so $t=\xi^{1/\mu}=e^{i\pi}=-1$). So, the line CB is transformed to the interval $t\in[-1;0]$ on the negative real axis in the t-plane. On the free streamline BE $u=u_t$ so $|\xi|=|t|=1$. The argument in the z-plane ranges from $\mu\pi$ in B to 0 in E and from (B.5) it follows that the argument in the t-plane then ranges from π in B and 0 in E. This is a half circle with radius 1 in the upper half space from B to E, which closes the contour.

The flow in both the z-plane and the t-plane can be represented by a source of strength q in H and a sink of strength -q in E. It is convenient to extend the domain in the t-plane to the whole plane. In order to satisfy the boundary conditions at the real axis (no flow penetrating it) a mirror transformation with respect to the real axis is performed, which creates a closed spherical streamline. Because of this extension the source and sink are doubled in strength, because only half of the fluid arrives in the upper half plane. The circle theorem of Milne-Thomson is used to satisfy the boundary condition on the circle. Consider a complex plane in which the flow can be represented by a complex velocity potential W=f(t). Then the potential flow in the same plane with a cylinder (radius r) placed in the origin, is described by

$$W = f(t) + f\left(\frac{r^2}{t}\right) \qquad \text{(B.6)}$$

(Milne-Thomson,1966). The resulting velocity potential in the complex plane of interest becomes (figure B.2):

$$W = \frac{q}{\pi}\ln(\eta) + \frac{q}{\pi}\ln(t-\eta) +$$

$$+ \frac{q}{\pi}\ln\left(t-\frac{1}{\eta}\right) - \frac{2q}{\pi}\ln(t-1) \qquad \text{(B.7)}$$

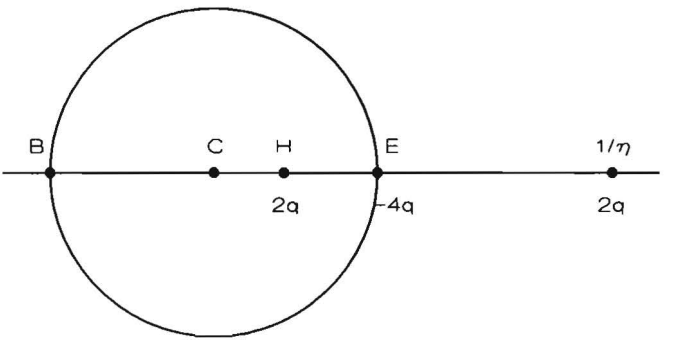

figure B.2 Von Mises fluid domain, extended to the full complex t-plane, using extra sources and sinks

Parameter η, the position of the source, is still not known but can be determined by making use of the fact that $|CB|=1$. Using the identity

$$z = \frac{1}{u_t} \int u_t \frac{dz}{dW} dW = \frac{1}{u_t} \int \frac{1}{\zeta} dW \qquad (B.8)$$

and (B.5) gives

$$z = \frac{1}{u_t} \int t^{-\mu} \frac{dW}{dt} dt. \qquad (B.9)$$

CB is in the t-plane represented by

$$t^{\mu} = e^{-i\mu\pi\sigma\mu} \qquad \sigma\epsilon[0;1]. \qquad (B.10)$$

Substituting this in (B.9) and using the derivative of (B.7) with respect to t gives

$$I = |CB| =$$

$$\frac{q}{\pi \cdot u_t} \int_0^{-1} \frac{dt}{t^{\mu}} \left\{ \frac{1}{t-\eta} + \frac{1}{t-1/\eta} - \frac{2}{t-1} \right\} \qquad (B.11)$$

$$\int_{\Omega} v[\nabla \cdot \vec{u}]d\Omega = 0 \qquad \text{(C.4b)}$$

for $\forall \vec{w} \in W$ $\forall v \in V$. All components of the vector function $\vec{w}$ and their partial derivatives in space as well as the scalar function v must be square Lebesque integrable over the domain Ω. Using integration by parts and Gauss' theorem, the first equation is transformed to:

$$\int_{\Omega} [St\, \vec{w} \cdot \dot{\vec{u}} + \vec{w} \cdot [\vec{u} \cdot (\nabla \vec{u})] + (\nabla \vec{w})^{c} : S]d\Omega = \int_{\Omega} \vec{w} \cdot \vec{f} d\Omega + \int_{\Gamma} \vec{w} \cdot \vec{t} d\Gamma \qquad \text{(C.5)}$$

for $\forall \vec{w} \in W$, with $\vec{t}$ the stress vector defined as $\vec{t} = S \cdot \vec{n}$, $\vec{n}$ being the outward normal unit vector on boundary Γ. Equations C.5 and C.4b are suitable for discretization with the finite element method. In this method the region Ω is divided into elements. Every element consists of a number of nodal points for the velocity and the pressure and the unknowns $\vec{u}$ and p are supposed to be a linear combination of the values of these unknowns in the nodal points:

$$\vec{u}(\vec{x},t) = \sum_{i=1}^{n} \varphi_i(\vec{x})\, \vec{u}_i(t) \qquad \text{(C.6a)}$$

$$p(\vec{x},t) = \sum_{i=1}^{m} \psi_i(\vec{x})\, p_i(t) \qquad \text{(C.6b)}$$

with n the total number of nodal points for the velocity and m the total number of nodal points for the pressure. The functions φ_i and ψ_i are the so-called basis functions for the velocity and the pressure in nodal point i, respectively. These functions are fully determined by the position vector $\vec{x}$. The symbols $\vec{u}_i$ and p_i present the velocity vector and the pressure in nodal point i, respectively, and are only functions of time. Therefore, the velocity and pressure fields are completely determined by the basis functions and the nodal point values. To solve the system of equations also assumptions must be made for the weight functions $\vec{w}$ and v. To this end finite dimensional subspaces $W_h \subset W$ and $V_h \subset V$ are constructed and the equations C.4b and C.5 should hold for $\vec{w}_h \in W_h$ and $v_h \in V_h$. Within the Galerkin method the basis functions for the velocity and the pressure are used to define these subspaces. In other words W_h is spanned by the set $\{\varphi_i, i=1,n\}$ and V_h is spanned by the set $\{\psi_i, i=1,m\}$. Therefore, the arbitrary weight functions $\vec{w}_h$ and v_h can be written

as:

$$\vec{w}_h(\vec{x},t) = \sum_{i=1}^{n} \varphi_i(\vec{x})\vec{w}_i(t) \tag{C.7a}$$

$$v_h(\vec{x},t) = \sum_{i=1}^{m} \psi_i(\vec{x})v_i(t) \tag{C.7b}$$

Substitution of the equations C.6 and C.7 into the equations C.5 and C.4b leads to:

$$\sum_{i=1}^{n} \vec{w}_i \cdot \{ \int_{\Omega} [St\, \varphi_i \sum_{j=1}^{n} \varphi_j \dot{\vec{u}}_j + \varphi_i \sum_{j=1}^{n} \varphi_j \sum_{l=1}^{n} (\nabla \varphi_l \vec{u}_l)^c \cdot \vec{u}_j + S^c \cdot \nabla \varphi_i] d\Omega \} =$$

$$\sum_{i=1}^{n} \vec{w}_i \cdot \{ \int_{\Omega} \varphi_i \vec{f}\, d\Omega + \int_{\Gamma} \varphi_i \vec{t}\, d\Gamma \} \tag{C.8a}$$

$$\sum_{i=1}^{m} v_i \int_{\Omega} \psi_i \sum_{j=1}^{n} \nabla \varphi_j \cdot \vec{u}_j d\Omega = 0 \tag{C.8b}$$

for all $\forall \vec{w}_h \in W_h$ and $\forall v_h \in V_h$. The requirement that these equations must hold for all admissable vector functions $\vec{w}_h$ and scalar functions v_h, substitution of the constitutive relation for Newtonian fluids (eq. C.2) and presentation in a Cartesian coordinate system leads to a set of differential equations. With the gradient operator, the velocity and the pressure column defined as:

$$\underset{\sim}{\nabla}^T = [\partial/\partial x_1, \partial/\partial x_2]$$
$$\underset{\sim}{u}^T = [\underset{\sim}{u}_1^T, \ldots, \underset{\sim}{u}_n^T]$$
$$\underset{\sim}{p}^T = [p_1, \ldots, p_m]$$

and $\underline{I}$ being a 2-dimensional unit matrix, the set of nonlinear first order equations reads:

$$\underline{M}\, \dot{\underset{\sim}{u}} + [\underline{S} + \underline{N}(\underset{\sim}{u})]\underset{\sim}{u} + \underline{L}^T \underset{\sim}{p} = \underset{\sim}{f} + \underset{\sim}{b} \tag{C.9a}$$

$$\underline{L}\, \underset{\sim}{u} = \underset{\sim}{0} \tag{C.9b}$$

with $\underline{M}$ the mass matrix:

$$\underline{M}^{ij} = St \int_{\Omega} \varphi_i \varphi_j\, \underline{I}\, d\Omega \tag{C.10a}$$

$\underline{\underline{S}}$ the diffusion matrix:

$$\underline{\underline{S}}^{ij} = \frac{1}{Re}\int_{\Omega} [(\underline{\nabla}\varphi_i^T \underline{\nabla}\varphi_j)\underline{\underline{I}} + \underline{\nabla}\varphi_i \underline{\nabla}\varphi_j^T]d\Omega \qquad \text{(C.10b)}$$

$\underline{\underline{N}}(\underline{u})$ the convection matrix:

$$\underline{\underline{N}}(\underline{u})^{ij} = \int_{\Omega} \varphi_i\varphi_j \sum_{l=1}^{n} (\underline{\nabla}\varphi_l \underline{u}_l^T)d\Omega \qquad \text{(C.10c)}$$

$\underline{\underline{L}}$ the divergence matrix:

$$(\underline{\underline{L}}^T)^{ij} = -\int_{\Omega} \psi_j \underline{\nabla}\varphi_i d\Omega \qquad \text{(C.10d)}$$

$\underline{f}$ the body force column:

$$\underline{f}^i = \int_{\Omega} \varphi_i \underline{f} d\Omega \qquad \text{(C.10e)}$$

and $\underline{b}$ the boundary stress column:

$$\underline{b}^i = \int_{\Gamma} \varphi_i \underline{t} d\Gamma \qquad \text{(C.10f)}$$

In this presentation $\underline{\underline{M}}$, $\underline{\underline{S}}$ and $\underline{\underline{N}}$ are square 2nx2n matrices, $\underline{\underline{L}}$ is a mx2n matrix and $\underline{f}$ and $\underline{b}$ are 2nx1 columns. $\underline{\underline{M}}^{ij}$, $\underline{\underline{S}}^{ij}$ and $\underline{\underline{N}}(\underline{u})^{ij}$ are square 2×2 matrices and $(\underline{\underline{L}}^T)^{ij}$, $\underline{f}^j$ and $\underline{b}^j$ are 2×1 matrices.

The application of the penalty function method (see section 2.1.3) leads in a similar way to the pressure matrix $\underline{\underline{M}}_p$:

$$\underline{\underline{M}}_p^{ij} = \int_{\Omega} \psi_i\psi_j d\Omega \qquad \text{(C.11)}$$

Since the matrix $\underline{\underline{L}}$ is not a square matrix, it has at most m independent rows. The same is true for the 2nx2n matrix $\frac{1}{\varepsilon}\underline{\underline{L}}^T\underline{\underline{M}}_p^{-1}\underline{\underline{L}}$ which occurs due to the application of the panlaty function method. Therefore this matrix is singular.

APPENDIX D: VAN WIJNGAARDEN-DEKKER-BRENT METHOD

In this appendix an outline is given of the van Wijngaarden-Dekker-Brent method (Brent, 1973). In the remainder it will be referred to as *Brent's method*. It is used in section 2.3 for the convergence to the equilibrium position of a rigid valve.

Essentially, the method is a combination of bisection and interpolation. It combines a guaranteed global convergence of at least first order with a superlinear convergence close to roots of continuously differentiable functions. Roughly sketched, the method proceeds as follows.

It is assumed that the root is initially bracketed in a known interval. The method decreases the interval length stepwise, assuring that the root is kept within the brackets. If possible, a next estimate of the root is obtained by an interpolation within the current interval, but at the start of each step it is first checked whether the decrease of the interval bounds has been sufficiently rapid in the previous iteration steps. If not, the interpolation is obviously not efficient enough and a bisection step is taken. If it was, a new interpolation is tested (but not yet performed!). Depending on the available old points the interpolation is either linear or inverse quadratic (position φ as quadratic function of moment m). Then it is checked whether there is no danger of over- or underflow and whether the interpolated point falls within the bracketed interval. If so, the interpolation is performed, otherwise a bisection step is taken. In all cases the correction is at least equal to the demanded tolerance, since a smaller step does not make sense.

If three distinct old points a,b and c are available an inverse quadratic Lagrange interpolation is used. The interpolation is *inverse* quadratic since with a direct quadratic interpolation a quadratic equation must be solved, which in general gives two distinct roots. Inverse quadratic interpolation avoids the problem of which root should be accepted. The interpolation formula is (Press et al., 1986)

$$\varphi = \frac{[m-m(a)][m-m(b)]\,c}{[m(c)-m(a)][m(c)-m(b)]} + \frac{[m-m(b)][m-m(c)]\,a}{[m(a)-m(b)][m(a)-m(c)]} + \frac{[m-m(c)][m-m(a)]\,b}{[m(b)-m(c)][m(b)-m(a)]} \qquad (D.1)$$

Setting m to zero gives as next root estimate

$$\varphi = b + \frac{p}{q} \qquad (D.2a)$$

with

$$r = m(b)/m(c),\ s = m(b)/m(a),\ t = m(a)/m(c) \qquad \text{(D.2b)}$$

$$p = s[t(r-t)(c-b) - (1-r)(b-a)] \qquad \text{(D.2c)}$$

$$q = (t-1)(r-1)(s-1) \qquad \text{(D.2d)}$$

If there are only two distinct old points available the inverse quadratic interpolation is not possible, so a linear interpolation is performed using (D.2.5) and (D.2a) together with

$$p = (c-b)s \qquad \text{(D.4a)}$$

$$q = s-1 \qquad \text{(D.4b)}$$

Now the algorithm is discussed in somewhat more detail way. Consider again the three points a,b, and c and define them such that m(b) m(c)≤0 and $|m(b)| \leq |m(c)|$. Here b is the best approximation to φ_{equil} so far, a is the previous value of b (and may be equal to c) and φ_{equil} must lie between b and c (initially a=c). Define also the tolerance δ and the midpoint of the interval $z=\frac{1}{2}(c-b)$. Furthermore, denote d as the correction to be made on b and e as the previous correction made. Apart from initializations a typical step is taken as follows:

```
{test whether convergence is achieved}
if |z|≤δ or m(b)=0 then {root is found}
        stop;
{root not found, so proceed}
if |e|<δ or |m(b)|>|m(a)| then
        {convergence is too slow: use bisection}
        d:=z; e:=d;
else {convergence is rapid enough: use interpolation if possible}
        if a=c then
                {only two distinct points: use linear interpolation}
                p := (c-b)s
                q := s-1
        else {three distinct points a,b,c available: use quadratic interpolation}
                p := s[t(r-t)(c-b) - (1-r)(b-a)]
                q := (t-1)(r-1)(s-1)
        {test if interpolation is successful}
```

```
        if |p/q|<1.5|z| {interpolation within boundary?}
                and |p/q|<½|e| {convergence fast enough?} then
                {accept interpolation}
                d:=p/q; e:=d;
        else {interpolation not possible or not efficient enough}
                d:=z; e:=d;
    if |d|<δ then {correction too small to be meaningful: take step of δ}
        b:=b+δ
    else {correction large enough: accept it}
        b:=b+d
    {proceed with next step}
```

The choice for the criterion $|p/q|<1.5|z|$ instead of the simpler criterion $|p/q|<|z|$ is motivated by Brent because of the use of the quadratic interpolation. For more details one is refered to his work.

The tolerance of the final approximation of the root is 2δ, where

$$\delta = 2\varepsilon|b| + \delta_a \qquad \text{(D.5)}$$

with ε the relative machine precision and δ_a a positive absolute tolerance. The algorithm is designed in such a way that rounding errors cannot prevent convergence (Brent, 1973, p51). If rounding errors are taken into account the tolerance δ increases slightly to

$$\delta = 3\varepsilon|b| + \delta_a \qquad \text{(D.6)}$$

(Brent, 1973, p52).

By carefully checking the convergence rate and taking bisection steps if necessary, Brent's method is never much slower than the bisection method. This is the main improvement of Brent. It is especially important for ill-behaved functions and for initial guesses far from roots of well-behaved functions. At a certain stage of the iteration process, closer to the root, superlinear convergence will set in. The order of convergence then will be at least equal to that of the secant method (successive linear interpolation), i.e. $\rho = \frac{1}{2}(1+\sqrt{5}) \approx 1.62$. The inverse quadratic interpolation (also added by Brent) can improve this slightly, but the effect is only modest. Practical tests of Brent show reduction of the total number of function evaluations by several percents.

In section 2.3 the bracketing of the root (which must proceed the application of Brent's method) is described globally. Here, some more details are given.

With φ_j the j-th estimate of the valve position on timestep n+1 and m_j the resulting moment, $\Delta\varphi_{try}$ a trial step, $\Delta\varphi_{max}$ the maximum allowed step, φ_{min} and φ_{max} the minimum and maximum allowed position and μ an elongation factor, the algorithm can be written as follows:

$\varphi_1 := \varphi^n$ {solution of previous timestep as initial estimate}
if $m_1 > 0$ then {valve is pushed down}
    $\varphi_2 := \varphi_1 + \Delta\varphi_{try}$
else {valve is pushed up}
    $\varphi_2 := \varphi_1 - \Delta\varphi_{try}$
j:=2
repeat
    $\Delta\varphi := \mu\, m_j(\varphi_{j-1}-\varphi_j)/(m_{j-1}-m_j)$
    if $|\Delta\varphi| \le \Delta\varphi_{max}$ then
        $\varphi_{j+1} := \varphi_j + \Delta\varphi$
    else {step too large, must be restricted}
        $\varphi_{j+1} := \varphi_j + \Delta\varphi_{max}\,\mathrm{sign}(\Delta\varphi)$
    if $\varphi_{j+1} < \varphi_{min}$ then $\varphi_{j+1} := \varphi_{min}$
    if $\varphi_{j+1} > \varphi_{max}$ then $\varphi_{j+1} := \varphi_{max}$
until $m_j\, m_{j+1} < 0$

Every timestep the two most recent estimates are used because they are the closest to the root, since $m(\varphi)$ is monotonic and only extrapolation takes place.

APPENDIX E: POWELL'S HYBRID METHOD

In this appendix an outline is given of Powell's hybrid method, which is used in section 2.3.2 to locate the equilibrium position of a segmented valve. Consider the scalar function

$$r(\varphi) = \sum_{i=1}^{n} m_i^2(\varphi) \tag{E.1}$$

$$= \underset{\sim}{m}^T(\varphi)\underset{\sim}{m}(\varphi) \tag{E.2}$$

with $\varphi^T = [\varphi_1,....,\varphi_n]$ and $\underset{\sim}{m}^T = [f_1,....,f_n]$. r is total residual to be minimized and m_i are functions of a parameter set φ. In this study, $\underset{\sim}{m}$ represents the link moments and φ the positions of the links.

Since the problem is nonlinear an iteration is used according to

$$\varphi_{k+1} = \varphi_k + \delta_k \tag{E.3}$$

with φ_k the k-th estimate for the minimum and δ_k a correction to it. Differentiating (E.2) with respect to φ and setting the gradient to zero (since a minimum is sought) leads to

$$[\underset{\sim}{J}_k^T\underset{\sim}{J}_k + \sum_{i=1}^{n} m_i(\varphi)\nabla^2 m_i(\varphi)]\underset{\sim}{\delta}_k = -\underset{\sim}{J}_k^T\underset{\sim}{m}_k \tag{E.4}$$

with $\underset{\sim}{J}(\varphi)$ the Jacobian matrix of $\underset{\sim}{m}$, defined by

$$J_{ij} = \frac{\partial m_i}{\partial \varphi_j} \tag{E.5}$$

with i=1,...n and j=1,...n. At this point it is assumed that the residual $r(\varphi)$ is zero at the minimum and that it is small close to it. Since in this study $\underset{\sim}{m}$ represents the link moments which are zero at the equilibrium position and which are smooth functions of position, it is expected that this assumption holds indeed. Then, the second term on the left hand side can be ignored. With this approximation (E.3) becomes

$$\underset{\sim}{J}_k^T\underset{\sim}{J}_k\underset{\sim}{\delta}_k = -\underset{\sim}{J}_k^T\underset{\sim}{m}_k \tag{E.6}$$

This is further simplified by a premultiplication by $\underline{J}_k^{-T}$, yielding

$$\underline{J}_k \underset{\sim}{\delta}_k = -\underset{\sim}{m}_k \tag{E.7}$$

Since no derivatives are available, the Jacobian matrix $\underline{J}_k$ and its inverse $\underline{J}_k^{-1}$ are approximated by matrices $\underline{B}_k$ and $\underline{H}_k$. At the first iteration step, $\underline{B}_0$ is approximated by finite differences and $\underline{H}_0$ from an inversion of $\underline{B}_0$. At the next iteration steps they are updated according to

$$\underline{B}_{k+1} = \underline{B}_k + \frac{(\Delta \underset{\sim}{m}_k - \underline{B}_k \, \Delta \underset{\sim}{\varphi}_k) \, \Delta \underset{\sim}{\varphi}_k^T}{\Delta \underset{\sim}{\varphi}_k^T \, \Delta \underset{\sim}{\varphi}_k} \tag{E.8}$$

$$\underline{H}_{k+1} = \underline{H}_k - \frac{(\underline{H}_k \Delta \underset{\sim}{m}_k - \Delta \underset{\sim}{\varphi}_k) \, \Delta \underset{\sim}{\varphi}_k^T \, \underline{H}_k}{\Delta \underset{\sim}{\varphi}_k^T \, \underline{H}_k \, \Delta \underset{\sim}{m}_k} \tag{E.9}$$

This is found by assuming $\underset{\sim}{m}$ to be linear and demanding that the update (E.3) does not cange the information normal to the step. It is called *Broyden's rank-one* updating formula.

An iteration step starts with the computation of a so-called *Gauss-Newton* step

$$\underset{\sim}{\delta}_k^{gn} = -\underline{H}_k \, \underset{\sim}{m}_k \tag{E.10}$$

This follows from (E.7) and (E.9). This step can be computed directly, without solving a set of equations. Close to a minimum of locally nearly quadratic functions, an iteration based on Gauss-Newton step will show a fast, superlinear convergence. Far from the minimum however, the convergence can be poor.

Therefore, the step size that may be taken at any iteration is limited by a variable parameter Δ_k which defines a region of trust. If $\|\underset{\sim}{\delta}_k^{gn}\| \leq \Delta_k$ then the Gauss-Newton step is accepted. Otherwise the vector

$$\underset{\sim}{\delta}_k^{sd} = -\underline{B}_k^T \, \underset{\sim}{m}_k \tag{E.11}$$

is calculated. $\underset{\sim}{\delta}_k^{sd}$ is proportional to the negative gradient of $r(\varphi)$ and thus pointing to the direction of steepest descent. A step of length

$$\alpha_k = \frac{\|\underline{B}_k^T \, \underset{\sim}{m}_k\|^2}{\|\underline{B}_k \underline{B}_k^T \, \underset{\sim}{m}_k\|^2} \tag{E.12}$$

in this direction is considered. This step would give the exact minimum along $\underset{\sim}{\delta}_k^{sd}$ if $r(\varphi)$ was quadratic. If $\alpha_k \|\underset{\sim}{\delta}_k^{sd}\| \geq \Delta_k$ then a pure steepest-descent move of magnitude Δ_k is made:

$$\varphi_{k+1} = \varphi_k + \frac{\Delta_k}{\|\underset{\sim}{\delta}_k^{sd}\|} \underset{\sim}{\delta}_k^{sd} \tag{E.13}$$

Failing both of these events, the method interpolates between $\underset{\sim}{\delta}_k^{gn}$ and $\underset{\sim}{\delta}_k^{sd}$ according to

$$\varphi_{k+1} = \varphi_k + \beta_k \underset{\sim}{\delta}_k^{gn} + (1-\beta_k)\alpha_k \underset{\sim}{\delta}_k^{sd} \tag{E.14}$$

where β_k is chosen such that $\|\Delta\varphi_k\| = \Delta_k$.

Δ_k controls the mixture of Gauss-Newton and steepest-descent methods, a large value favors the former and a small value the latter. The value of Δ_k is adapted during the iteration, depending on the progress of the minimization process. To decide whether or not to change Δ_k in the next iteration, the actual reduction in function value is compared with that predicted assuming $r(\varphi)$ to be quadratic. If the progress is poor, Δ_k is decreased (increasing the steepest-descent bias). If $r(\varphi)$ appears to be locally nearly quadratic and so the progress is good , Δ_k might be increased (favoring the Gauss-Newton step). Within one iteration step, an inner iteration is performed in which the Δ_k, the step size and the step direction are repeatedly adapted until $r_{k+1} < r_k$.

As an infinitesimal step in the steepest-descent direction will always reduce the function value at non-stationary points, a sufficient small initial value of Δ_k will always be successful and the method can consequently be made globally convergent. Since these infinitesimal steps converge very slow, good initial estimates φ_0 and $\underline{B}_0$ are still important for a fast convergence at some distance of the minimum. Close to the minimum of locally nearly quadratic functions $r(\varphi)$ the method reverts to the original Gauss-Newton method, resulting in a fast, superlinear convergence.

APPENDIX F: QUASI 1D FLUID MODEL WITH A PARABOLIC VELOCITY PROFILE

In this appendix an estimation is given of the effect of a parabolic velocity profile on the steady quasi one-dimensional fluid model of chapter 2. Again it is assumed that there is no pressure gradient in vertical direction. Some symbols are defined in figure F.1.

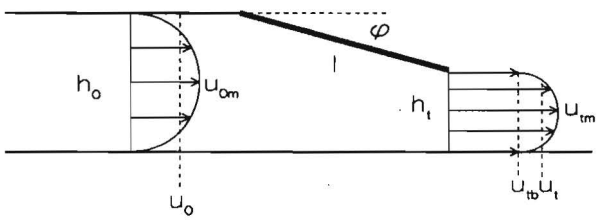

figure F.1 Definitions for a quasi one-dimensional fluid model with a parabolic velocity profile

If the dimensionless two-dimensional Navier-Stokes and continuity equations are considered in the vorticity formulation (Batchelor, 1983) and if the inertial term and the viscosity term are omitted, the fluid flow satisfies

$$\vec{u} \cdot \nabla \omega = 0 \qquad \text{(F.1)}$$

$$u_o h_o = u_t h_t \qquad \text{(F.2)}$$

with $h_o \equiv 1$ and ω the vorticity

$$\omega = \frac{\partial u_y}{\partial x} - \frac{\partial u_x}{\partial y} \qquad \text{(F.3)}$$

Since in this case $\partial u_y/\partial x$ is small, it follows from (F.3) and (F.1) that $\partial u_x/\partial y$ is approximately constant along a streamline. In the remainder of this appendix the suffix x will be omitted. With the additional assumption that streamlines which are equidistant in the entrance plane, stay equidistant throughout the fluid domain, it follows that the shape of the velocity profile remains unchanged. From this assumptions it follows that (see figure F.1)

$$\frac{u_{tm} - u_{tb}}{h_t} = \frac{u_{om}}{h_o} \qquad \text{(F.4)}$$

In order to satisfy the continuity equation (F.2) the velocity profile at the valve tip is a biased parabolic one as shown in figure F.1. Furthermore,

$$u_o = \frac{2}{3} u_{om} \tag{F.5}$$

$$u_t = u_{tb} + \frac{2}{3} (u_{tm} - u_{tb}) \tag{F.6}$$

$$\lambda = h_t/h_o = 1 - l \sin \varphi \tag{F.7}$$

From (F.2), (F.4), (F.5), (F.6) and (F.7) it follows that

$$u_{tm} = u_o[\frac{1}{\lambda} + \frac{1}{2}\lambda] \tag{F.8}$$

From Bernoulli's theorem it follows that the maximum pressure difference over the valve is given by

$$\Delta p = \frac{1}{2} u_{tm}^2 - \frac{1}{2} u_{om}^2 \tag{F.9}$$

For a flat velocity profile $u_{tm}=u_t$ and $u_{om}=u_o$ so that

$$\Delta p_{flat} = \frac{1}{2} u_o^2 [\frac{1}{\lambda^2} - 1] \tag{F.10}$$

Substituting (F.5) and (F.8) in (F.9) yields for a parabolic velocity profile

$$\Delta p_{par} = \frac{1}{2} u_o^2 \{ [\frac{1}{\lambda^2} - 1] + \frac{1}{4}[\lambda^2 - 1] \} \tag{F.11}$$

For a modest valve closure of $\varphi = 10^o$ ($\lambda = 0.76$) and $u_o \equiv 1$, $\Delta p_{flat} = 0.366$ while $\Delta p_{par} = 0.313$. This is a relative decrease of about 14%.

STELLINGEN

behorende bij het proefschrift

On the analysis of moving heart valves
A numerical fluid-structure interaction model

J.B.A.M. Horsten

1) Zwak-gekoppelde vloeistof-structuur interactiemodellen zijn ongeschikt voor de analyse van de beweging van lichte, flexibele structuren zoals hartkleppen.
   T. Belytschko, 1980
   Hoofdstuk 1 van dit proefschrift

2) De beperkte numerieke stabiliteit van het vloeistof-structuur interactiemodel van Peskin wordt in belangrijke mate veroorzaakt door een fysisch niet-realistische benadering van de vloeistofkrachten.
   C.S. Peskin, 1977
   Hoofdstuk 1 van dit proefschrift

3) De analytische modellen van van Steenhoven & van Dongen en van Wippermann voor de beweging van de aortaklep kunnen op eenvoudige wijze worden uitgebreid met de invloed van viskeuze stromingseffecten.
   A.A. van Steenhoven & M.E.H. van Dongen, 1979
   F.K. Wippermann, 1985
   Hoofdstuk 4 van dit proefschrift

4) Gezien de potentieel fnuikende invloed van snurken op intermenselijke relaties, is de analyse ervan een maatschappelijk zeer relevante toepassing van stroming-structuur interactiemodellen.

5) Volgens tenminste een gedeelte van de door haarzelf opgestelde kenmerken kan de wetenschapsfilosofie zelf niet als wetenschap worden aangemerkt.
   A. Chalmers, Wat heet wetenschap, Boom, 1987

6) De natuurwetenschap houdt zich niet bezig met het verklaren van verschijnselen, maar slechts met de beschrijving van de onderlinge samenhang ervan.

L. Wittgenstein, Tractatus logico-philosophicus, Polak & van Gennep, 1975

7) Vanwege het voortdurend gebrek aan ethische en maatschappelijke vorming van studenten aan de technische universiteiten, zijn deze universiteiten in belangrijke mate medeverantwoordelijk voor het onethisch en maatschappelijk ongewenst gebruik van techniek.

8) Denken over de dood maakt het leven zinvol.

M. Heidegger, Sein und Zeit, Niemeyer, 1941

9) Indien hun spel niet hoorbaar verschilt van elektronisch voortgebrachte muziek, zijn musici muzikaal gezien overbodig en moet hun beroep beschouwd worden als een folkloristisch ambacht.